

# Virtual Elements for sound propagation in complex poroelastic media

Abhilash Sreekumar<sup>1</sup> · Savvas P. Triantafyllou<sup>2</sup> · Fabien Chevillotte<sup>3</sup>

Received: date / Accepted: date

**Abstract** We develop a novel Virtual Element Method (VEM) to resolve the mixed Biot displacement pressure formulation governing wave propagation in porous media. Within this setting, the weak form of the governing equations is discretized using implicitly defined canonical basis functions and the resulting integral forms are computed using appropriate polynomial projections. The projection operator accounting for the solid, fluid, and coupling phases of the problem are presented. Different boundary, interface and excitation conditions are accounted for. The convergence behaviour, accuracy, and efficiency of the method is examined through a set of illustrative examples. A node insertion strategy is proposed to resolve non-conforming interfaces that naturally arise in multilayered systems. Finally the power of the VEM is exploited to examine the acoustic response of composite materials with periodic and non-periodic inclusions of complex geometries.

**Keywords** Virtual Element Method · Porous media · Vibroacoustics · Biot

## 1 Introduction

Porous materials are widely used in the aerospace, automotive, and construction industry to improve the vibro-acoustic isolation and transmission behaviour of structural and non-structural components see, e.g., [1, 2, 3].

<sup>1</sup> Centre for Structural Engineering and Informatics, Faculty of Engineering, The University of Nottingham, UK .

<sup>2</sup> Institute for Structural Engineering and Aseismic Research School of Civil Engineering, National Technical University of Athens, Greece, E-mail: savtri@mail.ntua.gr .

<sup>3</sup> Matelys - Research Lab 7 rue des Maraîchers Bâtiment B 69120 Vaulx-en-Velin, France

Over the past 10 years, an increasing and radical shift to additive manufacturing technologies has further enabled the development of material layouts tailor made to specific acoustic properties; these often come in polygonal and tessellated geometries, see, e.g., [4, 5].

The vibro-acoustic behaviour of two-phase porous media is described through structural and visco-inertial-thermal phenomena exhibited by the solid skeleton and the pore-fluid, respectively. The classical Helmholtz theory [6] can be used to describe the behaviour of very stiff materials, where the elastic behaviour of the solid skeleton can be safely ignored under the rigid motionless skeleton assumption [7]. In such cases, an equivalent fluid description [8] provides a complete characterization of the acoustic behaviour of the medium. However, there are certain resonance behaviours manifesting due to elastic effects that cannot be captured through the Helmholtz equation. In such cases, the rigid-skeleton assumption fails and one requires the Biot formulation for elastic wave propagation through poroelastic media [9, 10].

The Biot  $\mathbf{u} - \mathbf{U}$  formulation, where the primary variables are the solid skeleton and pore-fluid displacements, i.e.,  $\mathbf{u}$  and  $\mathbf{U}$ , require 4 and 6 degrees of freedom (DoFs) per node in the 2-D and 3-D cases, respectively. An alternative mixed  $\mathbf{u} - p$  formulation was developed in [11], where the primary field variables are solid-skeleton displacements  $\mathbf{u}$  and pore-fluid pressures  $p$ . In this case, 3 and 4 DoFs per node are required in the 2-D and 3-D cases, respectively. This reduction in the number of DoFs proves significant when solving over large scale domains. However, this formulation requires a reworking of the original Biot parameters.

This limitation is addressed in [12], where the dissipation parameters are decoupled from the rest of the formulation. These dissipation parameters are computed

Parameter	Description	Value	Units
$\sigma_s$	in-vacuo stress tensor		$N \cdot m^{-2}$
$\varepsilon_s$	infinitesimal strain tensor		-
E	Young's modulus		$N \cdot m^{-2}$
$\nu$	Poisson's ratio		-
$\eta_s(\omega)$	structural loss factor		-
$\tilde{D}$	elastic constitutive tensor		$N \cdot m^{-2}$
$\tilde{\rho}$	modified Biot density		$kg \cdot m^{-3}$
$\tilde{\rho}_{eq}$	dynamic mass density		$kg \cdot m^{-3}$
$\tilde{K}_{eq}$	dynamic bulk modulus		$N \cdot m^{-2}$
$\tilde{\gamma}$	coupling factor		-
$\omega$	angular frequency		$rad \cdot s^{-1}$
$\phi$	porosity		-
$\rho_s$	solid skeleton-material density		$kg \cdot m^{-3}$
$\rho_0$	air density at rest	1.2042	$kg \cdot m^{-3}$
$\rho_1$	solid skeleton-frame density		$kg \cdot m^{-3}$
$K_b$	porous skeleton bulk modulus at constant pressure		$N \cdot m^{-2}$
$K_s$	solid skeleton-material bulk modulus		$N \cdot m^{-2}$
$K_f$	fluid bulk modulus		$N \cdot m^{-2}$
$\sigma$	static airflow resistivity		$N \cdot s \cdot m^{-4}$
$\alpha_\infty$	high frequency limit of dynamic tortuosity		-
A	viscous characteristic length		m
$A'$	thermal characteristic length		m
$k'_0$	static thermal permeability		$m^2$
$c_{air}$	speed of sound in air	343.377	$m \cdot s^{-1}$
$z_{air}$	impedance of air	413.4807	$kg \cdot m^{-2} \cdot s^{-1}$
$P_0$	atmospheric pressure	101,325	$N \cdot m^{-2}$
$C_p$	specific heat of fluid at constant pressure	$1.0024 \times 10^3$	$J \cdot kg^{-1}$
$\eta$	dynamic viscosity	$1.8214 \times 10^{-5}$	$N \cdot s \cdot m^{-2}$
$\gamma$	adiabatic index	1.4012	-
$\alpha$	sound absorption coefficient		-
$\mathcal{T}$	sound transmission loss coefficient		-
$\kappa$	thermal conductivity	0.0257	$W \cdot m^{-1} \cdot K^{-1}$
k	wave number of acoustic excitation		$m^{-1}$

**Table 1** Material parameters used in the Biot  $\mathbf{u} - p$  formulation.

through analytic, empirical and semi-phenomenological models [13], which in turn, depend on macroscopic mechanical, acoustical, thermal and geometrical properties. Characterization of these properties through experimental or sub-scale modelling approaches [14, 15] is a challenging task, and as a result, not all parameters are always readily available. Here, one can insert a chosen dissipation model depending on the accuracy required and the number of macroscopic parameters available, e.g. a six parameter model - Johnson, Champoux, Allard, Lafarge (JCAL) model [16, 17, 18], or a single parameter Delany-Bazley-Miki (DBM) model [19].

Solving the aforementioned equations using classical finite-element techniques involves meshing the domain with quadrilateral or triangular elements. Using such elements to resolve complex shaped mesoscale heterogeneous morphologies necessitate fine resolutions, thus rendering the problem expensive. Optimal mesh discretizations would aid in augmenting the efficiency of the method. This motivates the investigation of numerical techniques that can handle flexible element geometries.

Polygonal finite elements PFEM [20, 21, 22] are used in a wide range of applications where one encounters complicated interface and inclusion geometries as in the case of e.g., topology and shape optimization [23, 24], fracture and damage modelling [25, 26, 27], contact mechanics [28], and fluid-structure interaction problems [29]. Defining shape functions over arbitrary polygonal domains is an active field of research and encompasses a large family of approaches. These include Wachspress [30, 31], natural neighbour [32, 33], mean-value coordinate [34, 35] and maximum entropy [36, 37] shape functions. A detailed summary collating advances in these polygonal shape functions is provided in [38]. The method involves treating these typically non-polynomial functions with special numerical schemes [39], or standard quadrature rules over sub-triangulated domains. Sub-optimal convergence rates are observed due to the errors arising from numerical integration of complicated non-polynomial functions. Employing higher quadrature rules to minimize this error can significantly drive up computational costs, especially in problems where iterative solutions are necessary, e.g., spectral problems, time domain analysis, topology optimization etc. The Virtual Element Method (VEM) [40, 41, 42, 43, 44, 45, 46] is a relatively recent technique introduced into the computational mechanics community to specifically address these shortcomings.

The VEM circumvents the problem of creating polygonal basis functions over non-standard element geometries by avoiding explicit definitions altogether. The trial and test functions spaces are enriched by allow-

ing potentially non-polynomial expressions that are defined implicitly through precisely chosen degrees of freedom over the element domain. These implicit definitions solve the problem of numerically or analytically computing polygonal basis functions. Generalized inter-element conformity and continuity requirements [47] are enforced by preserving the polynomial accuracy over element boundaries [40]. Extensions to curved geometries is a new development [48, 49, 50]. This method is being applied extensively in fracture mechanics [51, 52, 53], modelling of structures [54, 55, 56], topology and shape optimization [24], different problems in elasticity [57, 58, 59, 60, 61], contact and micro-mechanics [62, 63], composite materials [64], sound propagation in solid or fluid, i.e., uncoupled, domains [65, 66] and very recently in electro-magneto-mechanical couplings [67]. The VEM has been used in [68] to treat solid domains for reservoir modelling, considering also the case of fracture propagation [69] using a combined Discrete Element-Virtual Element approach. With regards to fluid domains, the case of Darcy and Brinkman flow has been addressed using the VEM in [70, 71].

Naturally, mixed VEM formulations have emerged over the past years to address elliptic problems [42, 72, 73]. This paved the way for extended applications in poromechanics such as mixed finite-volume discretizations [74] and three field formulations for the Biot consolidation equations [75, 76]. Very recently, multiphase problems pertaining to miscible fluids have been treated in [77]. A hybridised MFD-VEM has been developed for a similar application in [78] considering the case of Darcy flow in elastic domains under quasi-static loading conditions. Further to the current state-of-the-art, in this work we harness the power of the VEM vis-à-vis its ability to resolve complex geometries and examine the case of wave propagation in poro-elastic domains considering all the pertinent inertial and viscous terms arising from the solid to fluid couplings; this is a direction not yet explored in the literature.

Within this context, a novel VEM formalism is derived to resolve waves propagating in poro-elastic domains. To achieve this, the weak form of the Biot governing equations is introduced and the appropriate virtual spaces are defined. Next, the expansion coefficients of the VEM projection operators pertinent to the fully coupled vibro-acoustics setting are derived. Finally, we introduce the appropriate definitions for the resulting elastic, mass, fluid kinetic, fluid compressibility, and coupling consistency and stability terms of the VEM formulation. Through a set of benchmarks, we investigate the merits and potential bottlenecks of the scheme in terms of solution accuracy and computational efficiency. Further, we examine the merits of a node-

insertion scheme to treat the problem of non-conforming meshes arising in layered porous materials. We further examine the applicability of the method to resolve acoustic waves in composites with tortuous inclusions.

In Section 2, the strong and weak forms of the governing equations are presented. The VEM discretization procedure developed in this work is discussed in Section 3. The computation of the associated state matrices are discussed extensively in Section 4. The solution procedure is briefly shown in Section 5. Numerical examples are finally provided in Section 6.

## 2 Preliminaries

### 2.1 Strong form

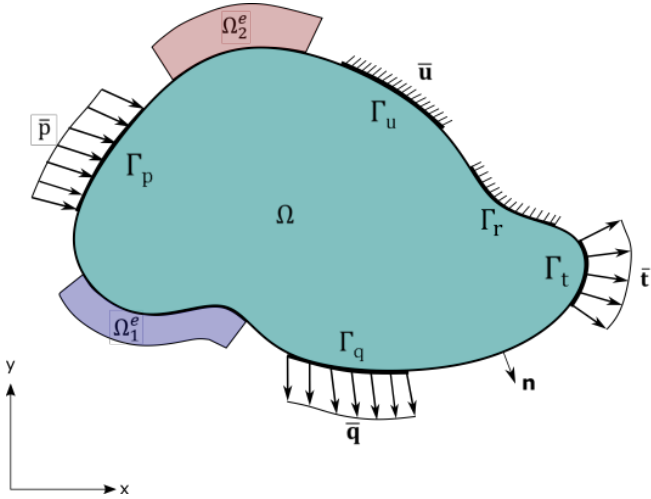


**Fig. 1** A poro-elastic domain  $\Omega$  subjected to acoustic and mechanical excitations.

A generalized continuous two-dimensional poroelastic domain  $\Omega \in \mathbb{R}^d$ ,  $d = 2$  with a boundary  $\Gamma$  is shown in Fig. 1. The domain  $\Omega$  is surrounded by arbitrary neighbouring domains  $\Omega_1^e$  and  $\Omega_2^e$ . These neighbouring domains may be elastic (solid), acoustic (fluid) or porous domains. The domain is kinematically constrained over  $\Gamma_u$  with prescribed displacements  $\bar{\mathbf{u}}$ . An acoustic excitation  $\bar{p}$  is enforced over  $\Gamma_p$ . Tractions  $\bar{\mathbf{t}}$  and volume flux  $\bar{\mathbf{q}}$  are applied over  $\Gamma_t$  and  $\Gamma_q$ , respectively. The boundary domains are constructed such that  $\Gamma_u \cap \Gamma_t = \emptyset$  and  $\Gamma_p \cap \Gamma_q = \emptyset$ . There is no restriction on the overlap of  $\Gamma_u$ ,  $\Gamma_p$  or  $\Gamma_t$ ,  $\Gamma_q$ . These overlaps are indeed encountered in defining interface coupling conditions. An impedance-type Robin boundary is also provided over  $\Gamma_r$ .

In this work, the mixed  $\mathbf{u} - p$  formulation [11] is employed. The corresponding momentum balance equa-

tions at a specific angular frequency  $\omega$  are defined as

$$\operatorname{div}(\boldsymbol{\sigma}_s) + \omega^2 \tilde{\rho} \mathbf{u} = -\tilde{\gamma} \nabla p \quad (1a)$$

$$\frac{\Delta p}{\tilde{\rho}_{\text{eq}}} + \omega^2 \frac{p}{\tilde{K}_{\text{eq}}} = \omega^2 \tilde{\gamma} \operatorname{div}(\mathbf{u}) \quad (1b)$$

for the solid and the fluid phase, respectively. In Eqs. (1),  $\boldsymbol{\sigma}_s$  is the *in-vacuo* stress tensor, i.e., the stresses present in the drained configuration. Furthermore,  $\tilde{\rho}$  is the modified Biot density,  $\tilde{\rho}_{\text{eq}}$  is the dynamic mass density,  $\tilde{K}_{\text{eq}}$  is the dynamic bulk modulus, and  $\tilde{\gamma}$  is the Biot coupling factor, respectively.

Under the assumption of linear elasticity, the solid phase constitutive equations are defined as

$$\boldsymbol{\sigma}_s = \tilde{\mathbb{D}} \varepsilon_s(\mathbf{u}), \quad (2)$$

where the elastic constitutive tensor  $\tilde{\mathbb{D}}$  depends on the modified Young's modulus  $\tilde{E}$  and the Poisson's ratio  $\nu$ ,

$$\tilde{\mathbb{D}} \equiv \tilde{\mathbb{D}}(\tilde{E}, \nu), \quad (3)$$

and  $\varepsilon_s(\cdot)$  is the infinitesimal strain operator, which assumes the following form

$$\varepsilon_s(\mathbf{u}) = \frac{1}{2} (\nabla \mathbf{u} + (\nabla \mathbf{u})^T). \quad (4)$$

The modified Young's modulus  $\tilde{E}$  in Eq. (3) is expressed as

$$\tilde{E} = E(1 + j\eta_s(\omega)), \quad (5)$$

where  $E$  and  $\eta_s(\omega)$  are the Young's modulus and the structural loss factor, respectively while  $(\tilde{\cdot})$  denotes the complex-valued and frequency dependent nature of it's argument. The symbol  $j$  stands for the unit complex number  $j = \sqrt{-1}$ .

The thermal and visco-inertial dissipation effects of the pore-fluid are captured by the dynamic bulk modulus  $\tilde{K}_{\text{eq}}$  and the dynamic mass density  $\tilde{\rho}_{\text{eq}}$ , respectively. The expressions for these quantities are provided by a chosen semi-phenomenological dissipation model, (e.g., the JCAL and DBM models). The JCAL model is defined as

$$\tilde{\rho}_{\text{eq}}(\omega) = \frac{\alpha_\infty \rho_0}{\phi} \left[ 1 + \frac{\sigma \phi}{j\omega \rho_0 \alpha_\infty} \sqrt{1 + j \frac{4\alpha_\infty^2 \eta \rho_0 \omega}{\sigma^2 \Lambda^2 \phi^2}} \right] \quad (6a)$$

$$\tilde{K}_{\text{eq}}(\omega) = \frac{\gamma P_0 / \phi}{\gamma - (\gamma - 1)A}, \quad (6b)$$

where  $A$  is equal to

$$A = \left[ 1 - j \frac{\phi \kappa}{k'_0 C_p \rho_0 \omega} \sqrt{1 + j \frac{4k'^2 C_p \rho_0 \omega}{\kappa \Lambda'^2 \phi^2}} \right]^{-1}. \quad (7)$$

The macroscopic material parameters  $\alpha_\infty$ ,  $\sigma$ ,  $\eta$ ,  $\Lambda$ ,  $\Lambda'$ ,  $\gamma$ ,  $P_0$ ,  $k'_0$ ,  $C_p$  and  $\kappa$  denote the high frequency limit of dynamic tortuosity, static airflow resistivity, dynamic viscosity, viscous and thermal characteristic lengths, adiabatic index, atmospheric pressure, static thermal permeability, specific heat at constant pressure and thermal conductivity. A concise list of the expressions for all semi-phenomenological models is provided in [13]. The modified Biot density  $\tilde{\rho}$  is computed:

$$\tilde{\rho} = \tilde{\rho}_{11} - \frac{\tilde{\rho}_{12}^2}{\tilde{\rho}_{22}} \quad (8a)$$

$$\tilde{\rho}_{11} = \rho_1 - \tilde{\rho}_{12} \quad (8b)$$

$$\tilde{\rho}_{12} = \phi\rho_0 - \tilde{\rho}_{22} \quad (8c)$$

$$\tilde{\rho}_{22} = \phi^2\tilde{\rho}_{\text{eq}}. \quad (8d)$$

Here, the density of the solid frame  $\rho_1$  is evaluated by  $\rho_1 = (1-\phi)\rho_s$ , where  $\rho_s$  is the density of the constituent material of the solid-skeleton. The symbol  $\phi$  denotes the porosity of the material and  $\rho_0$  represents the density of air at rest. The coupling factor  $\tilde{\gamma}$  is expressed as follows:

$$\tilde{\gamma} = \phi \left( \frac{\tilde{\rho}_{12}}{\tilde{\rho}_{22}} - \frac{\tilde{Q}}{\tilde{R}} \right). \quad (9)$$

The coefficient  $\tilde{Q}$  captures the elastic coupling behaviour between both phases. Parameter  $\tilde{R}$  corresponds to the bulk modulus of a fluid occupying a volume fraction  $\phi$  of the porous media under consideration. These assume the forms:

$$\tilde{Q} = \frac{\left[1 - \phi - \frac{K_b}{K_s}\right]\phi K_s}{\tilde{D}} \quad (10a)$$

$$\tilde{R} = \frac{\phi^2 K_s}{\tilde{D}} \quad (10b)$$

$$\tilde{D} = 1 - \phi - \frac{K_b}{K_s} + \phi \frac{K_s}{K_f}, \quad (10c)$$

where  $K_b$  is the bulk modulus of the porous skeleton subject to constant air pressure,  $K_s$  is the the bulk modulus of the constituent material of the skeleton frame and  $K_f$  denotes the fluid bulk modulus. These coefficients can be used to compute the total stress using the principle of equivalent stress:

$$\boldsymbol{\sigma}_t(\mathbf{u}, \mathbf{U}) = \boldsymbol{\sigma}_s - c\mathbb{I}, \quad (11)$$

where  $\boldsymbol{\sigma}_t$  and  $\mathbb{I}$  represent the total stress tensor of the material and identity tensor, respectively. The total stress  $\boldsymbol{\sigma}_t$  is a function of both the solid skeleton displacements  $\mathbf{u}$  and fluid displacements  $\mathbf{U}$ . The constant  $c$  has the following expression:

$$c = \phi \left( 1 + \frac{\tilde{Q}}{\tilde{R}} \right).$$

The fluid displacement  $\mathbf{U}$  can be defined in terms of the primary variables  $\mathbf{u}$  and  $p$ :

$$\mathbf{U} = \frac{1}{\omega^2 \phi \tilde{\rho}_{\text{eq}}} \nabla p - \frac{\tilde{\rho}_{12}}{\tilde{\rho}_{22}} \mathbf{u}. \quad (12)$$

The material parameters involved in this model are summarized in Table 1.

The coupled system of Eqs. 1 is subjected to the following set of essential

$$\mathbf{u} = \bar{\mathbf{u}} \text{ on } \Gamma_u, \quad p = \bar{p} e^{-j\mathbf{k} \cdot \mathbf{x}} \text{ on } \Gamma_p, \quad (13)$$

natural

$$\mathbf{t} = \bar{\mathbf{t}} \text{ on } \Gamma_t, \quad \mathbf{q} = \bar{\mathbf{q}} \text{ on } \Gamma_q, \quad (14)$$

and impedance boundary conditions

$$z(\theta) \nabla p \cdot \mathbf{n} + j\omega \tilde{\rho}_{\text{eq}} p = \bar{g} \text{ on } \Gamma_r, \quad (15)$$

respectively, where  $\bar{\mathbf{u}}$  and  $\bar{p}$  denote Dirichlet-type boundary values whereas  $\bar{\mathbf{t}}$  and  $\bar{\mathbf{q}}$  denote Neumann-type boundary values, respectively. For a time-harmonic acoustic excitation of amplitude  $\bar{p}$  incident at an angle  $\theta$ , the vector valued wave number is represented by  $\mathbf{k} = [k\cos(\theta), k\sin(\theta)]$ , where  $k = \omega/c_{\text{air}}$ . The vector  $\mathbf{x} = [x, y]^T$  denotes the coordinates of a point on the incident face  $\Gamma_p$ . A Robin-type boundary value  $\bar{g}$  is specified over  $\Gamma_r$  where  $z$  denotes an impedance constant  $z(\theta) = z_{\text{air}}/\cos(\theta)$ . The parameters  $c_{\text{air}}$  and  $z_{\text{air}} = \rho_0 c_{\text{air}}$  denote the speed of sound in air and impedance of air, respectively. For our purposes, we take  $\bar{g} = 0$  [79].

## 2.2 Weak form

The weak form of Eq. (1) is derived by multiplying each expression with the relevant test functions  $\delta\mathbf{u}$  and  $\delta p$

and integrating over the entire domain:

Find  $(\mathbf{u}, p) \in \mathcal{V}^u \times \mathcal{V}^p := [\mathcal{H}^1(\Omega)]^d \times [\mathcal{H}^1(\Omega)]$ ,  
 $d = 2$ , such that:

*Solid phase*

$$\int_{\Omega} \boldsymbol{\sigma}_s(\mathbf{u}) : \boldsymbol{\varepsilon}_s(\delta \mathbf{u}) d\Omega - \omega^2 \int_{\Omega} \tilde{\rho} \mathbf{u} \cdot \delta \mathbf{u} d\Omega$$

$$- \int_{\Omega} \tilde{\gamma} \nabla p \cdot \delta \mathbf{u} d\Omega - \underbrace{\int_{\Gamma_t} (\boldsymbol{\sigma}_s \cdot \mathbf{n}) \cdot \delta \mathbf{u} d\Gamma}_{I_1} = 0 \quad \forall \delta \mathbf{u} \in \mathcal{V}^u \quad (16a)$$

*Fluid phase*

$$\int_{\Omega} \frac{1}{\tilde{\rho}_{eq}} \nabla p \cdot \nabla \delta p d\Omega - \omega^2 \int_{\Omega} \frac{1}{\tilde{K}_{eq}} p \delta p d\Omega$$

$$- \omega^2 \int_{\Omega} \tilde{\gamma} \nabla \delta p \cdot \mathbf{u} d\Omega$$

$$+ \omega^2 \int_{\Gamma} \left( \tilde{\gamma} \mathbf{u} \cdot \mathbf{n} - \frac{1}{\omega^2 \tilde{\rho}_{eq}} \nabla p \cdot \mathbf{n} \right) \delta p d\Gamma = 0 \quad \forall \delta p \in \mathcal{V}^p, \quad (16b)$$

where  $\delta \mathbf{u}$  and  $\delta p$  are the variations in displacements and pressures such that  $\mathbf{u}, \delta \mathbf{u} \in \mathcal{V}^u$  and  $p, \delta p \in \mathcal{V}^p$ , respectively. The spaces  $\mathcal{V}^u$  and  $\mathcal{V}^p$  contain admissible displacements and pressures and assume standard 2-D  $[\mathcal{H}^1(\Omega)]^d$ ,  $d = 2$  and 1-D  $[\mathcal{H}^1(\Omega)]^d$ ,  $d = 1$  Hilbert spaces, respectively. Using Eq. (11), the boundary integral  $I_1$  in Eq. (16a) is modified to

$$I_1 = \int_{\Gamma_t} (\boldsymbol{\sigma}_t \cdot \mathbf{n} + c p \mathbb{I} \cdot \mathbf{n}) \cdot \delta \mathbf{u} d\Gamma. \quad (17)$$

Similarly, the boundary integral  $I_2$  in Eq. (16b) is decomposed into the relevant Neumann and Robin contributions according to the identity  $\Gamma \equiv \Gamma_q \cup \Gamma_r$ :  $I_2 = I_2^{\Gamma_q} + I_2^{\Gamma_r}$ , where, employing Eq. (12) the following expression is eventually established

$$I_2^{\Gamma_q} = -\omega^2 \int_{\Gamma_q} (\mathbf{c} \mathbf{u} \cdot \mathbf{n} + \mathbf{w}_n) \delta p d\Gamma, \quad (18)$$

where  $\mathbf{w}_n = \phi(\mathbf{U} - \mathbf{u}) \cdot \mathbf{n}$  is the normal component of the fluid displacement relative to the solid skeleton. This is measured in volume per unit area of the bulk medium [80, 81]. Using Eq. (15), a simplified expression for  $I_2^{\Gamma_r}$  is obtained

$$I_2^{\Gamma_r} = \frac{j\omega}{z(\theta)} \int_{\Gamma_r} p \delta p d\Gamma. \quad (19)$$

Boundary Condition	Boundary Integrals
Acoustic	$I_1 = 0$
Excitation	$I_2 = 0$
Roller	$I_1 = 0$
Support	$I_2 = 0$
Clamped	$I_1 = 0$
Support	$I_2 = 0$
Anechoic	$I_1 = 0$
Termination	$I_2 = \frac{j\omega}{z(\theta)} \int_{\Gamma_r} p \delta p d\Gamma$

**Table 2** Boundary integrals

Primary Domain	Neighbour Domain	Boundary Integrals
Poroelastic	Acoustic	$I_1 = 0$ $I_2 = 0$ $I_1 = - \int_{\Gamma_t} c(p \mathbb{I} \cdot \mathbf{n}) \cdot \delta \mathbf{u} d\Gamma$
Poroelastic	Elastic	$I_2 = -\omega^2 \int_{\Gamma_q} c \mathbf{u} \cdot \mathbf{n} \delta p d\Gamma$
Poroelastic	Poroelastic	$I_1 = 0$ $I_2 = 0$

**Table 3** Interface coupling integrals

Is it to be noted that the solid skeleton normal displacements are not defined over  $\Gamma_r$ .

When subject to acoustic excitation, variations in  $\delta \mathbf{p}$  are zero. To ensure continuities, one requires  $\boldsymbol{\sigma}_t \cdot \mathbf{n} = -p \mathbb{I} \cdot \mathbf{n}$ . Using the result for classical sound absorbing materials, i.e.,  $c \approx 1$  [82],  $I_1 = I_2 = 0$ . The acoustic wave is simply imposed on the incident face as a pressure Dirichlet boundary (Eq. (13)). Considering roller or fully clamped supports, variations in  $\delta \mathbf{u}$  are zero. Further,  $\mathbf{u} \cdot \mathbf{n}$  and  $\mathbf{w}_n$  are zero as well. Consequently, once again,  $I_1 = I_2 = 0$ . Given an impedance-type anechoic termination,  $I_1 = 0$ ,  $I_2 = I_2^{\Gamma_r}$ . These integral conditions are tabulated in Table 2.

The coupling conditions encountered at the interface between  $\Omega$  and  $\Omega_e^1$ ,  $\Omega_e^2$  etc. need to be taken into account. They are critical to generating accurate predictive models of porous composites. These conditions are summarized in Table 3 and will not be derived here. For a more detailed discussion of the boundary conditions involved, see [82].

### 3 Virtual Element method for Biot vibro-acoustics

#### 3.1 Discretization

In this work, we harness the power of the VEM to treat arbitrary polygonal domains and discretize the coupled weak form Eqs. (16). Within this context, the

following finite-dimensional approximations are considered for the displacement

$$\mathbf{u}_h \approx \mathbf{u}, \quad \delta\mathbf{u}_h \approx \delta\mathbf{u} \in \mathcal{V}_h^u \subset \mathcal{V}^u \quad (20)$$

and pressure fields

$$p_h \approx p, \quad \delta p_h \approx \delta p \in \mathcal{V}_h^p \subset \mathcal{V}^p, \quad (21)$$

respectively, where  $\mathbf{u}_h, p_h$  are the discretized displacement and pressure trial functions and  $\delta\mathbf{u}_h, \delta p_h$  are the corresponding test functions. These functions are defined over approximating finite-dimensional subspaces  $\mathcal{V}_h^u$  and  $\mathcal{V}_h^p$ .

**Remark 1** This work concerns itself with a conforming Virtual Element Method. Consequently, it is reasonable to require that  $\mathcal{V}_h^u$  and  $\mathcal{V}_h^p$  are subspaces of the corresponding infinite dimensional  $\mathcal{V}^u$  and  $\mathcal{V}^p$  spaces. For a treatment of the non-conforming Virtual Element method for elliptic problems, see [45].

Substituting in the weak form and collecting terms gives rise to the following abstract weak formulation, i.e.,

$$\left\{ \begin{array}{l} \text{Find } (\mathbf{u}_h, p_h) \in \mathcal{V}_h^u \times \mathcal{V}_h^p \text{ such that :} \\ \\ \forall \delta\mathbf{u}_h \in \mathcal{V}_h^u, \\ a^\varepsilon(\mathbf{u}_h, \delta\mathbf{u}_h) - \omega^2 a^0(\mathbf{u}_h, \delta\mathbf{u}_h)_{\tilde{\rho}} - \\ a^{(\nabla,0)}(p_h, \delta\mathbf{u}_h)_{\tilde{\gamma}} - a^{0\Gamma}(p_h, \delta\mathbf{u}_h)_c = 0, \\ \\ \forall \delta p_h \in \mathcal{V}_h^p, \\ b^\nabla(p_h, \delta p_h)_{1/\tilde{\rho}_{eq}} - \omega^2 b^0(p_h, \delta p_h)_{1/\tilde{K}_{eq}} - \\ \omega^2 a^{(\nabla,0)}(\delta p_h, \mathbf{u}_h)_{\tilde{\gamma}} - a^{0\Gamma}(\mathbf{u}_h, \delta p_h)_c + \\ j\omega b^{0\Gamma}(p_h, \delta p_h)_{\frac{1}{z(\theta)}} = 0, \end{array} \right. \quad (22)$$

where  $a^{(\cdot)}(\cdot, \cdot)_{(\cdot)}$  and  $b^{(\cdot)}(\cdot, \cdot)_{(\cdot)}$  represent bilinear functional operators, which assume the following

Solid Phase

$$a^\varepsilon(\mathbf{u}_h, \delta\mathbf{u}_h) = \int_{\Omega_h} \boldsymbol{\sigma}_s(\mathbf{u}_h) : \boldsymbol{\varepsilon}_s(\delta\mathbf{u}_h) \, d\Omega \quad (23a)$$

$$a^0(\mathbf{u}_h, \delta\mathbf{u}_h)_{\tilde{\rho}} = \int_{\Omega_h} \tilde{\rho}\mathbf{u}_h \cdot \delta\mathbf{u}_h \, d\Omega \quad (23b)$$

Fluid Phase

$$b^\nabla(p_h, \delta p_h)_{\frac{1}{\tilde{\rho}_{eq}}} = \int_{\Omega_h} \frac{1}{\tilde{\rho}_{eq}} \nabla p_h \cdot \nabla \delta p_h \, d\Omega \quad (23c)$$

$$b^0(p_h, \delta p_h)_{\frac{1}{\tilde{K}_{eq}}} = \int_{\Omega_h} \frac{1}{\tilde{K}_{eq}} p_h \delta p_h \, d\Omega. \quad (23d)$$

$$b^{0\Gamma}(p_h, \delta p_h)_{\frac{1}{z(\theta)}} = \int_{\Gamma_{hr}} \frac{1}{z(\theta)} p_h \delta p_h \, d\Gamma. \quad (23e)$$

Phase coupling

$$a^{(\nabla,0)}(p_h, \delta\mathbf{u}_h)_{\tilde{\gamma}} = \int_{\Omega_h} \tilde{\gamma} \nabla p_h \cdot \delta\mathbf{u}_h \, d\Omega \quad (23f)$$

$$a^{0\Gamma}(p_h, \delta\mathbf{u}_h)_c = \int_{\Gamma_{ht}} c(p_h \mathbb{I} \cdot \mathbf{n}) \cdot \delta\mathbf{u}_h \, d\Gamma \quad (23g)$$

In Eqs. (23), the domain  $\Omega_h$  is the discretized approximation of the original domain geometry, i.e.,

$$\Omega_h = \bigcup_{\mathcal{K}_i \in \Omega_h} \mathcal{K}_i \approx \Omega \quad (24)$$

where  $\mathcal{K}_i, i = 1, \dots, n_{el}$  correspond to non-intersecting polygonal sub-domains, i.e., virtual elements as shown in Fig. 2. An arbitrary element is also shown in Fig. 2 with polynomial order  $k \geq 1$ . The vertex coordinates are given by  $\mathbf{x}_j, j = 1, \dots, N_v$ , where  $N_v$  is the number of edges; this equals the number of vertices. Each edge  $e_j, j = 1, \dots, N_v$  connects vertices  $\mathbf{x}_j$  and  $\mathbf{x}_{j+1}$  and contains  $k - 1$  internal nodes per edge. These internal nodes are labelled  $\mathbf{x}^e$ . The index  $h$  denotes the maximum diameter of all elements contained in  $\Omega_h$ . The discretized boundaries  $\Gamma_{hu}, \Gamma_{ht}, \Gamma_{hp}, \Gamma_{hq}$  and  $\Gamma_{hr}$  are also obtained in the same fashion.

**Remark 2** The fluid phase contribution  $a^{0\Gamma}(\mathbf{u}_h, \delta p_h)_c$  from Eq. (22) is evaluated as shown in Eq. (23g). However, the integration is performed over  $\Gamma_{hq}$ . Additionally, it is to be noted that the boundary forms  $a^{0\Gamma}(p_h, \delta\mathbf{u}_h)_c$  and  $b^{0\Gamma}(p_h, \delta p_h)$  are obtained as generalizations of the boundary and interface conditions provided in Tables 2-3.

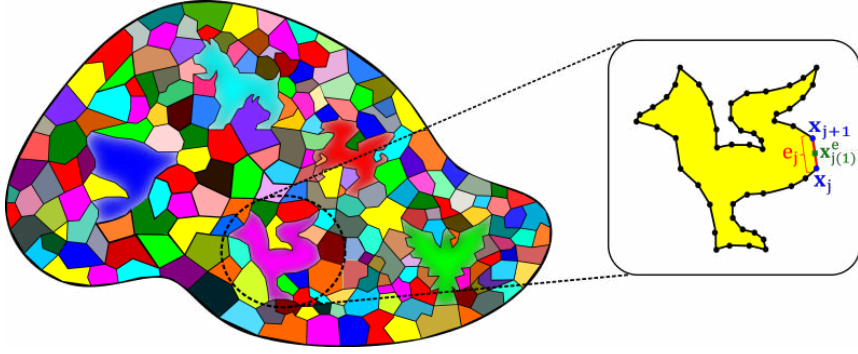


**Fig. 2** Discretized domain  $\Omega_h$  decomposed into  $n_{\text{el}}$  arbitrary potentially non-convex polygonal elements. An example chicken element with  $N_v = 51$  edges adapted from [24] is shown. The  $j$ th edge  $e_j$  connects vertex nodes  $\mathbf{x}_j$  and  $\mathbf{x}_{j+1}$ . A single edge node  $\mathbf{x}_{j(1)}^e$  is also illustrated.

Using Eq. (24), the bilinear forms of Eqs. (23a)-(23g) can be additively assembled from elemental contributions, i.e.,

The elemental contributions in Eqs. (25) assume the following form

Solid Phase

$$a_{\mathcal{K}_i}^\varepsilon(\mathbf{u}_h, \delta\mathbf{u}_h) = \int_{\mathcal{K}_i} \boldsymbol{\sigma}_s(\mathbf{u}_h) : \boldsymbol{\varepsilon}_s(\delta\mathbf{u}_h) d\Omega, \quad (26a)$$

$$a_{\mathcal{K}_i}^0(\mathbf{u}_h, \delta\mathbf{u}_h)_{\tilde{\rho}} = \int_{\mathcal{K}_i} \tilde{\rho}\mathbf{u}_h \cdot \delta\mathbf{u}_h d\Omega, \quad (26b)$$

Fluid Phase

$$b_{\mathcal{K}_i}^\nabla(p_h, \delta p_h)_{\frac{1}{\tilde{\rho}_{\text{eq}}}} = \int_{\mathcal{K}_i} \frac{1}{\tilde{\rho}_{\text{eq}}} \nabla p_h \cdot \nabla \delta p_h d\Omega, \quad (26c)$$

$$b_{\mathcal{K}_i}^0(p_h, \delta p_h)_{\frac{1}{\tilde{K}_{\text{eq}}}} = \int_{\mathcal{K}_i} \frac{1}{\tilde{K}_{\text{eq}}} p_h \delta p_h d\Omega, \quad (26d)$$

Solid Phase

$$a^\varepsilon(\mathbf{u}_h, \delta\mathbf{u}_h) = \sum_{i=1}^{n_{\text{el}}} a_{\mathcal{K}_i}^\varepsilon(\mathbf{u}_h, \delta\mathbf{u}_h), \quad (25a)$$

$$a^0(\mathbf{u}_h, \delta\mathbf{u}_h)_{\tilde{\rho}} = \sum_{i=1}^{n_{\text{el}}} a_{\mathcal{K}_i}^0(\mathbf{u}_h, \delta\mathbf{u}_h)_{\tilde{\rho}}, \quad (25b)$$

Fluid Phase

$$b^\nabla(p_h, \delta p_h)_{\frac{1}{\tilde{\rho}_{\text{eq}}}} = \sum_{i=1}^{n_{\text{el}}} b_{\mathcal{K}_i}^\nabla(p_h, \delta p_h)_{\frac{1}{\tilde{\rho}_{\text{eq}}}}, \quad (25c)$$

$$b^0(p_h, \delta p_h)_{\frac{1}{\tilde{K}_{\text{eq}}}} = \sum_{i=1}^{n_{\text{el}}} b_{\mathcal{K}_i}^0(p_h, \delta p_h)_{\frac{1}{\tilde{K}_{\text{eq}}}}, \quad (25d)$$

$$b^{0\Gamma}(p_h, \delta p_h)_{\frac{1}{z}} = \sum_{i=1}^{n_{\text{el}}} b_{\mathcal{K}_i}^{0\Gamma}(p_h, \delta p_h)_{\frac{1}{z}}, \quad (25e)$$

Phase coupling

$$a^{(\nabla,0)}(p_h, \delta\mathbf{u}_h)_{\tilde{\gamma}} = \sum_{i=1}^{n_{\text{el}}} a_{\mathcal{K}_i}^{(\nabla,0)}(p_h, \delta\mathbf{u}_h)_{\tilde{\gamma}}, \quad (25f)$$

$$a^{0\Gamma}(p_h, \delta\mathbf{u}_h)_c = \sum_{i=1}^{n_{\text{el}}} a_{\mathcal{K}_i}^{0\Gamma}(p_h, \delta\mathbf{u}_h)_c. \quad (25g)$$

$$b_{\mathcal{K}_i}^{0\Gamma}(p_h, \delta p_h)_{\frac{1}{z(\theta)}} = \int_{\Gamma_{h,r}^{\mathcal{K}_i}} \frac{1}{z(\theta)} p_h \delta p_h d\Gamma, \quad (26e)$$

$$a_{\mathcal{K}_i}^{(\nabla,0)}(p_h, \delta\mathbf{u}_h)_{\tilde{\gamma}} = \int_{\mathcal{K}_i} \tilde{\gamma} \nabla p_h \cdot \delta\mathbf{u}_h d\Omega, \quad (26f)$$

$$a_{\mathcal{K}_i}^{0\Gamma}(p_h, \delta\mathbf{u}_h)_c = \int_{\Gamma_{h,t}^{\mathcal{K}_i}} c(p_h \mathbb{I} \cdot \mathbf{n}) \cdot \delta\mathbf{u}_h d\Gamma. \quad (26g)$$

Finally, the globally continuous displacement  $\mathbf{u}_h$  and pressure fields  $p_h$ , and their corresponding weight functions  $\delta\mathbf{u}_h$  and  $\delta p_h$  are discretized into piece-wise continuous functions over each element  $\mathcal{K}_i$  according to the following expressions

$$\mathbf{u}_h = \underbrace{[\Phi^u]}_{(n_{\text{dof}}^u \times 2)} {}^T \hat{\mathbf{u}}, \quad \delta\mathbf{u}_h = \underbrace{[\Phi^u]}_{(n_{\text{dof}}^u \times 2)} {}^T \hat{\delta\mathbf{u}}, \quad (27a)$$

$$p_h = \underbrace{[\Phi^p]}_{(n_{\text{dof}}^p \times 1)} {}^T \hat{p}, \quad \delta p_h = \underbrace{[\Phi^p]}_{(n_{\text{dof}}^p \times 1)} {}^T \hat{\delta p}, \quad (27b)$$

where  $\hat{\mathbf{u}}$ ,  $\delta\hat{\mathbf{u}}$ ,  $\hat{\mathbf{p}}$  and  $\delta\hat{\mathbf{p}}$  denote vectors containing element-wise trial and test nodal displacement and pressure values, respectively. The quantities  $n_{\text{dof}}^u$  and  $n_{\text{dof}}^p$  denote the number of DoFs for  $\mathcal{V}_h^u(\mathcal{K})$  and  $\mathcal{V}_h^p(\mathcal{K})$ .

The arrays  $[\Phi^u]$  and  $[\Phi^p]$  contain the canonical basis functions that span  $\mathcal{V}_h^u$  and  $\mathcal{V}_h^p$ , respectively. The conventional Bubnov-Galerkin FEM definition for these spaces for a  $k_{\text{th}}$  order method is provided below:

$$\mathcal{V}_h^u = [\mathcal{W}_h]^d, d = 2, \quad \mathcal{V}_h^p = [\mathcal{W}_h]^d, d = 1 \quad (28a)$$

$$\mathcal{W}_h = \{v \in [\mathcal{H}^1(\Omega) \cap C^0(\Omega_h)] : v|_{\mathcal{K}} \in \mathcal{V}_h^k(\mathcal{K}), \forall \mathcal{K} \in \Omega_h\}, \quad (28b)$$

where  $\mathcal{V}_h^k(\mathcal{K})$  has the following definition:

$$\mathcal{V}_h^k(\mathcal{K}) = \{v \in [\mathcal{H}^1(\mathcal{K}) \cap C^0(\mathcal{K})] : v_{,i}|_{\mathcal{K}} \in \mathbb{L}_k(\mathcal{K}), \text{ for } i = 1, \dots, d\}. \quad (29)$$

The canonical basis functions retain their classical properties

$$\begin{aligned} \Phi_i^u(\mathbf{x}_j) &= \delta_{ij}, \quad i = 1, \dots, n_{\text{dof}}^u \\ \Phi_i^p(\mathbf{x}_j) &= \delta_{ij}, \quad i = 1, \dots, n_{\text{dof}}^p \end{aligned} \quad (30)$$

and partition of unity properties

$$\sum_{i=1}^{n_{\text{dof}}^u} \Phi_i^u(\mathbf{x}_j) = 1, \quad \sum_{i=1}^{n_{\text{dof}}^p} \Phi_i^p(\mathbf{x}_j) = 1, \quad (31)$$

over  $\mathcal{V}_h^u(\mathcal{K})$  and  $\mathcal{V}_h^p(\mathcal{K})$  in the VEM formulation. These properties are exploited through the entire work to allow for implicit definitions for  $\mathbf{u}_h$  and  $p_h$ .

The term  $\mathbb{L}_{mak}(\mathcal{K})$  in Eq. (29) denotes  $k_{\text{th}}$  order Lagrange interpolating polynomials defined over an element domain  $\mathcal{K}$ . These polynomials spanning the FEM space are explicitly defined and fully dependent on the element geometry.

### 3.2 Virtual Element spaces

To accommodate element domains  $\mathcal{K}_i$  of arbitrary shapes, the VEM seeks to avoid explicit definitions of these basis functions. To facilitate this, certain restricting assumptions on the approximating subspace  $\mathcal{V}_h^k(\mathcal{K})$  need to be relaxed. This is done by enlarging the space to allow for potentially non-polynomial function definitions over the element interior. The associated enrichments provide desirable stabilisation properties and correctly capture the relevant kinematic modes of the element. Within this setting, the space  $\mathcal{V}_h^k(\mathcal{K})$  is defined as

$$\mathcal{V}_h^k(\mathcal{K}) = \{v \in [\mathcal{H}^1(\mathcal{K}) \cap C^0(\mathcal{K})] : v_{,i}|_e \in \mathbb{P}_k(e) \quad \forall e \in \partial\mathcal{K};$$

$$\Delta v_{,i}|_{\mathcal{K}} \in \mathbb{P}_{k-2}(\mathcal{K}), \text{ for } i = 1, \dots, d\},$$

(32)

where  $\mathbb{P}_k(\mathcal{K})$  denotes a  $k_{\text{th}}$  order polynomial space, which is spanned by appropriately defined monomials.

A significant point of departure from the FEM consists in a two-fold observation of Eq. (32). First, the VEM space  $\mathcal{V}_h^k(\mathcal{K})$  no longer requires its members to have exclusively polynomial definitions over the element interior. Second, the members are implicitly defined through carefully chosen DoFs, as defined in Table 4, where  $[\mathbb{M}_{k-2}(\mathcal{K})]^2$  and  $\mathbb{M}_{k-2}(\mathcal{K})$  contain scaled  $k - 2$  order monomials of dimensions  $d = 2$  and  $d = 1$ , respectively. The total number of DoFs for each VEM space is  $n_{\text{dof}}^u = 2N_v k + k(k-1)$  and  $n_{\text{dof}}^p = N_v k + k(k-1)/2$ , respectively. This is illustrated in Fig. 3 for an element with  $N_v = 7$  edges.

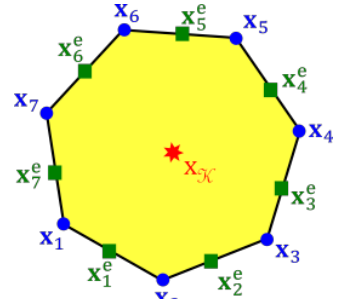


**Fig. 3** VEM DoFs illustrated for a  $k = 2$  element with  $N_v = 7$ . The centroid and element diameter are denoted by  $\mathbf{x}_{\mathcal{K}}$  and  $h_{\mathcal{K}}$ , respectively. This element contains  $n_{\text{dof}}^u = 30$  and  $n_{\text{dof}}^p = 15$  displacement and pressure DoFs, respectively.

**Remark 3** From Eq. (32), it is to be noted that these generalized non-polynomial functions assume continuous  $k_{\text{th}}$  order polynomial expressions over the element boundary. These polynomials can be uniquely determined through the corner and edge DoFs. This behaviour is consistent with the classical FEM definition provided in Eq. (29). The behaviour of the functions remain unknown within the element interior, except through a condition on its Laplacian, as defined in the area moment DoFs. Owing to the  $C^0$  conforming nature of the method induced by the governing equations, it is sufficient to retain the Laplacian operator, as originally defined for elliptic problems in [40]. Stricter conformity requirements, as encountered in higher order problems require different conditions within the element interior [56].

This approach solves the difficulty of providing explicit expressions for element basis functions. This implicit definition justifies the terminology *virtual elements* and *virtual spaces*. These bases are numerically evaluated and visualized in Fig. 4 for the heptagonal element

DoF Type	Location	$\mathcal{V}_h^u$		$\mathcal{V}_h^p$	
		Number of DoFs	Description	Number of DoFs	Description
Corner	vertices of $\mathcal{K}$	$N_C^u = 2N_v$	$\mathbf{u}_h(\mathbf{x}_j), j = 1, \dots, N_v$	$N_C^p = N_v$	$p_h(\mathbf{x}_j), j = 1, \dots, N_v$
Edge	internal boundary points on each edge of $\mathcal{K}$	$N_E^u = 2N_v(k - 1)$	$\mathbf{u}_h(\mathbf{x}_j^e), j = 1, \dots, k - 1$ for each edge	$N_E^p = N_v(k - 1)$	$p_h(\mathbf{x}_j^e), j = 1, \dots, k - 1$ for each edge
Area Moment	point lying in interior of domain $\mathcal{K}$	$N_A^u = 2\frac{k(k-1)}{2}$	$\frac{1}{ \mathcal{K} } \int_{\mathcal{K}} \mathbf{u}_h \cdot \mathbf{m} d\mathcal{K}$ $\forall \mathbf{m} \in [\mathbb{M}_{k-2}(\mathcal{K})]^2$	$N_A^p = \frac{k(k-1)}{2}$	$\frac{1}{ \mathcal{K} } \int_{\mathcal{K}} p_h \cdot \mathbf{m} d\mathcal{K}$ $\forall \mathbf{m} \in \mathbb{M}_{k-2}(\mathcal{K})$

**Table 4** Degrees of Freedom for  $\mathcal{V}_h^u(\mathcal{K})$  and  $\mathcal{V}_h^p(\mathcal{K})$ . For Area moment, the monomials belong to  $[\mathbb{M}_{k-2}(\mathcal{K})]^2$  and  $\mathbb{M}_{k-2}(\mathcal{K})$  spaces, respectively.

defined in Fig. 3. They are computed through a sub-scale boundary value problem over the element domain with appropriate kinematic constraints.

### 3.3 Virtual approximants at the element level

Following the discretization introduced in Eqs. (27), the displacement and pressure fields are split into their polynomial and non-polynomial components

$$\mathbf{u}_h = \mathbf{u}_h^\pi + (\mathbf{u}_h - \mathbf{u}_h^\pi), \quad \delta \mathbf{u}_h = \delta \mathbf{u}_h^\pi + (\delta \mathbf{u}_h - \delta \mathbf{u}_h^\pi), \quad (33)$$

$$p_h = p_h^\pi + (p_h - p_h^\pi), \quad \delta p_h = \delta p_h^\pi + (\delta p_h - \delta p_h^\pi). \quad (34)$$

This decomposition is illustrated in Fig. 5. The index  $\pi$  in Eqs. (33) and (34) denotes the polynomial component of the respective field. The polynomial components contain the consistent kinematic modes exhibited by the element. For the solid phase, these comprise rigid body and deformation modes.

Inserting Eqs. (33) into the definition for the solid phase specific local bilinear operators of Eqs. (26a) and (26b), the following expressions are derived

$$a_{\mathcal{K}}^\varepsilon(\mathbf{u}_h, \delta \mathbf{u}_h) = P(a_{\mathcal{K}}^\varepsilon) + NP(a_{\mathcal{K}}^\varepsilon) \quad (35)$$

$$a_{\mathcal{K}}^0(\mathbf{u}_h, \delta \mathbf{u}_h)_{\tilde{\rho}} = P(a_{\mathcal{K}}^0) + NP(a_{\mathcal{K}}^0) \quad (36)$$

where  $P(a_{\mathcal{K}}^\varepsilon)$  contains the polynomial and  $NP(a_{\mathcal{K}}^\varepsilon)$  the non-polynomial component of the operator, i.e.,

$$P(a_{\mathcal{K}}^\varepsilon) = a_{\mathcal{K}}^\varepsilon \left( \Pi_k^\varepsilon \mathbf{u}_h, \Pi_k^\varepsilon \delta \mathbf{u}_h \right) \quad (37)$$

$$NP(a_{\mathcal{K}}^\varepsilon) = a_{\mathcal{K}}^\varepsilon \left( (\mathbf{u}_h - \Pi_k^\varepsilon \mathbf{u}_h), (\delta \mathbf{u}_h - \Pi_k^\varepsilon \delta \mathbf{u}_h) \right), \quad (38)$$

and

$$P(a_{\mathcal{K}}^0) = a_{\mathcal{K}}^0 \left( \Pi_k^{0u} \mathbf{u}_h, \Pi_k^{0u} \delta \mathbf{u}_h \right)_{\tilde{\rho}} \quad (39)$$

$$NP(a_{\mathcal{K}}^0) = a_{\mathcal{K}}^0 \left( (\mathbf{u}_h - \Pi_k^{0u} \mathbf{u}_h), (\delta \mathbf{u}_h - \Pi_k^{0u} \delta \mathbf{u}_h) \right)_{\tilde{\rho}}, \quad (40)$$

respectively.

In Eqs. (37)-(40),  $\Pi_k^\varepsilon : \mathcal{V}_h^u(\mathcal{K}) \rightarrow [\mathbb{P}_k(\mathcal{K})]^2$  and  $\Pi_k^{0u} : \mathcal{V}_h^u(\mathcal{K}) \rightarrow [\mathbb{P}_k(\mathcal{K})]^2$  denote unknown projection operators that map the unknown field  $\mathbf{u}_h$  onto the polynomial space  $[\mathbb{P}_k(\mathcal{K})]^2$ . These projection operators arise from the fact that the operators  $\varepsilon_s(\cdot)$  and  $(\cdot)$  cannot directly interact with the unknown displacement field as the latter is not explicitly defined.

Naturally, this introduces additional error into the formulation. To minimize this error, the projection operators are computed on the basis of the following orthogonality conditions, i.e.,

$$\Pi_k^\varepsilon := a_{\mathcal{K}}^\varepsilon(\mathbf{u}_h - \Pi_k^\varepsilon \mathbf{u}_h, \mathbf{m}) = 0, \quad (41a)$$

$$\Pi_k^{0u} := a_{\mathcal{K}}^0(\mathbf{u}_h - \Pi_k^{0u} \mathbf{u}_h, \mathbf{m})_{\tilde{\rho}} = 0, \quad (41b)$$

$$\forall \mathbf{u}_h \in \mathcal{V}_h^u(\mathcal{K}), \mathbf{m} \in [\mathbb{P}_k(\mathcal{K})]^2,$$

**Remark 4** One would expect four terms in the r.h.s of Eqs. (35)-(36). However, two terms contribute zero energy due to the energetic orthogonality conditions defined in Eqs. (41). The polynomial terms in these expressions are called consistency terms as they comprise the consistent kinematic modes defined earlier.

Similarly, inserting Eqs. (34) into the fluid phase specific operators of Eqs. (26c) and (26d) results in the

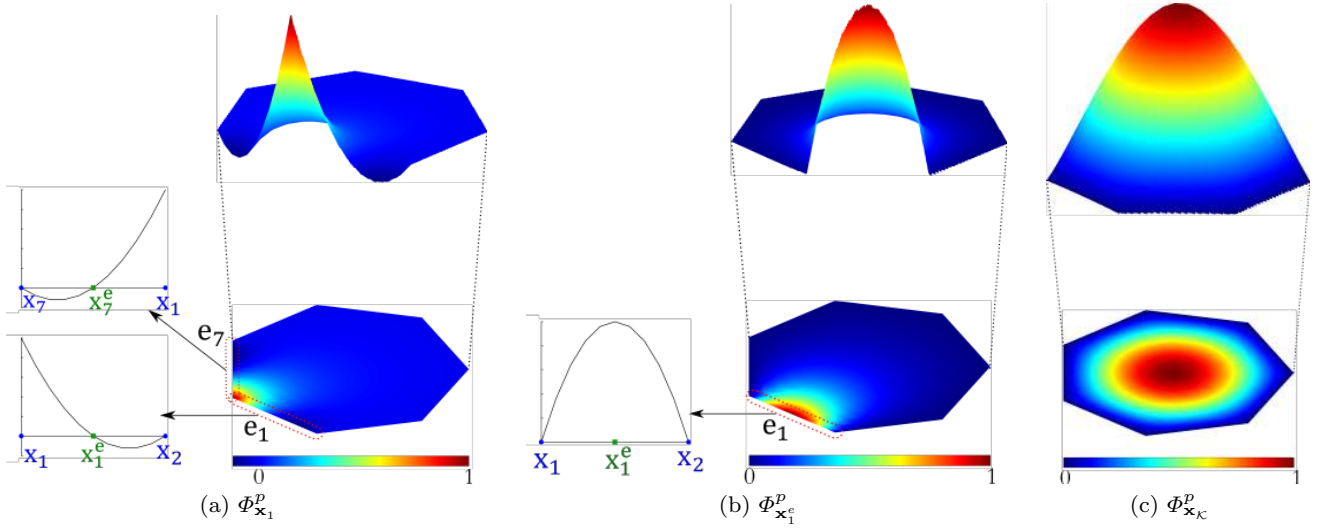


**Fig. 4** Canonical VEM basis functions defined over a heptagonal domain in Fig. 3 for (a) a vertex DoF, (b) an edge DoF and (c) an interior DoF. The non-zero quadratic forms recovered on (a) edges  $e_1$  and  $e_7$  for  $\Phi_{\mathbf{x}_1}^p$  and (b) edge  $e_1$  for  $\Phi_{\mathbf{x}_1^e}^p$  are uniquely defined exclusively through the relevant edge and vertex DoFs.

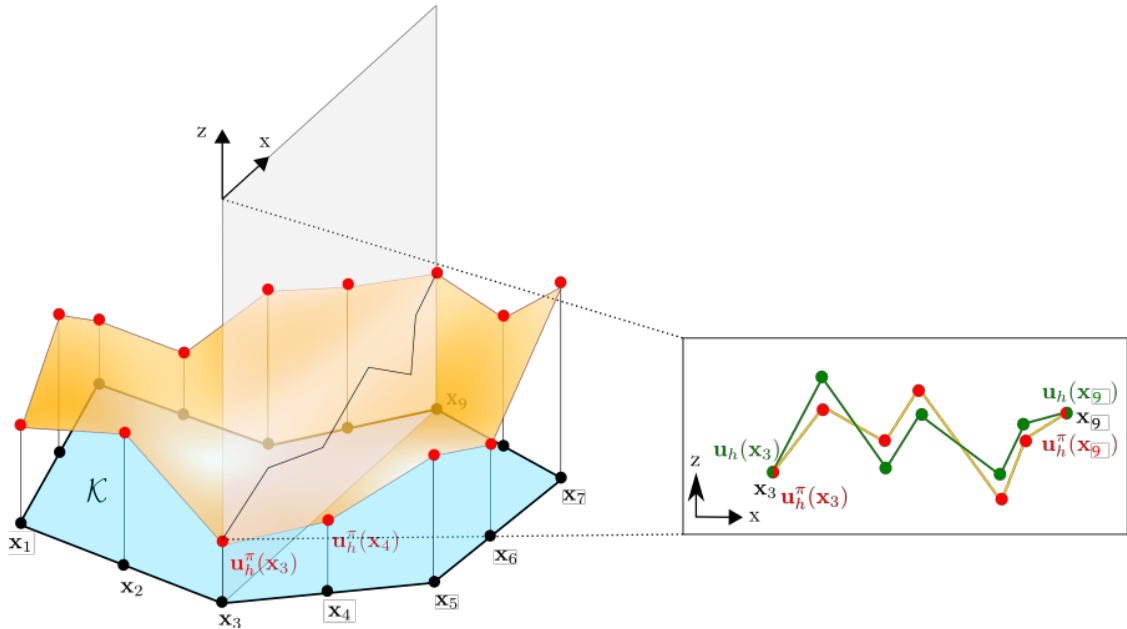


**Fig. 5** A discretized solution field and its polynomial components visualized over a polygonal element. A planar cross-section illustrates that  $\mathbf{u}_h$  and  $\mathbf{u}_h^\pi$  vary within the element interior, but coincide at the boundary.

following splits

$$b_{\mathcal{K}}^\nabla(p_h, \delta p_h)_{\frac{1}{\rho_{\text{eq}}}} = P(b_{\mathcal{K}}^\nabla) + NP(b_{\mathcal{K}}^\nabla) \quad (42)$$

$$b_{\mathcal{K}}^0(p_h, \delta p_h)_{\frac{1}{K_{\text{eq}}}} = P(b_{\mathcal{K}}^0) + NP(b_{\mathcal{K}}^0), \quad (43)$$

$$P(b_{\mathcal{K}}^\nabla) = b_{\mathcal{K}}^\nabla \left( \Pi_k^{\nabla p} p_h, \Pi_k^{\nabla p} \delta p_h \right)_{\frac{1}{\rho_{\text{eq}}}} \quad (44)$$

$$NP(b_{\mathcal{K}}^\nabla) = b_{\mathcal{K}}^\nabla \left( (p_h - \Pi_k^{\nabla p} p_h), (\delta p_h - \Pi_k^{\nabla p} \delta p_h) \right)_{\frac{1}{\rho_{\text{eq}}}}, \quad (45)$$

where the corresponding polynomial and non-polynomial arguments become

and

$$P(b_{\mathcal{K}}^0) = b_{\mathcal{K}}^0 \left( \Pi_k^{0p} p_h, \Pi_k^{0p} \delta p_h \right)_{\frac{1}{K_{eq}}} \quad (46)$$

$$NP(b_{\mathcal{K}}^0) = b_{\mathcal{K}}^0 \left( (p_h - \Pi_k^{0p} p_h), (\delta p_h - \Pi_k^{0p} \delta p_h) \right)_{\frac{1}{K_{eq}}}, \quad (47)$$

respectively. The projection operators  $\Pi_k^{\nabla p} : \mathcal{V}_k^p(\mathcal{K}) \rightarrow \mathbb{P}_k(\mathcal{K})$  and  $\Pi_k^{0p} : \mathcal{V}_k^p(\mathcal{K}) \rightarrow \mathbb{P}_k(\mathcal{K})$  arise from the action of  $\nabla(\cdot)$  and  $(\cdot)$  onto the unknown pressure field.

Similar to Eq. (41), the following orthogonality conditions are defined for the fluid phase projection operators

$$\Pi_k^{\nabla p} := b_{\mathcal{K}}^{\nabla} (p_h - \Pi_k^{\nabla p} p_h, m)_{\frac{1}{\tilde{\rho}_{eq}}} = 0, \quad (48a)$$

$$\Pi_k^{0p} := b_{\mathcal{K}}^0 (p_h - \Pi_k^{0p} p_h, m)_{\frac{1}{K_{eq}}} = 0, \quad (48b)$$

$$\forall p_h \in \mathcal{V}_h^p(\mathcal{K}), m \in \mathbb{P}_k(\mathcal{K}),$$

Finally, inserting Eqs. (33) and (34) into the coupling operator of Eq. (26f), the following expressions are derived, i.e.,

$$a_{\mathcal{K}}^{(\nabla,0)} = P(a_{\mathcal{K}}^{(\nabla,0)}) + NP(a_{\mathcal{K}}^{(\nabla,0)}) \quad (49)$$

with

$$P(a_{\mathcal{K}}^{(\nabla,0)}) = a_{\mathcal{K}}^{(\nabla,0)} \left( \Pi_k^{\nabla p} p_h, \Pi^{0u} \delta \mathbf{u}_h \right)_{\tilde{\gamma}} \quad (50)$$

$$NP(a_{\mathcal{K}}^{(\nabla,0)}) = a_{\mathcal{K}}^{(\nabla,0)} \left( (p_h - \Pi_k^{\nabla p} p_h), (\delta \mathbf{u}_h - \Pi^{0u} \delta \mathbf{u}_h) \right)_{\tilde{\gamma}}, \quad (51)$$

The subspaces  $[\mathbb{P}_k(\mathcal{K})]^2$  and  $[\mathbb{P}_k(\mathcal{K})]$  are spanned by vector and scalar valued scaled monomials belonging to  $[\mathbb{M}_k(\mathcal{K})]^2$  and  $[\mathbb{M}_k(\mathcal{K})]$ , respectively. The members of these monomial spaces are provided in Table 11 of Appendix A.

In these spaces, there exist members contributing zero energy to  $a_{\mathcal{K}}^{\varepsilon}(\cdot, \cdot)$  and  $b_{\mathcal{K}}^{\nabla}(\cdot, \cdot)$ , e.g.,  $\varepsilon_s([1, 0]^T) = [0, 0, 0]^T$ .  $\nabla(1) = [0, 0]^T$ . These zero energy modes are operator specific and collected in  $\mathbb{K}^{\varepsilon}(\mathcal{K})$  and  $\mathbb{K}^{\nabla p}(\mathcal{K})$ . They are called the *kernel* of the relevant operator. The projectors are computed without the kernel, to avoid spurious results arising from ill conditioned matrices. To this end, Eqs. (41) and (48) are redefined as:

$$\begin{cases} \Pi_k^{\varepsilon} := a_{\mathcal{K}}^{\varepsilon} (\mathbf{u}_h - \Pi_k^{\varepsilon} \mathbf{u}_h, \mathbf{m}) = 0 \\ \forall \mathbf{u}_h \in \mathcal{V}_h^u(\mathcal{K}), \mathbf{m} \in [\mathbb{M}_k(\mathcal{K})]^2 \setminus \mathbb{K}^{\varepsilon}(\mathcal{K}), \\ \Pi_k^{0u} := a_{\mathcal{K}}^0 (\mathbf{u}_h - \Pi_k^{0u} \mathbf{u}_h, \mathbf{m})_{\tilde{\rho}} = 0, \\ \forall \mathbf{u}_h \in \mathcal{V}_h^u(\mathcal{K}), \mathbf{m} \in [\mathbb{M}_k(\mathcal{K})]^2 \setminus \mathbb{K}^{0u}(\mathcal{K}), \end{cases} \quad (52)$$

and

$$\begin{cases} \Pi_k^{\nabla p} := b_{\mathcal{K}}^{\nabla} (p_h - \Pi_k^{\nabla p} p_h, m)_{\frac{1}{\tilde{\rho}_{eq}}} = 0, \\ \forall p_h \in \mathcal{V}_h^p(\mathcal{K}), m \in \mathbb{M}_k(\mathcal{K}) \setminus \mathbb{K}^{\nabla}(\mathcal{K}), \\ \Pi_k^{0p} := b_{\mathcal{K}}^0 (p_h - \Pi_k^{0p} p_h, m)_{\frac{1}{K_{eq}}} = 0 \\ \forall p_h \in \mathcal{V}_h^p(\mathcal{K}), m \in \mathbb{M}_k(\mathcal{K}) \setminus \mathbb{K}^{0p}(\mathcal{K}) \end{cases}, \quad (53)$$

respectively. It is to be noted that  $a_{\mathcal{K}}^0(\cdot, \cdot)$  and  $b_{\mathcal{K}}^0(\cdot, \cdot)$  contain empty kernels as they have no zero energy modes, i.e.,  $\mathbb{K}^{0u}(\mathcal{K}) = \mathbb{K}^{0p}(\mathcal{K}) = \emptyset$ . These operator kernels are provided in Table 12 in Appendix A.

**Remark 5** The optimality criteria used above ensure that the energies associated with the bilinear operators  $P(\cdot)$  are still computed exactly. This property is called polynomial  $k$ -consistency, see, e.g., [40].

To compute the  $\mathcal{L}_2$  projector  $\Pi_k^{0u}$ , an intermediate fifth projector  $\Pi_k^{\nabla u} := \mathcal{V}_h^u(\mathcal{K}) \rightarrow [\mathbb{P}_k(\mathcal{K})]^2$  is required [47]. This is a projector specific to the solid phase and is defined here for completeness

$$\Pi_k^{\nabla u} := a_{\mathcal{K}}^{\nabla} (\mathbf{u}_h - \Pi_k^{\nabla u} \mathbf{u}_h, \mathbf{m})_{\delta^*} = 0, \quad (54)$$

$$\forall \mathbf{u}_h \in \mathcal{V}_h^u(\mathcal{K}), \mathbf{m} \in [\mathbb{M}_k(\mathcal{K})]^2 \setminus \mathbb{K}^{\nabla u}(\mathcal{K}),$$

where  $\mathbb{K}^{\nabla u}$  denotes the kernel of  $a_{\mathcal{K}}^{\nabla}(\cdot, \cdot)$ . This operator is defined as follows:

$$a_{\mathcal{K}}^{\nabla} (\mathbf{u}_h, \delta \mathbf{u}_h)_{\delta^*} = \int_{\mathcal{K}} \delta^* \nabla \mathbf{u}_h \cdot \nabla \delta \mathbf{u}_h d\mathcal{K}, \quad (55)$$

where the material parameter  $\delta^*$  is an arbitrarily chosen scalar real valued number. The need for this additional projector is dealt with in greater detail in Section 3.4.2.

### 3.4 Computing the projectors

Following the revised definition of the projectors in Eqs. (52)-(54), the projected functions are expanded in terms of the appropriate monomial bases. The  $\mathcal{H}^1$  projectors, i.e.,  $\Pi_k^{\varepsilon}$ ,  $\Pi_k^{\nabla u}$ , and  $\Pi_k^{\nabla p}$  are expanded as

$$\Pi_k^{\varepsilon} \mathbf{u}_h = \sum_{i=1}^{n_k^u-3} \mathbf{m}_{i+3} \zeta_i^{\varepsilon}, \quad (56a)$$

$$\Pi_k^{\nabla u} \mathbf{u}_h = \sum_{i=1}^{n_k^u-2} \mathbf{m}_{i+2} \zeta_i^{\nabla u}, \quad (56b)$$

$$\Pi_k^{\nabla p} p_h = \sum_{i=1}^{n_k^p-1} \mathbf{m}_{i+1} \zeta_i^{\nabla p}, \quad (56c)$$

where  $\zeta_i^\varepsilon$  and  $\zeta_i^{\nabla u}$  are  $(1 \times n_{\text{dof}}^u)$  vectors of the unknown expansion coefficients. Conversely,  $\zeta_i^{\nabla p}$  is a  $(1 \times n_{\text{dof}}^p)$  vector. Each entry in the expansion vectors corresponds to a canonical basis function describing  $\mathbf{u}_h$  or  $p_h$ , contained in  $\Phi^u$  and  $\Phi^p$ , respectively (see Eq. (27)).

Eqs. (56a)-(56c) can be conveniently cast in matrix form as

$$\Pi_k^\varepsilon \mathbf{u}_h = \underbrace{\mathbf{m}^\varepsilon}_{(2 \times n_k^u - 3)} \underbrace{\zeta^\varepsilon}_{(n_k^u - 3 \times n_{\text{dof}}^u)}, \quad (57a)$$

$$\Pi_k^{\nabla u} \mathbf{u}_h = \underbrace{\mathbf{m}^{\nabla u}}_{(2 \times n_k^u - 2)} \underbrace{\zeta^{\nabla u}}_{(n_k^u - 2 \times n_{\text{dof}}^u)}, \quad (57b)$$

$$\Pi_k^{\nabla p} p_h = \underbrace{\mathbf{m}^{\nabla p}}_{(1 \times n_k^p - 1)} \underbrace{\zeta^{\nabla p}}_{(n_k^p - 1 \times n_{\text{dof}}^p)}, \quad (57c)$$

where the matrices  $\mathbf{m}^\varepsilon$ ,  $\mathbf{m}^{\nabla u}$ , and  $\mathbf{m}^{\nabla p}$  hold the appropriate monomial bases and  $\zeta^\varepsilon$ ,  $\zeta^{\nabla u}$ ,  $\zeta^{\nabla p}$  are arrays whose  $i_{th}$  row holds the vectors of expansion coefficients  $\zeta_i^\varepsilon$ ,  $\zeta_i^{\nabla u}$ , and  $\zeta_i^{\nabla p}$ , respectively.

Similarly, the  $\mathcal{L}^2$  projectors, i.e.,  $\Pi_k^{0u}$  and  $\Pi_k^{0p}$  are expanded as

$$\Pi_k^{0u} \mathbf{u}_h = \sum_{i=1}^{n_k^u} \mathbf{m}_i \zeta_i^{0u}, \quad (58a)$$

$$\Pi_k^{0p} p_h = \sum_{i=1}^{n_k^p} \mathbf{m}_i \zeta_i^{0p}, \quad (58b)$$

where  $\zeta_i^{0u}$  and  $\zeta_i^{0p}$  are  $(1 \times n_{\text{dof}}^u)$  and  $(1 \times n_{\text{dof}}^p)$  vectors, respectively.

Eqs. (58) are also cast in their corresponding matrix form, i.e.,

$$\Pi_k^{0u} \mathbf{u}_h = \underbrace{\mathbf{m}^{0u}}_{(2 \times n_k^u)} \underbrace{\zeta^{0u}}_{(n_k^u \times n_{\text{dof}}^u)} \quad (59)$$

and

$$\Pi_k^{0p} p_h = \underbrace{\mathbf{m}^{0p}}_{(1 \times n_k^p)} \underbrace{\zeta^{0p}}_{(n_k^p \times n_{\text{dof}}^p)}, \quad (60)$$

respectively, where the matrices  $\mathbf{m}^{0u}$  and  $\mathbf{m}^{0p}$  hold the monomial bases and  $\zeta^{0u}$ ,  $\zeta^{0p}$  are the corresponding arrays of the expansion coefficients.

The summation indices in Eqs. (56a)-(58b)  $n_k^u$  and  $n_k^p$  denote the number of vector and scalar valued monomials in  $[\mathbb{M}_k(\mathcal{K})]^2$  and  $\mathbb{M}_k(\mathcal{K})$  and their expressions are provided in Appendix A for completeness.

### 3.4.1 Computing the projectors $\Pi_k^\varepsilon$ , $\Pi_k^{\nabla u}$ , and $\Pi_k^{\nabla p}$

Inserting the expansion of Eq. (56a) into the orthogonality condition Eq. (52) and performing the necessary algebra the following system of equations is established with respect to the unknown expansion coefficients, i.e.,

$$\underbrace{\mathbf{G}^\varepsilon}_{(n_k^u - 3 \times n_k^u - 3)} \underbrace{\zeta^\varepsilon}_{(n_k^u - 3 \times n_{\text{dof}}^u)} = \underbrace{\mathbf{B}^\varepsilon}_{(n_k^u - 3 \times n_{\text{dof}}^u)}, \quad (61)$$

where  $\mathbf{G}^\varepsilon$  is an array with elements

$$G_{ij}^\varepsilon = \int_{\mathcal{K}} \boldsymbol{\varepsilon}_s(\mathbf{m}_{i+3})^T \boldsymbol{\sigma}_s(\mathbf{m}_{j+3}) d\mathcal{K}, \quad (62)$$

and  $\mathbf{B}^\varepsilon$  is an array whose  $j_{th}$  row is a vector

$$\mathbf{B}_j^\varepsilon = \int_{\mathcal{K}} \boldsymbol{\varepsilon}_s(\mathbf{u}_h)^T \boldsymbol{\sigma}_s(\mathbf{m}_{j+3}) d\mathcal{K}. \quad (63)$$

Similarly, imposing the orthogonality condition Eq. (54) on Eq. (56b), the following equation is established for the expansion coefficients of the projector  $\Pi_k^{\nabla u}$

$$\underbrace{\mathbf{G}^{\nabla u}}_{(n_k^u - 2 \times n_k^u - 2)} \underbrace{\zeta^{\nabla u}}_{(n_k^u - 2 \times n_{\text{dof}}^u)} = \underbrace{\mathbf{B}^{\nabla u}}_{(n_k^u - 2 \times n_{\text{dof}}^u)}, \quad (64)$$

where the matrices  $\mathbf{G}^{\nabla u}$ ,  $\mathbf{B}^{\nabla u}$  are defined as

$$G_{ij}^{\nabla u} = \int_{\mathcal{K}} (\nabla \mathbf{m}_{i+2})^T \delta^* \nabla \mathbf{m}_{j+2} d\mathcal{K}, \quad (65)$$

and

$$\mathbf{B}_j^{\nabla u} = \int_{\mathcal{K}} (\nabla \mathbf{u}_h)^T \delta^* \nabla \mathbf{m}_{j+2} d\mathcal{K}, \quad (66)$$

respectively.

Finally, inserting Eq. (56c) into the first of Eqs. (53), the following equation is established

$$\underbrace{\mathbf{G}^{\nabla p}}_{(n_k^p - 1 \times n_k^p - 1)} \underbrace{\zeta^{\nabla p}}_{(n_k^p - 1 \times n_{\text{dof}}^p)} = \underbrace{\mathbf{B}^{\nabla p}}_{(n_k^p - 1 \times n_{\text{dof}}^p)}, \quad (67)$$

where

$$G_{ij}^{\nabla p} = \int_{\mathcal{K}} (\nabla \mathbf{m}_{i+1})^T \frac{1}{\tilde{\rho}_{\text{eq}}} \nabla \mathbf{m}_{j+1} d\mathcal{K}, \quad (68)$$

and

$$\mathbf{B}_j^{\nabla p} = \int_{\mathcal{K}} (\nabla \mathbf{p}_h)^T \frac{1}{\tilde{\rho}_{\text{eq}}} \nabla \mathbf{m}_{j+1} d\mathcal{K}, \quad (69)$$

The terms  $G_{ij}^\varepsilon$ ,  $G_{ij}^{\nabla u}$ , and  $G_{ij}^{\nabla p}$  in Eqs. (62), (65), (68) are computable using numerical integration since

$\varepsilon_s(\cdot)$  and  $\nabla(\cdot)$  can be directly performed on the explicitly defined monomials (Appendix A). A standard Gauss-Legendre quadrature is sufficient as the integrands are composed wholly of polynomial-type terms. For  $k = 1$ , this is trivial as the integrand is a constant whereas for  $k \geq 2$ , numerical integration over sub-triangulated domains is required.

Conversely, the terms  $B_j^\varepsilon$ ,  $B_j^{\nabla u}$  and  $B_j^{\nabla p}$  cannot be evaluated in their current form as explicit definitions for the terms  $\mathbf{u}_h$  and  $p_h$  over the element domain interior do not exist. Performing integration by parts in Eq. (63) results in

$$\mathbf{B}_j^\varepsilon = \mathbf{B}_{bj}^\varepsilon + \mathbf{B}_{dj}^\varepsilon, \quad (70)$$

where

$$\mathbf{B}_{bj}^\varepsilon = \sum_{e \in \partial\mathcal{K}} \int_e \mathbf{u}_h \cdot (\boldsymbol{\sigma}(\mathbf{m}_{j+3}) \cdot \mathbf{n}^\varepsilon(e)) \, de, \quad (71)$$

and

$$\mathbf{B}_{dj}^\varepsilon = - \int_{\mathcal{K} \setminus \partial\mathcal{K}} \mathbf{u}_h \cdot (\operatorname{div}(\boldsymbol{\sigma}_s(\mathbf{m}_{j+3}))) \, d\mathcal{K}, \quad (72)$$

respectively, where  $\mathbf{n}^\varepsilon(e)$  collects the boundary direction cosines  $n_x(e)$  and  $n_y(e)$  and is expressed as

$$\mathbf{n}^\varepsilon(e) = \begin{bmatrix} n_x(e) & 0 & n_y(e) \\ 0 & n_y(e) & n_x(e) \end{bmatrix}^T. \quad (73)$$

Since  $\mathbf{u}_h$  is known over the boundary through the definitions of the corner and edge DoFs (Table 4), the boundary integral of Eq. (71) can be evaluated with a Gauss-Lobatto quadrature giving rise to the following expression

$$\mathbf{B}_{bj}^\varepsilon = \underbrace{\begin{bmatrix} B_{bj,1}^\varepsilon & \dots & B_{bj,N_B^u}^\varepsilon \end{bmatrix}}_{N_B^u = N_C^u + N_E^u} \underbrace{\begin{bmatrix} 0 & \dots & 0 \end{bmatrix}}_{N_A^u}. \quad (74)$$

Conversely, the area moment DoFs within the element interior (see Table 4, Fig. 3) are exploited to evaluate the interior domain integral  $\mathbf{B}_{dj}^\varepsilon$ . As there are no interior DoFs for  $k = 1$  methods, these integrals vanish. For order  $k \geq 2$ , the Laplacian condition defined in Eq. (32) is exploited. To this end, the term  $\operatorname{div}(\boldsymbol{\sigma}_s(\mathbf{m}_{j+3}))$  in Eq. (72) is expanded over the  $[\mathbb{M}_{k-2}(\mathcal{K})]^2$  basis giving rise to the following expression

$$\operatorname{div}(\boldsymbol{\sigma}_s(\mathbf{m}_{j+3})) = \sum_{\beta=1}^{n_{k-2}^u} d_{j\beta}^\varepsilon \mathbf{m}_\beta, \quad \forall \mathbf{m}_\beta \in [\mathbb{M}_{k-2}(\mathcal{K})]^2, \quad (75)$$

where the expansion coefficients  $d_{j\beta}^\varepsilon$  are obtained through inspection [83]. Substituting Eq. (75) in Eq. (72) the following expression is eventually established

$$\mathbf{B}_{dj}^\varepsilon = -|\mathcal{K}| \sum_{\beta=1}^{n_{k-2}^u} d_{j\beta}^\varepsilon \operatorname{dof}_{2kN_v+\beta}(\mathbf{u}_h) = -|\mathcal{K}| \mathbf{d}^\varepsilon \quad (76)$$

where the dof function denotes the evaluation of its argument at the indexed degree of freedom (see Eq. (142)), and

$$\mathbf{d}^\varepsilon = \left[ \overbrace{0 \cdots 0}^{N_B^u} \mid \overbrace{d_{j1}^\varepsilon \cdots d_{j(n_{k-2}^u)}^\varepsilon}^{N_A^u} \right]. \quad (77)$$

Combining Eqs. (74) and (76) and substituting in Eq. (70) provides the computed form of matrix  $\mathbf{B}^\varepsilon$ . Hence, Eq. (61) can be solved for the array of the expansion coefficients  $\zeta^\varepsilon$ . Substituting in Eq. (57a) the following expression is eventually derived for the projection operator  $\Pi_k^\varepsilon \mathbf{u}_h$

$$\Pi_k^\varepsilon \mathbf{u}_h = \mathbf{m}^\varepsilon [\mathbf{G}^\varepsilon]^{-1} \mathbf{B}^\varepsilon. \quad (78)$$

The right hand side matrices in Eqs. (64) and (67) are derived in a similar fashion. The derivations are provided in Appendix B for completeness. Similar to Eq. (78), the projection operators  $\Pi_k^{\nabla u} \mathbf{u}_h$  and  $\Pi_k^{\nabla p} p_h$  are evaluated according to the following expressions

$$\Pi_k^{\nabla u} \mathbf{u}_h = \mathbf{m}^{\nabla u} [\mathbf{G}^{\nabla u}]^{-1} \mathbf{B}^{\nabla u}, \quad (79a)$$

$$\Pi_k^{\nabla p} p_h = \mathbf{m}^{\nabla p} [\mathbf{G}^{\nabla p}]^{-1} \mathbf{B}^{\nabla p}. \quad (79b)$$

### 3.4.2 Computing the projectors $\Pi_k^{0u}$ and $\Pi_k^{0p}$

Within this vibro-acoustics setting, two additional  $\mathcal{L}^2$  projectors emerge. To evaluate these, Eqs. (58a) and (58b) are inserted into the second of Eqs. (52) and (53), respectively to obtain

$$\underbrace{\mathbf{G}^{0u}}_{(n_k^u \times n_k^u)} \underbrace{\zeta^{0u}}_{(n_k^u \times n_{\text{dof}}^u)} = \underbrace{\mathbf{B}^{0u}}_{(n_k^u \times n_{\text{dof}}^u)}, \quad (80a)$$

$$\underbrace{\mathbf{G}^{0p}}_{(n_k^p \times n_k^p)} \underbrace{\zeta^{0p}}_{(n_k^p \times n_{\text{dof}}^p)} = \underbrace{\mathbf{B}^{0p}}_{(n_k^p \times n_{\text{dof}}^p)}, \quad (80b)$$

where the terms  $\mathbf{G}^{0u}$  and  $\mathbf{G}^{0p}$  are arrays with elements

$$G_{ij}^{0u} = \int_{\mathcal{K}} (\mathbf{m}_i)^T \tilde{\rho} \mathbf{m}_j \, d\mathcal{K}, \quad (81a)$$

$$G_{ij}^{0p} = \int_{\mathcal{K}} (\mathbf{m}_i)^T \frac{1}{\tilde{K}_{\text{eq}}} \mathbf{m}_j \, d\mathcal{K}. \quad (81b)$$

The quantities  $\mathbf{B}^{0u}$  and  $\mathbf{B}^{0p}$  are arrays, whose  $j_{th}$  rows are

$$\mathbf{B}_j^{0u} = \int_{\mathcal{K}} (\mathbf{u}_h)^T \tilde{\rho} \mathbf{m}_j d\mathcal{K}, \quad (82a)$$

$$\mathbf{B}_j^{0p} = \int_{\mathcal{K}} (\mathbf{p}_h)^T \frac{1}{\tilde{K}_{eq}} \mathbf{m}_j d\mathcal{K}. \quad (82b)$$

Computing  $G_{ij}^{0u}$  and  $G_{ij}^{0p}$  in Eqs. (81a)-(81b) is straightforward. The terms  $\mathbf{B}_j^{0u}$  and  $\mathbf{B}_j^{0p}$  in Eqs. (82a)-(82b) however, are not computable solely through the DoFs of  $\mathbf{u}_h$  and  $\mathbf{p}_h$ . This is because the interior DoFs are defined for  $\mathbf{m} \in [\mathbb{M}_{k-2}(\mathcal{K})]^2$  and  $\mathbf{m} \in \mathbb{M}_{k-2}(\mathcal{K})$ , respectively. To alleviate this, we employ the procedure shown in [47, 84].

Hence, these integrals are computed through the existing DoFs of  $\mathcal{V}_h^u(\mathcal{K})$  and  $\mathcal{V}_h^p(\mathcal{K})$  when the current monomial has a degree lesser than or equal to  $k-2$ . Conversely, the integrals are evaluated using  $\Pi_k^{\nabla u}$  and  $\Pi_k^{\nabla p}$  when the order of the monomial under consideration is larger than  $k-2$ .

Following this procedure,  $\mathbf{B}_j^{0u}$  assumes the following form

$$\mathbf{B}_j^{0u} = \begin{cases} \mathbf{B}_{1j}^{0u}, & \text{if } 1 \leq j \leq n_{k-2}^u \\ \mathbf{B}_{2j}^{0u}, & \text{if } n_{k-2}^u < j \leq n_k^u \end{cases}, \quad (83)$$

Similarly,  $\mathbf{B}_j^{0p}$  becomes

$$\mathbf{B}_j^{0p} = \begin{cases} \mathbf{B}_{1j}^{0p}, & \text{if } 1 \leq j \leq n_{k-2}^p \\ \mathbf{B}_{2j}^{0p}, & \text{if } n_{k-2}^p < j \leq n_k^p. \end{cases} \quad (84)$$

**Remark 6** A *prima-facie* notion might be that additional error is introduced through using  $\mathcal{H}^1$  projectors here. However, it is proved in [41, 47] that this is not the case. In fact, it is shown that one can replace  $\mathbf{u}_h$  and  $\mathbf{p}_h$  here with enhanced stand-in functions  $\mathbf{z}_h \in \mathcal{Z}_h^u(\mathcal{K})$  and  $z_h \in \mathcal{Z}_h^p(\mathcal{K})$  where

$$\mathcal{Z}_h^u(\mathcal{K}) = \{\mathbf{z}_h \in [\mathcal{V}_h^{\mathcal{K}}(\mathcal{K})]^2, \quad a_{\mathcal{K}}^0(\mathbf{z}_h - \Pi^{\nabla u} \mathbf{z}_h, \mathbf{m}_j)_{\tilde{\rho}} = 0, \\ n_{k-2}^u < j \leq n_k^u\} \quad (85a)$$

$$\mathcal{Z}_h^p(\mathcal{K}) = \{z_h \in \mathcal{V}_h^{\mathcal{K}}(\mathcal{K}), \quad b_{\mathcal{K}}^0(z_h - \Pi^{\nabla p} z_h, m_j)_{\frac{1}{\tilde{K}_{eq}}} = 0, \\ n_{k-2}^p < j \leq n_k^p\}. \quad (85b)$$

With the additional condition requiring the orthogonality of the  $\mathcal{H}^1$  projection error with respect to the  $\mathcal{L}^2$  bilinear operators, it is seen that no additional error is introduced through this procedure.

Using the definitions for VEM DoFs in Table 4,  $\mathbf{B}_{1j}^{0u}$  and  $\mathbf{B}_{1j}^{0p}$  can be evaluated as follows:

$$\mathbf{B}_{1j}^{0u} = |\mathcal{K}| \tilde{\rho} \text{dof}(\mathbf{u}_h) = |\mathcal{K}| \mathbf{d}_j^{0u}, \quad (86a)$$

$$\mathbf{B}_{1j}^{0p} = |\mathcal{K}| \frac{1}{\tilde{K}_{eq}} \text{dof}(\mathbf{p}_h) = |\mathcal{K}| \mathbf{d}_j^{0p}, \quad (86b)$$

where

$$\mathbf{d}_j^{0u} = \tilde{\rho} \left[ \underbrace{0 \cdots 0}_{N_B^u} | \underbrace{0 \cdots 1}_{j} \cdots 0 \right], \quad (87a)$$

$$\mathbf{d}_j^{0p} = \frac{1}{\tilde{K}_{eq}} \left[ \underbrace{0 \cdots 0}_{N_B^p} | \underbrace{0 \cdots 1}_{j} \cdots 0 \right]. \quad (87b)$$

Using the monomial expansion for  $\Pi_k^{\nabla u} \mathbf{u}_h$  and  $\Pi_k^{\nabla p} \mathbf{p}_h$  from Eqs. (58a) and (58b) with running index  $\beta$  instead of  $i$  to avoid confusion, the terms  $\mathbf{B}_{2j}^{0u}$  and  $\mathbf{B}_{2j}^{0p}$  are now collected and computed:

$$\mathbf{B}_2^{0u} = \underbrace{\mathbf{H}_u}_{(n_k^u-2 \times n_k^u-2)} \zeta^{\nabla u}, \quad (88a)$$

$$\mathbf{B}_2^{0p} = \underbrace{\mathbf{H}_p}_{(n_k^p-1 \times n_k^p-1)} \zeta^{\nabla p}, \quad (88b)$$

where

$$\mathbf{H}_{\beta j}^u = \int_{\mathcal{K}} (\mathbf{m}_{\beta+2})^T \tilde{\rho} \mathbf{m}_j d\mathcal{K}, \quad \beta = 1, \dots, n_k^u - 2, \quad (89)$$

and

$$\mathbf{H}_{\beta j}^p = \int_{\mathcal{K}} (\mathbf{m}_{\beta+1})^T \frac{1}{\tilde{K}_{eq}} \mathbf{m}_j d\mathcal{K}, \quad \beta = 1, \dots, n_k^p - 1. \quad (90)$$

The coefficient arrays  $\zeta^{\nabla u}$  and  $\zeta^{\nabla p}$  have already been derived. The quantities  $\mathbf{H}_{\beta j}^u$  and  $\mathbf{H}_{\beta j}^p$  can be computed using numerical integration over sub-triangulated domains.

Using Eqs. (86a) and (88a),  $\mathbf{B}^{0u}$  is cast in the following form:

$$\mathbf{B}^{0u} = [\mathbf{B}_1^{0u} \mid \mathbf{B}_2^{0u}]^T \quad (91)$$

Similarly, using Eqs. (86b) and (88b),  $\mathbf{B}^{0p}$  is eventually expressed as

$$\mathbf{B}^{0p} = [\mathbf{B}_1^{0p} \mid \mathbf{B}_2^{0p}]^T \quad (92)$$

All terms in Eqs. (80a)-(80b) are now rendered computable.

Solving Eqs. (80a)-(80b) for the expansion coefficients and substituting in Eqs. (59) and Eqs. (60), the following approximations for the projection operators are eventually derived, i.e,

$$\Pi_k^{0u} \mathbf{u}_h = \mathbf{m}^{0u} [\mathbf{G}^{0u}]^{-1} \mathbf{B}^{0u}, \quad (93a)$$

$$\Pi_k^{0p} p_h = \mathbf{m}^{0p} [\mathbf{G}^{0p}]^{-1} \mathbf{B}^{0p}. \quad (93b)$$

## 4 Discretized governing equations

### 4.1 Consistency terms

Using Eqs. (26a) and (26b), the solid phase polynomial terms in Eq. (35) and Eq. (36) give rise to an elastic consistency term,

$$a_{\mathcal{K}}^{\varepsilon}(\mathbf{u}_h, \delta \mathbf{u}_h) = \int_{\mathcal{K}} \boldsymbol{\sigma}_s \left( \Pi_k^{\varepsilon} \mathbf{u}_h \right) : \boldsymbol{\varepsilon}_s \left( \Pi_k^{\varepsilon} \delta \mathbf{u}_h \right) d\mathcal{K}, \quad (94)$$

and a mass consistency term

$$a_{\mathcal{K}}^0(\mathbf{u}_h, \delta \mathbf{u}_h)_{\tilde{\rho}} = \int_{\mathcal{K}} \tilde{\rho} \Pi_k^{0u} \mathbf{u}_h \cdot \Pi_k^{0u} \delta \mathbf{u}_h d\mathcal{K}, \quad (95)$$

respectively. Similarly, substituting Eqs. (26c), (26d), and (26f) in the polynomial terms of Eqs. (42), (43), and (49), respectively results in the following expressions for the fluid kinetic consistency term

$$b^{\nabla}(p, \delta p_h)_{\frac{1}{\tilde{\rho}_{\text{eq}}}} = \int_{\mathcal{K}} \frac{1}{\tilde{\rho}_{\text{eq}}} \nabla \left( \Pi_k^{\nabla p} p_h \right) \cdot \nabla \left( \Pi_k^{\nabla p} \delta p_h \right) d\mathcal{K}, \quad (96)$$

the fluid compressibility consistency term.

$$b^0(p, \delta p_h)_{\frac{1}{\tilde{K}_{\text{eq}}}} = \int_{\mathcal{K}} \frac{1}{\tilde{K}_{\text{eq}}} \Pi_k^{0p} p_h \cdot \Pi_k^{0p} \delta p_h d\mathcal{K}, \quad (97)$$

and the coupling consistency term

$$a^{\nabla,0}(p_h, \delta \mathbf{u}_h)_{\tilde{\gamma}} = \int_{\mathcal{K}} \tilde{\gamma} \nabla \left( \Pi_k^{\nabla p} p_h \right) \cdot \Pi_k^{0u} \delta \mathbf{u}_h d\mathcal{K}, \quad (98)$$

respectively.

Substituting the projector approximation from Eq. (78) in Eq. (94) and performing the necessary algebraic manipulations, the following expression is eventually retrieved for the elastic stiffness consistency term

$$\tilde{\mathbf{K}}_{\mathcal{K}}^C = \boldsymbol{\zeta}^{\varepsilon T} [\mathbf{G}^{\varepsilon}] \boldsymbol{\zeta}^{\varepsilon}, \quad (99)$$

where  $\mathbf{G}^{\varepsilon}$  is provided in Eq. (62).

Similarly, substituting the projector approximation of Eq. (93a) into Eq. (95) the following expression for the mass consistency term is retrieved

$$\tilde{\mathbf{M}}_{\mathcal{K}}^C = \boldsymbol{\zeta}^{0u T} [\mathbf{G}^{0u}] \boldsymbol{\zeta}^{0u}, \quad (100)$$

where  $\mathbf{G}^{0u}$  is provided in Eq. (81a).

The expressions for the fluid phase consistency terms are established by substituting Eqs. (79b) and (93b) into Eqs. (96) and (97), respectively. Hence, the fluid kinetic consistency term assumes the following form

$$\tilde{\mathbf{H}}_{\mathcal{K}}^C = \boldsymbol{\zeta}^{\nabla p T} [\mathbf{G}^{\nabla p}] \boldsymbol{\zeta}^{\nabla p}, \quad (101)$$

where  $\mathbf{G}^{\nabla p}$  is evaluated in Eq. (68) and the fluid compressibility term becomes

$$\tilde{\mathbf{Q}}_{\mathcal{K}}^C = \boldsymbol{\zeta}^{0p T} [\mathbf{G}^{0p}] \boldsymbol{\zeta}^{0p}, \quad (102)$$

where  $\mathbf{G}^{0p}$  is provided in Eqs. (81b).

Finally, the phase coupling consistency term in Eq. (98) assumes the following form

$$\tilde{\mathbf{C}}_{\mathcal{K}}^C = \boldsymbol{\zeta}^{\nabla p T} \underbrace{[\mathbf{G}^{\nabla p 0u}]_{(n_k^p - 1 \times n_k^u)}}_{\nabla p} \boldsymbol{\zeta}^{0u}, \quad (103)$$

where where  $\mathbf{G}^{\nabla p 0u}$  in Eq. (103) is an array with elements

$$\begin{aligned} \left( \mathbf{G}^{\nabla p 0u} \right)_{ij} &= \int_{\mathcal{K}} \tilde{\gamma} \nabla(m_{i+1}) \cdot \mathbf{m}_j d\mathcal{K}, \\ i &= 1, \dots, n_k^p - 1, \quad j = 1, \dots, n_k^u \end{aligned} \quad (104)$$

This integral can be computed in a straightforward way using the sub-triangulation approach. The consistency terms are not coercive over the complete polynomial space as the monomials from the operator kernel have been omitted.

### 4.2 Stability terms

The second part of the r.h.s. in Eqs. (35),(36), (42),(43) and (49) cures this rank-deficiency. However, as these contain non-polynomial integrands without an explicit definition over the element interior, the relevant integrals cannot be computed analytically. Further, numerical integration requires higher order quadrature rules to achieve reasonable accuracy. To alleviate this, the non-polynomial contributions are approximated by user defined bilinear forms called *Stability terms*.

**Remark 7** These terms are chosen to satisfy basic stability and coercivity properties. They are also designed to reduce to zero over polynomial subspaces as in, e.g., the boundaries of an element. This is necessary as consistency terms exactly account for the entire energy here.

These stability terms also provide additional stiffness to higher order modes, thus preventing the entry of spurious higher order hourglass modes. For this reason, the stability terms can also be interpreted as a form of hourglass control [85].

The non-polynomial integrands,  $\mathbf{u}_h$  and  $p_h$  are known only in terms of the canonical bases  $\Phi^u$  and  $\Phi^p$ , respectively. Conversely, owing to the kinematic decomposition used in Eqs. (33)-(34), polynomial projections  $\mathbf{u}_h^\pi$  and  $p_h^\pi$  are also present alongside the non-polynomial terms. These quantities are known in terms of the monomial bases  $[\mathbb{M}_k(\mathcal{K})]^2$  and  $\mathbb{M}_k(\mathcal{K})$ . To facilitate interaction between these two components, as is necessary here, one needs to express  $\mathbf{u}_h^\pi$  and  $p_h^\pi$  in terms of  $\Phi^u$  and  $\Phi^p$ . This is done by re-expressing the monomial bases in terms of the canonical bases as follows:

$$\Pi_k^\varepsilon \mathbf{u}_h = \mathbf{m}^\varepsilon \zeta^\varepsilon = [\Phi^u]^T \underbrace{\mathbf{D}^\varepsilon}_{(n_{\text{dof}}^u \times n_k^u - 3)} \zeta^\varepsilon \quad (105)$$

$$\Pi_k^{0u} \mathbf{u}_h = \mathbf{m}^{0u} \zeta^{0u} = [\Phi^u]^T \underbrace{\mathbf{D}^{0u}}_{(n_{\text{dof}}^u \times n_k^u)} \zeta^{0u} \quad (106)$$

$$\Pi_k^\nabla p_h = \mathbf{m}^\nabla p \zeta^\nabla p = [\Phi^p]^T \underbrace{\mathbf{D}^\nabla p}_{(n_{\text{dof}}^p \times n_k^p - 1)} \zeta^\nabla p \quad (107)$$

$$\Pi_k^{0p} p_h = \mathbf{m}^{0p} \zeta^{0p} = [\Phi^p]^T \underbrace{\mathbf{D}^{0p}}_{(n_{\text{dof}}^p \times n_k^p)} \zeta^{0u}, \quad (108)$$

where the matrices  $\mathbf{D}^\varepsilon$ ,  $\mathbf{D}^{0u}$ ,  $\mathbf{D}^\nabla p$  and  $\mathbf{D}^{0p}$  collect the monomials evaluated at the VEM DoFs. Explicit forms for these arrays are provided in Eq. (141) in Appendix C.

Since the projectors have so far been computed only for non-kernel monomials, it is now necessary to have similar counterparts for the kernel components. This ensures the completeness of the polynomial spaces involved and restores coercivity to the entire formulation. It is of interest to note that the  $L_2$  projectors already achieve a complete polynomial projection as the respective operator kernels are empty (see Table 12 in Appendix A). To this end, it is sufficient to define kernel-specific projectors  $\zeta_S^\varepsilon$  and  $\zeta_S^\nabla p$  along with the relevant change-of-basis transformation matrices  $\mathbf{D}_S^\varepsilon$  and  $\mathbf{D}_S^\nabla p$ . These matrices contain kernel monomials evaluated at all DoFs, similar to Eq. (141):

$$\mathbf{D}_S^\varepsilon = \begin{bmatrix} \text{dof}_1(\mathbf{m}_1) & \dots & \text{dof}_1(\mathbf{m}_3) \\ \vdots & \ddots & \vdots \\ \text{dof}_{n_{\text{dof}}^u}(\mathbf{m}_1) & \dots & \text{dof}_{n_{\text{dof}}^u}(\mathbf{m}_3) \end{bmatrix}, \quad \forall \mathbf{m} \in \mathbb{K}^\varepsilon(\mathcal{K}) \quad (109a)$$

$$\mathbf{D}_S^\nabla p = \begin{bmatrix} \text{dof}_1(\mathbf{m}_1) \\ \vdots \\ \text{dof}_{n_{\text{dof}}^p}(\mathbf{m}_1) \end{bmatrix}, \quad \forall \mathbf{m} \in \mathbb{K}^\nabla p(\mathcal{K}), \quad (109b)$$

where  $\text{dof}_i(\mathbf{m}_j)$  denotes the  $j$ th monomial evaluated at the  $i$ th DoF.

The quantities  $\zeta_S^\varepsilon$  and  $\zeta_S^\nabla p$  are now computed in a straightforward way:

$$\zeta_S^\varepsilon = [\mathbf{G}_S^\varepsilon]^{-1} \mathbf{B}_S^\varepsilon \quad (110a)$$

$$\zeta_S^\nabla p = [\mathbf{G}_S^\nabla p]^{-1} \mathbf{B}_S^\nabla p, \quad (110b)$$

where  $\mathbf{G}_S^\varepsilon = \mathbf{B}_S^\varepsilon \mathbf{D}_S^\varepsilon$  and  $\mathbf{G}_S^\nabla p = \mathbf{B}_S^\nabla p \mathbf{D}_S^\nabla p$ . The terms  $\mathbf{B}_S^\varepsilon$  and  $\mathbf{B}_S^\nabla p$  are specially defined using relations derived in [83, 47]:

$$\mathbf{B}_S^\varepsilon = \begin{bmatrix} 1/N_v & 0 & 1/N_v & 0 & \dots \\ 0 & 1/N_v & 0 & 1/N_v & \dots \\ \eta(\mathbf{x}_1) & -\xi(\mathbf{x}_1) & \eta(\mathbf{x}_2) & -\xi(\mathbf{x}_2) & \dots \end{bmatrix} \quad (111a)$$

$$\mathbf{B}_S^\nabla p = [1/N_v \ 1/N_v \ \dots], \quad (111b)$$

where  $\xi = \frac{x-x_K}{h_K}$  and  $\eta = \frac{y-y_K}{h_K}$  denote scaled monomials in each parametric direction.

**Remark 8** These relations are obtained for  $\mathbf{B}_S^\varepsilon$  by imposing equality of two mean translations and a single rotation between  $\mathbf{u}_h$  and  $\mathbf{u}_h^\pi$ . Similarly,  $\mathbf{B}_S^\nabla p$  is obtained through imposing equality of mean pore-fluid pressures between  $p_h$  and  $p_h^\pi$ . It is to be noted that since Eq. (111) is defined only at vertex DoFs, columns resulting from edge and area DoFs encountered in  $k \geq 2$  methods are set to zero.

The complete stability specific projection operators are finally expressed in the canonical bases as follows:

$$\Pi_{\text{tot}}^\varepsilon = \mathbf{D}^\varepsilon \zeta^\varepsilon + \mathbf{D}_S^\varepsilon \zeta_S^\varepsilon \quad (112a)$$

$$\Pi_{\text{tot}}^{0u} = \mathbf{D}^{0u} \zeta^{0u} \quad (112b)$$

$$\Pi_{\text{tot}}^\nabla p = \mathbf{D}^\nabla p \zeta^\nabla p + \mathbf{D}_S^\nabla p \zeta_S^\nabla p \quad (112c)$$

$$\Pi_{\text{tot}}^{0p} = \mathbf{D}^{0p} \zeta^{0p}. \quad (112d)$$

Driven by the work of [86] on elasto-statics, we introduce the following stability term approximants for the non-polynomial terms of the solid phase

$$\text{NP}(a_K^\varepsilon) \approx \mathcal{S}^K(\mathbf{u}_h, \delta \mathbf{u}_h) = [\Phi^u]^T \tilde{\mathbf{K}}_K^S [\Phi^u], \quad (113a)$$

$$\text{NP}(a_K^0) \approx \mathcal{S}^M(\mathbf{u}_h, \delta \mathbf{u}_h)_{\tilde{\rho}} = [\Phi^u]^T \tilde{\mathbf{M}}_K^S [\Phi^u], \quad (113b)$$

the fluid phase

$$\text{NP}(b_K^\nabla) \approx \mathcal{S}^H(p_h, \delta p_h)_{\frac{1}{\tilde{\rho}_{\text{eq}}}} = [\Phi^p]^T \tilde{\mathbf{H}}_K^S [\Phi^p], \quad (114a)$$

$$\text{NP}(b_K^0) \approx \mathcal{S}^Q(p_h, \delta p_h)_{\frac{1}{\tilde{\kappa}_{\text{eq}}}} = [\Phi^p]^T \tilde{\mathbf{Q}}_K^S [\Phi^p], \quad (114b)$$

and the coupling term

$$\text{NP}(a_K^{(\nabla,0)}) \approx \mathcal{S}^C(p_h, \delta \mathbf{u}_h) = [\Phi^p]^T \tilde{\mathbf{C}}_K^S [\Phi^u], \quad (115)$$

respectively.

In Eqs. (113a)-(115),  $\tilde{\mathbf{K}}_{\mathcal{K}}^S$ ,  $\tilde{\mathbf{M}}_{\mathcal{K}}^S$ ,  $\tilde{\mathbf{H}}_{\mathcal{K}}^S$ ,  $\tilde{\mathbf{Q}}_{\mathcal{K}}^S$ , and  $\tilde{\mathbf{C}}_{\mathcal{K}}^S$  denote the elastic, mass, fluid kinetic, fluid compressibility and coupling stability stiffness matrices, respectively. These are defined according to the following expressions,

$$\tilde{\mathbf{K}}_{\mathcal{K}}^S = (\mathbb{I}_u - \boldsymbol{\Pi}_{\text{tot}}^{\boldsymbol{\varepsilon}})^T \beta_K (\mathbb{I}_u - \boldsymbol{\Pi}_{\text{tot}}^{\boldsymbol{\varepsilon}}), \quad (116a)$$

$$\tilde{\mathbf{M}}_{\mathcal{K}}^S = (\mathbb{I}_u - \boldsymbol{\Pi}_{\text{tot}}^{0u})^T \beta_M (\mathbb{I}_u - \boldsymbol{\Pi}_{\text{tot}}^{0u}), \quad (116b)$$

$$\tilde{\mathbf{H}}_{\mathcal{K}}^S = (\mathbb{I}_p - \boldsymbol{\Pi}_{\text{tot}}^{\nabla p})^T \beta_H (\mathbb{I}_p - \boldsymbol{\Pi}_{\text{tot}}^{\nabla p}), \quad (116c)$$

$$\tilde{\mathbf{Q}}_{\mathcal{K}}^S = (\mathbb{I}_p - \boldsymbol{\Pi}_{\text{tot}}^{0p})^T \beta_Q (\mathbb{I}_p - \boldsymbol{\Pi}_{\text{tot}}^{0p}), \quad (116d)$$

$$\tilde{\mathbf{C}}_{\mathcal{K}}^S = (\mathbb{I}_p - \boldsymbol{\Pi}_{\text{tot}}^{\nabla p})^T \beta_C \mathbb{I}_C (\mathbb{I}_u - \boldsymbol{\Pi}_{\text{tot}}^{0u}). \quad (116e)$$

In Eqs. (116),  $\mathbb{I}_u$  and  $\mathbb{I}_p$  are identity matrices of sizes  $(n_{\text{dof}}^u \times n_{\text{dof}}^u)$  and  $(n_{\text{dof}}^p \times n_{\text{dof}}^p)$ . The array  $\mathbb{I}_C = [\mathbb{I}_p, \mathbb{I}_p]$  is used to ensure compatible matrix multiplication. The stabilization parameters  $\beta_K$ ,  $\beta_M$ ,  $\beta_H$ ,  $\beta_Q$  and  $\beta_C$  are defined using the D-recipe stabilization (originally proposed in [87] and adapted to a porous media context in [76]) below:

$$\begin{aligned} \beta_K^G &= \gamma_K^G |\mathcal{K}| \frac{\text{tr}(\mathbb{D})}{\text{tr}(\mathbf{D}^{\boldsymbol{\varepsilon}^T} \mathbf{D}^{\boldsymbol{\varepsilon}})} & \beta_M^G &= \gamma_M^G |\mathcal{K}| \frac{\tilde{\rho}}{\text{tr}(\mathbf{D}^{0u^T} \mathbf{D}^{0u})} \\ \beta_H^G &= \gamma_H^D |\mathcal{K}| \frac{1/\tilde{\rho}_{\text{eq}}}{\text{tr}(\mathbf{D}^{\nabla p^T} \mathbf{D}^{\nabla p})} & \beta_Q^G &= \gamma_Q^G |\mathcal{K}| \frac{1/\tilde{K}_{\text{eq}}}{\text{tr}(\mathbf{D}^{0p^T} \mathbf{D}^{0p})} \\ \beta_C^G &= \gamma_C^G |\mathcal{K}| \frac{\tilde{\gamma}}{\text{tr}(\mathbf{D}^{0p^T} \mathbf{D}^{0p})}. \end{aligned} \quad (117)$$

In Eq. (117), the constants  $\gamma_K^G$ ,  $\gamma_M^G$ ,  $\gamma_H^G$ ,  $\gamma_Q^G$ ,  $\gamma_C^G$  are scaling parameters. In the numerical tests conducted in this work, we observe that  $\gamma_K^G = \gamma_M^G = \gamma_H^G = \gamma_Q^G = \gamma_C^G = 1$  provides accurate and well behaved results in all cases. However, it has been reported in [68], that the stabilization parameter for the elastic stiffness matrix, while stable with regards to uniform/isotropic scaling, is unstable with respect to the aspect ratio of the element. Such unstable ratios can often be encountered, e.g., in the case of non-conforming interfaces. To remedy this, an alternate choice for the elastic stiffness stabilization parameter is proposed in [68]:

$$\beta_K^N = \gamma_K^N |\mathcal{K}| \text{tr}(\mathbb{D}) \text{tr}([\mathbf{D}^{\boldsymbol{\varepsilon}^T} \mathbf{D}^{\boldsymbol{\varepsilon}}]^{-1}). \quad (118)$$

The choice  $\gamma_K^N = \frac{1}{9}$  has been proposed in [68]. For a more detailed study on the influence of mesh quality on the VEM, the reader is referred to [88].

### 4.3 State matrices

Employing the consistency and stability term definitions introduced in Eqs. (99)-(103) and Eqs. (116), re-

spectively, the virtual element state matrices are eventually defined according to the following expressions, i.e.,

$$\begin{array}{lll} & \text{Consistency} & \text{Stability} \\ \tilde{\mathbf{K}}_{\mathcal{K}} & \approx & \tilde{\mathbf{K}}_{\mathcal{K}}^C + \tilde{\mathbf{K}}_{\mathcal{K}}^S \\ \tilde{\mathbf{M}}_{\mathcal{K}} & \approx & \tilde{\mathbf{M}}_{\mathcal{K}}^C + \tilde{\mathbf{M}}_{\mathcal{K}}^S \\ \tilde{\mathbf{H}}_{\mathcal{K}} & \approx & \tilde{\mathbf{H}}_{\mathcal{K}}^C + \tilde{\mathbf{H}}_{\mathcal{K}}^S \\ \tilde{\mathbf{Q}}_{\mathcal{K}} & \approx & \tilde{\mathbf{Q}}_{\mathcal{K}}^C + \tilde{\mathbf{Q}}_{\mathcal{K}}^S, \\ \tilde{\mathbf{C}}_{\mathcal{K}} & \approx & \tilde{\mathbf{C}}_{\mathcal{K}}^C + \tilde{\mathbf{C}}_{\mathcal{K}}^S. \end{array} \quad (119)$$

The local state matrices defined in Eq. (119) are assembled over the entire domain  $\Omega_h$  using a direct approach to obtain the following global state matrices:

$$\begin{aligned} \tilde{\mathbf{K}} &= \sum_{i=1}^{n_{\text{el}}} \tilde{\mathbf{K}}_{\mathcal{K}_i}, & \mathbf{M} &= \sum_{i=1}^{n_{\text{el}}} \tilde{\mathbf{M}}_{\mathcal{K}_i}, & \tilde{\mathbf{H}} &= \sum_{i=1}^{n_{\text{el}}} \tilde{\mathbf{H}}_{\mathcal{K}_i}, \\ \tilde{\mathbf{Q}} &= \sum_{i=1}^{n_{\text{el}}} \tilde{\mathbf{Q}}_{\mathcal{K}_i}, & \tilde{\mathbf{C}} &= \sum_{i=1}^{n_{\text{el}}} \tilde{\mathbf{C}}_{\mathcal{K}_i}. \end{aligned} \quad (120)$$

### 4.4 Computing Boundary and Interface integrals

It is to be noted that as stated in Remark 3, one recovers from the VEM, a classical Lagrange polynomial based interpolation over the element boundaries. As a result, the boundary terms mentioned in Eqs. (26e) and (26g) can be computed in a straightforward way without resorting to deriving projectors exclusive to these forms:

$$\tilde{\mathbf{A}}_{\mathcal{K}} = \int_{\Gamma_{hr}^{\mathcal{K}}} \frac{1}{z(\theta)} \boldsymbol{\Phi}^p \cdot \boldsymbol{\Phi}^p \, d\Gamma, \quad (121a)$$

$$\tilde{\mathbf{S}}_{\mathcal{K}} = \int_{\Gamma_{ht}^{\mathcal{K}}} c(\boldsymbol{\Phi}^p \cdot \mathbf{n}) \cdot \boldsymbol{\Phi}^u \, d\Gamma, \quad (121b)$$

where  $\tilde{\mathbf{A}}_{\mathcal{K}}$  denotes a local admittance matrix encountered over Robin boundary  $\Gamma_{hr}^{\mathcal{K}}$  (see Eq. (26e)). Matrix  $\tilde{\mathbf{S}}_{\mathcal{K}}$  denotes a local fluid-structure coupling matrix encountered at an interface (see Eq. (26g)). Similar to Eq. (120), these integrals are assembled over the relevant boundaries  $\Gamma_{hr}$ ,  $\Gamma_{ht}$ ,  $\Gamma_{hq}$  to yield global boundary matrices:

$$\tilde{\mathbf{A}} = \sum_i \tilde{\mathbf{A}}_{\mathcal{K}(i)}, \quad \tilde{\mathbf{S}} = \sum_i \tilde{\mathbf{S}}_{\mathcal{K}(i)}. \quad (122)$$

## 5 Analysis Procedure

The virtual element discretization of the weak form in Eq. (16) is written as a coupled system of linear equations in matrix form:

$$\begin{bmatrix} \tilde{\mathbf{K}} - \omega^2 \tilde{\mathbf{M}} & -(\tilde{\mathbf{C}} + \tilde{\mathbf{S}}) \\ -\omega^2 (\tilde{\mathbf{C}}^T + \tilde{\mathbf{S}}^T) \tilde{\mathbf{H}} + j\omega \tilde{\mathbf{A}} - \omega^2 \tilde{\mathbf{Q}} \end{bmatrix} \begin{Bmatrix} \hat{\mathbf{u}} \\ \hat{\mathbf{p}} \end{Bmatrix} = \begin{Bmatrix} \mathbf{f}^u \\ \mathbf{f}^p \end{Bmatrix}, \quad (123)$$

where  $\mathbf{f}^u$  and  $\mathbf{f}^p$  are load terms for either phase. It has already been shown in Section 2.2 that all coupling and support conditions yield either zero-value boundary integrals or forms that are bilinear in nature, (see Tables 2-3). Furthermore, since we exclusively consider acoustic excitations for this work, it is reasonable to allow  $\mathbf{f}^u = \mathbf{0}$  and  $\mathbf{f}^p = \mathbf{0}$ . These excitations are imposed as Dirichlet pressures.

It is worth noting that despite Eq. (123) being linear in  $\hat{\mathbf{u}}$  and  $\hat{\mathbf{p}}$ , it exhibits an explicit parametric non-linearity with respect to  $\omega$ . Implicit material non-linearities are encountered in the global state matrices through their complex frequency-dependent material parameters, see, e.g, Eqs. (6) for the JCAL model.

Owing to the spectral nature of the problem, multiple solutions to Eq. (123) are required over a desired frequency bandwidth to sufficiently characterize the vibro-acoustic behaviour of the system. It is possible to significantly reduce the assembly time by assembling the global state matrices only once without the implicit frequency-dependent content; this can be post-multiplied during the solution stage.

## 6 Numerical Examples

In this work, we investigate the accuracy of the VEM through four numerical examples. A first order method  $k = 1$  is used. The accuracy of the displacements and pressures achieved by the method is measured through relative  $\mathcal{L}_2$  error norms:

$$\|\mathbf{u}_h^Q(\omega) - \mathbf{u}_{ref}^Q(\omega)\|_{\mathcal{L}_2} = \sqrt{\frac{1}{n_{Q_{el}}} \sum_{i=1}^{n_{Q_{el}}} \frac{\langle \mathbf{u}_{h(i)}^Q(\omega) - \mathbf{u}_{ref(i)}^Q(\omega), \mathbf{u}_{h(i)}^Q(\omega) - \mathbf{u}_{ref(i)}^Q(\omega) \rangle}{\langle \mathbf{u}_{ref(i)}^Q(\omega), \mathbf{u}_{ref(i)}^Q(\omega) \rangle}}, \quad (124)$$

$$\|\mathbf{p}_h^Q(\omega) - \mathbf{p}_{ref}^Q(\omega)\|_{\mathcal{L}_2} = \sqrt{\frac{1}{n_{Q_{el}}} \sum_{i=1}^{n_{Q_{el}}} \frac{\langle \mathbf{p}_{h(i)}^Q(\omega) - \mathbf{p}_{ref(i)}^Q(\omega), \mathbf{p}_{h(i)}^Q(\omega) - \mathbf{p}_{ref(i)}^Q(\omega) \rangle}{\langle \mathbf{p}_{ref(i)}^Q(\omega), \mathbf{p}_{ref(i)}^Q(\omega) \rangle}}$$

where  $\mathbf{u}_h^Q(\omega)$ ,  $\mathbf{p}_h^Q(\omega)$ , where  $\mathbf{u}_{ref}^Q(\omega)$ ,  $\mathbf{p}_{ref}^Q(\omega)$  denote numerically computed and reference displacements and pressures at an excitation frequency  $\omega$ , respectively. The quantities are interpolated over a query mesh  $Q$  with  $n_{Q_{el}}$  elements. The reference solutions  $\mathbf{u}_{ref}^Q$  and  $\mathbf{p}_{ref}^Q$  are obtained using finely discretized FEM solutions. The stabilization scaling parameters used throughout the examples correspond to Eq. (117), unless explicitly stated otherwise.

Useful acoustic indicators like the Sound Absorption Coefficient (SAC) and the Sound Transmission Loss Coefficient (STL) are provided. For comparisons, a reference SAC or STL curve is generated with the finely discretized post-processed FEM results or the semi-analytical Transfer Matrix Method (TMM) [89]. The procedure followed in computing these indicators is provided in Appendix D.

### 6.1 Square poroelastic domain

The convergence behaviour of the method is investigated herein. A square poroelastic domain with a side  $b = 57$  mm is considered. This domain is given impedance tube constraints, i.e. a roller support on the lateral sides and a rigid impervious backing at the rear. It is excited by an acoustic plane wave at normal incidence. This configuration is illustrated in Fig. 6.

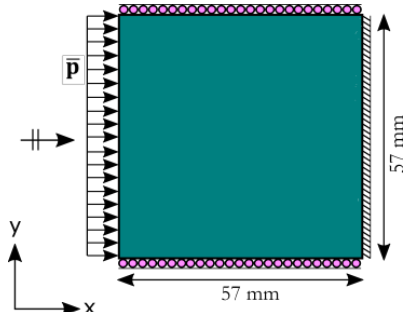


**Fig. 6** A poro-elastic domain in impedance tube configuration subject to plane-wave acoustical excitation  $\bar{p}$  at normal incidence

The material used is a poroelastic melamine foam. The macroscopic material parameters are provided as Material ID III in Table 7. Since the governing equations are linear in pressures, the solutions can be appropriately scaled with the excitation. For the sake of brevity, an amplitude of 1 Pa is considered.

The VEM solution procedure is performed using a structured quadrilateral grid (QUAD) and unstructured CVT grid (CVT) over an excitation frequency

range  $f \in [20\text{Hz}, 5500\text{Hz}]$ . Results were found to converge at a discretization of  $10 \times 10$  QUAD elements and 100 polygonal CVT elements. The converged displacement contours  $\|\mathbf{u}\|$  for both meshes are shown in Fig. 7 at 20 Hz and 1500 Hz. Similarly, the converged pressure contours  $p$  are provided in Fig. 8 for the same frequencies.

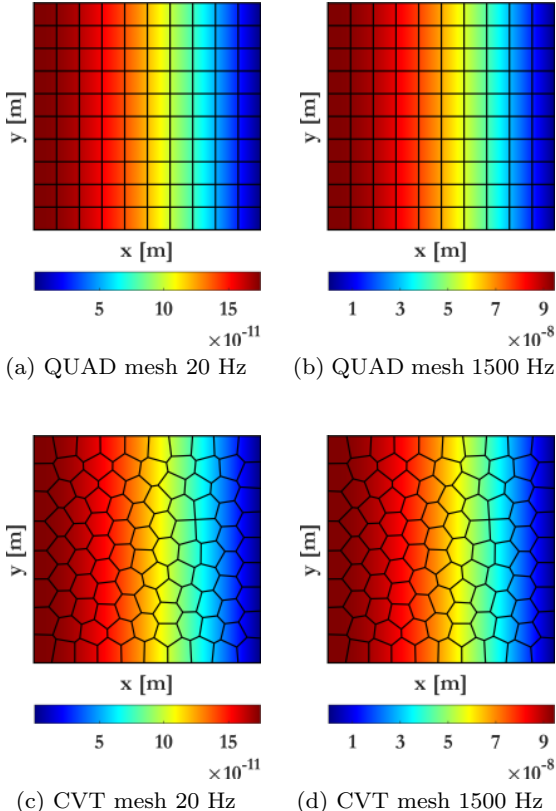


**Fig. 7** Converged  $\|\mathbf{u}\|$  displacement contours at excitation frequencies 20 Hz and 1500 Hz for QUAD and CVT type meshes

The contours obtained by the VEM for both meshes are practically identical with a linear variation in displacements and a uniform pressure profile accross the domain being retrieved. As anticipated, the method converges to a solution that is independent of the type of the underlying discretization.

Next, a convergence study is performed through an a posteriori error-based mesh sensitivity analysis. Five QUAD and five CVT meshes are chosen for this purpose. The details of these discretizations are provided in Table 5. A finely discretized FEM solution with a structured  $250 \times 250$  QUAD mesh is used as a reference.

The relative displacement errors in  $\mathcal{L}_2$  norm for both mesh types are shown at frequencies  $f = 20\text{Hz}$ ,  $f = 750$

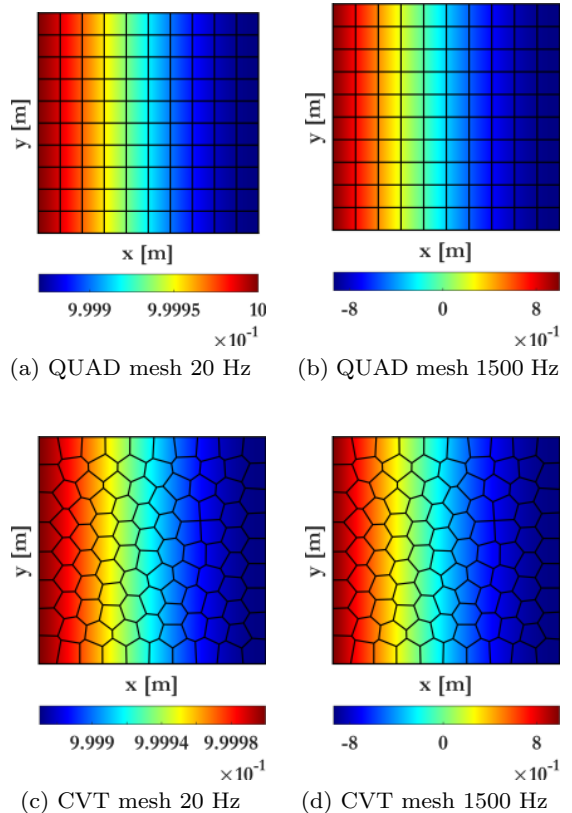


**Fig. 8** Converged  $p$  pressure contours at excitation frequencies 20 Hz and 1500 Hz for QUAD and CVT type meshes

Label	QUAD		CVT	
	Nodes	Elements	Nodes	Elements
I	36	$5 \times 5$	52	25
II	121	$10 \times 10$	202	100
III	676	$25 \times 25$	1251	625
IV	2601	$50 \times 50$	4993	2500
V	10,201	$100 \times 100$	19,968	10,000

**Table 5** Discretization used for the error-based mesh sensitivity analysis

Hz and  $f = 1500\text{Hz}$  in Fig. 9. Variations with respect to the number of degrees of freedom and the average element size are shown on the bottom and top horizontal axes, respectively. Near comparable behaviour is obtained by both meshes. The CVT mesh is shown to achieve smaller errors at higher discretizations than the QUAD mesh. This is expected as the number of nodes and hence degrees of freedom associated with the former practically doubles as shown in Table 5 hence resulting in considerably more flexible numerical domains.

The relative pressure errors in  $\mathcal{L}_2$  norm are displayed in Fig. 10. Once again comparable behaviour is noticed across both meshes. The displacement and

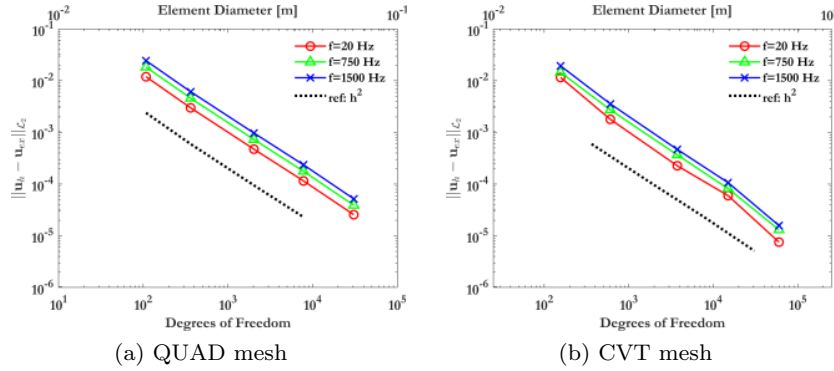


**Fig. 9** Convergence of relative errors in displacements at excitation frequencies 20 Hz, 750 Hz and 1500 Hz

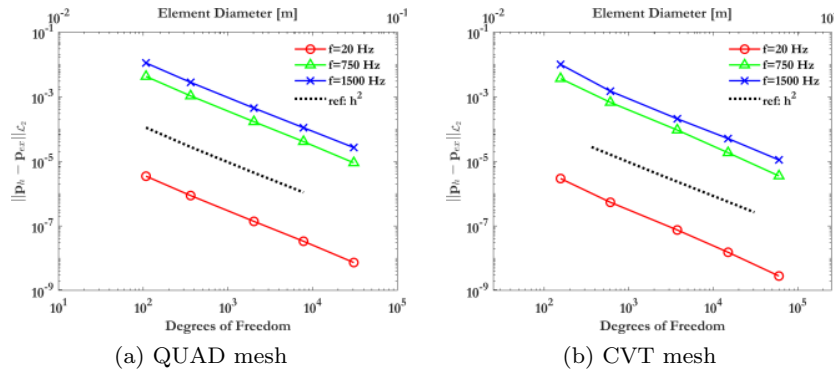


**Fig. 10** Convergence of relative errors in pressures at excitation frequencies 20 Hz, 750 Hz and 1500 Hz

pressure fields are approximated in descending accuracy across the excitation frequency spectrum in Figs. 9 and 10. This is due to the fact that the same spatial resolution is employed across the entire frequency range; yet the higher the frequency becomes the finer mesh discretization is required to accurately resolve the corresponding wave lengths.

First order methods of this nature are expected a priori to converge at  $h^2$  with respect to mesh size in the  $\mathcal{L}_2$  norm. This theoretical slope is provided as "ref:  $h^2$ " in Figs. 9 and 10. Graphically it can be seen that near optimal convergence rates for errors in displacements and pressures are obtained by the method across both mesh-types. This suggests that the stability approximations chosen using the D-recipe stabilization procedure, and the enhancing conditions introduced in computing  $\mathcal{L}_2$  projectors do not generate sub-optimal convergence properties.

It is of interest to note that a larger spread is observed for errors in pressure in Fig. 10 when compared to errors in displacements in Fig. 9. This potentially highlights the requirement for a different order of approximation specifically for the pressure field. Such aspects are beyond the scope of this work.

### 6.1.1 A remark on VEM mesh refinement

To achieve accurate high frequency solutions, several alternatives to standard  $h$ -refinement have been proposed in the literature;  $p$  refinement or  $h-p$  refinement strategies using classical polynomial-driven finite elements do offer a viable route. Alternatives based on enrichment strategies such as generalized finite element methods [90], discontinuity enriched methods [91]. Amongst these, the Spectral Element Method (SEM) [92] has been shown to provide well behaved solutions across the frequency spectrum. These higher order methods are motivated by the creation of more flexible domains without having to decrease element sizes. This criterion can be met using the Virtual Element Method as well.

To examine this, a relatively coarse discretization of  $4 \times 4$  QUAD elements is shown in Fig. 11a. 1, 2 and 3 nodes are inserted per element edge to obtain the 8, 12, and 16 noded element discretizations shown in Figs. 11b, 11c, and 11d, respectively. These elements are parametrized using  $p_e$ , which corresponds to the number of subdivisions per edge.

In classical finite element methods, Figs. 11b, 11c and 11d are generally interpreted as serendipity elements and support quadratic, cubic and quartic inter-

subdivisions per edge	nodes per element	total nodes	FEM		VEM	
			edges	order	edges	order
$p_e = 1$	4	25	4	1	4	1
$p_e = 2$	8	65	4	2	8	1
$p_e = 3$	12	105	4	3	12	1
$p_e = 4$	16	145	4	4	16	1

**Table 6** Alternate parametrization of higher order elements using a first order VEM.

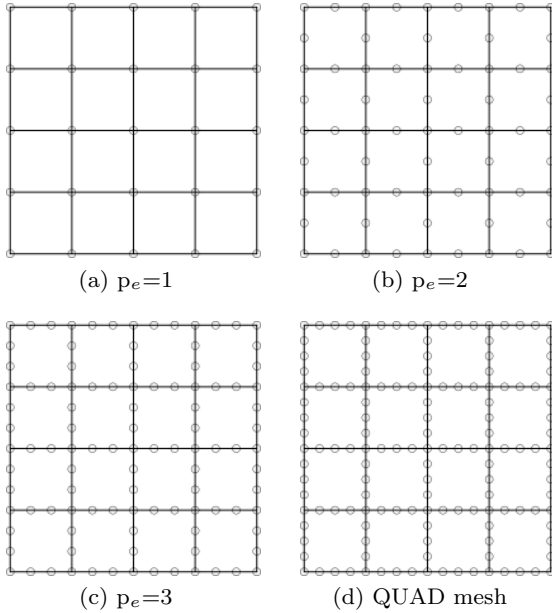


**Fig. 11**  $p_e$  refined virtual element meshes

polations, respectively and  $p_e$  would correspond to the order of approximation. While these higher order interpolations are certainly achievable through the VEM, we propose an alternate route harnessing the ability of a virtual element to have multiple edges. A first order VEM ( $k=1$ ) interprets  $p_e=1$ ,  $p_e=2$ ,  $p_e=3$  and  $p_e=4$  as 4-sided, 8-sided, 12-sided and 16-sided elements, respectively. Hence, linear polynomials living on each edge can uniquely be defined through adjacent vertex degrees of freedom. This argument is summarized in Table 6.

Since the elements employed remain linear, an h-refinement based error convergence analysis would continue to yield a relative error convergence rate of  $h^2$  in  $\mathcal{L}^2$  norm. One should not expect the  $h^{p_e+1}$  rates more commonly associated with higher order methods.

**Remark 9** It is to be noted that the number of quadrature points required for accurate polynomial integration directly scales with the order of the classical polynomial based higher order methods, such as FEM and SEM. Conversely, on the edge refinement method examined herein, the number of quadrature points will vary only

as a function of the sub-triangulation required for integration over the domain interior. We point out that for first order VEM methods, this sub-triangulation is required only for bilinear operators containing  $\mathcal{L}_2$ -type projectors, i.e.,  $a_K^0, b_K^0$  and  $a_K^{(\nabla,0)}$ . For the purely  $\mathcal{H}_1$ -type operators, i.e.  $a_K^\varepsilon$  and  $b_K^\nabla$ , numerical integration is moved to the boundary and exactly and uniquely computed through 2 Gauss Lobatto quadrature points per edge, located at the relevant vertex nodes.

The influence of this procedure on the solution accuracy is illustrated through the SAC. This determines the absorption behaviour of a system and is computed in post-processing (see Appendix D).

The reference SAC is computed through the semi-analytic Transfer Matrix Method (TMM). Although the TMM assumes an infinite lateral dimension, the solution is still valid for the purpose of this example due to the normal plane wave incidence and lateral sliding condition.

The SAC curves computed for the four discretizations described above are compared against the TMM curve in Fig. 12. The SAC computed through the VEM agrees with the TMM curve from 20 Hz to  $\approx 1500$  Hz. Beyond this limit, deviations are noticed, especially for the  $p_e=1$  mesh. On the contrary, a near exact correspondence is achieved with  $p_e=4$ .

To illustrate gains in computational cost, a second-order serendipity finite element method is used to perform the computations over the  $p_e=2$  mesh. Total computational times are recorded over 1000 runs to obtain meaningful comparisons. The VEM achieves a time of 0.42 hours, whereas the FEM takes a total time of 0.6 hours. Hence, the order 1 virtual element method achieves in providing accurate results without significantly increasing the computational complexity of the discretized domain.

## 6.2 Multilayer systems

Poro-elastic materials generally exhibit reduced sound absorption properties at low excitation frequencies. This is due to a mismatch between the sample thickness

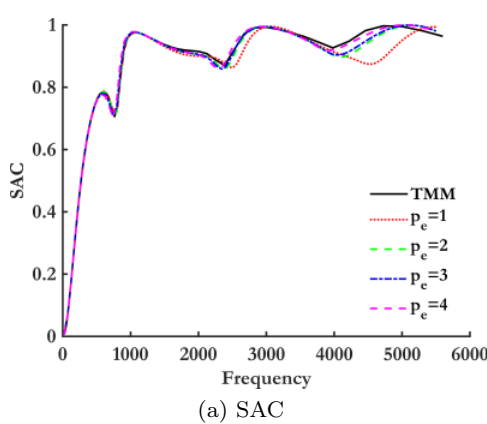


**Fig. 12** Convergence of SAC with  $p_e$  refinement

and large wavelengths encountered at these frequencies. Multilayer systems are often deployed to improve the low frequency behaviour. Similarly, multilayer configurations are also designed to improve sound transmission properties as well.

This example is chosen to demonstrate the ability of the VEM to account for wave propagation through different types of materials. Varied interface coupling constraints, boundary conditions and acoustic excitation types are considered. A multilayer system comprising three layers, i.e., (I) a melamine foam (poroelastic), (II) an elastic plasterboard (solid) and (III) non-dissipative air (fluid) is taken up for analysis. Each layer is 10 mm thick and has a lateral dimension of 2m. This exaggerated height is used to simulate the infinite diameter assumption used by the Transfer Matrix Method for impedance tube simulations. Contrary to the previous example, here this requirement is necessary owing to the presence of oblique excitations. To avoid spurious reflections at the lateral boundaries due to the fully reflecting zero normal fluid velocity Neumann conditions, Floquet-Bloch type conditions [93] are typically employed to mimic periodic material behaviour in the vertical direction. Alternatively, absorbing/non-reflecting boundaries are also implemented using Infinite Elements [94], Perfectly Matched Layers [95] or doubly asymptotic approximations [96]. Since these possibilities lie outside the scope of our work, we instead choose to model an exaggerated height of 2m to eliminate the possibility of spurious reflections at these lateral boundaries.

The material properties for each layer is summarized in Table 7.

**Remark 10** We mention that creating multilayer configurations that improve acoustic properties is a matter of engineering judgement and is not our objective here. Our choice of materials for the multilayered system is

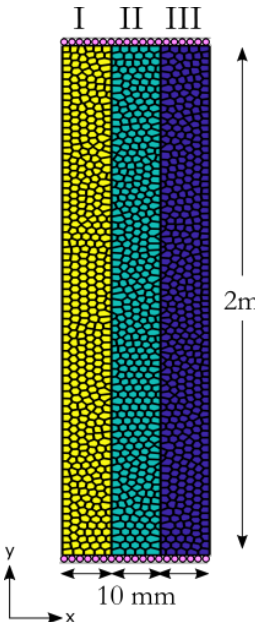


**Fig. 13** Multilayer configuration with roller supports on lateral edges. Material configuration provided in Table 7. Each layer is 10 mm thick. Plane wave normal incidence excitation with a fully clamped backing considered for Section 6.2.1. Diffuse field excitation with anechoic termination considered for Section 6.2.2.

motivated purely by computational reasons. Layer II is chosen as a solid elastic layer to demonstrate the ability of the VEM to accurately compute the admittance matrix necessary for coupling pressure degrees of freedom of layer I and layer III with the displacement degrees of freedom of layer II at the respective interfaces. This corresponds to  $a^{0\Gamma}(p_h, \delta\mathbf{u}_h)_c$  defined in Eq. (23g) and Table 3.

The lateral edges are subjected to sliding conditions with roller supports. A polygonal discretization of 30 CVT elements per smallest wavelength is considered to accurately resolve high frequency wave propagation. The smallest wavelength is chosen to be the minimum wavelength of the three Biot waves (P1, P2, S) propagating through a poroelastic media, and the corresponding structural and acoustic waves propagating through elastic and fluid media [97]. The interfaces are appropriately seeded to allow the CVT to accurately capture the geometry. The ability of the VEM to account for potentially non-conforming interfaces is illustrated in Fig. 14.

These non-conforming interfaces are converted into conforming ones by exploiting the power of the VEM to accommodate elements with several edges. Nodes that are conventionally treated as "hanging nodes" are detected and added to the relevant interface element to create new corners and edges; it is not necessary to

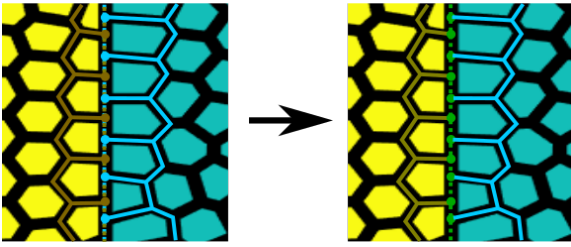


**Fig. 14** Converting a non-conforming interface into a conforming one by adding nodes and edges to each interface element as required

incorporate weak coupling techniques like the Mortar method [98] or the Nitsche method [99] here.

The node-insertion technique may result in elements with non-standard aspect ratios, thereby leading to an unstable aspect ratio as discussed in Section 4.2. In this case, the elements may not be amenable to standard isotropic scaling of the elastic stiffness stability terms. To examine this, the alternate elastic stabilization parameter of Eq. (118) is also used herein and the stability of the results is examined. A heat map illustrating "diff", i.e., the relative differences between the element-wise elastic stiffness matrix as computed using Eqs. (117) and (118) is provided in Fig. 15. The relative

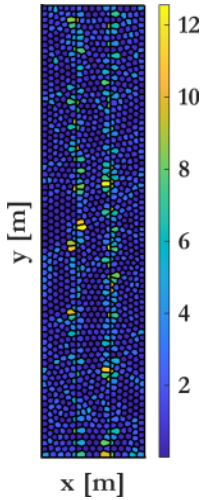


**Fig. 15** Relative differences (in %) in the element-wise elastic stiffness matrix with respect to different stabilization parameter choices (Eqs. (117) and (118))

difference is evaluated for the  $i^{th}$  element as

$$\text{diff}_i = \left\| \frac{\tilde{\mathbf{K}}_{\mathcal{K}(i)}^G - \tilde{\mathbf{K}}_{\mathcal{K}(i)}^N}{\tilde{\mathbf{K}}_{\mathcal{K}(i)}^G} \right\|, \quad (126)$$

where  $\tilde{\mathbf{K}}_{\mathcal{K}(i)}^G$  and  $\tilde{\mathbf{K}}_{\mathcal{K}(i)}^N$  indicate the element elastic stiffness matrix as computed using the VEM, with stabilization parameters  $\beta_K^G$  and  $\beta_K^N$ , respectively (see Eqs. (117)

and (118)). The differences are observed to be mostly negligible except from the interface elements where node insertion has taken place. The behaviour of the method for two problems is examined: (1) an absorption problem subject to plane wave excitation and (2) a transmission problem subject to diffuse field excitation.

### 6.2.1 Normal incidence plane wave excitation absorption problem

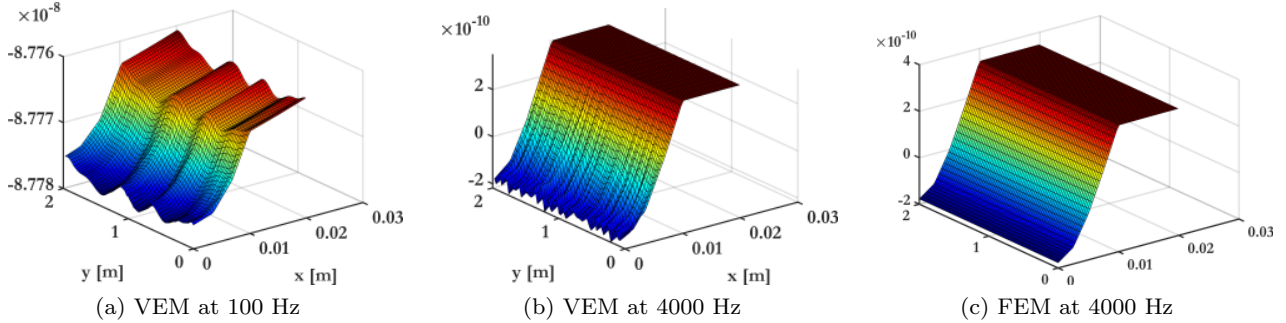
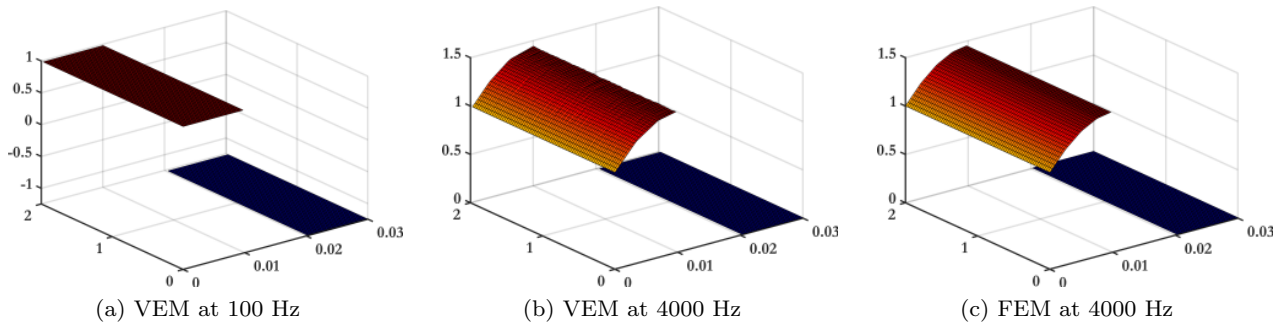
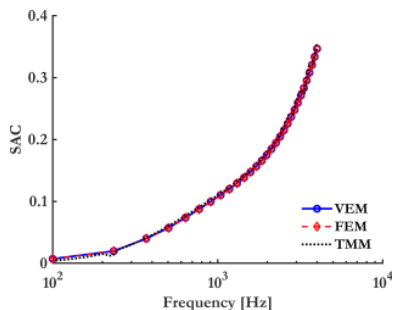
A plane acoustic wave at normal incidence excites the left face of layer I. The right face of layer III is subject to a rigid backing, i.e., bonded/clamped supports. The response of the system to an excitation frequency spectra of  $f = [100, 4000]$  Hz is evaluated. The displacement and pressure contours  $u_x$ ,  $u_y$  and  $p$  obtained by the VEM at low and high excitation frequencies 100 Hz and 4000 Hz are shown in Figs. 16 and 17, respectively. The corresponding contours obtained by the FEM at 4000 Hz is also shown for comparison. All contours are interpolated over a structured query rectangular grid containing  $50 \times 50$  QUAD elements to make the comparisons fair.

As expected in this normal incidence case, the elastic wave is propagating along the x-direction as shown in Fig. 16. The high frequency contours obtained by the VEM and FEM are practically identical. It is evident from Figs. 16 that the elastic wave does not propagate through the fluid/air layer. The acoustic wave in Fig. 17 propagates only through the poroelastic and fluid layers and is fully horizontal. Once again, the high frequency FEM and VEM contours are practically equivalent, and the pressure wave has nearly been damped out in the fluid layer.

The SAC is evaluated by the FEM and the VEM for 30 frequency steps and is shown in Fig. 18. The SAC as computed through the semi-analytic Transfer Matrix Method (TMM) is used as a reference. It is clear that all three methods offer coinciding absorption curve results.

The relative differences in the displacement (Eq. (124)) and pressure (Eq. (125)) values at the interfaces, as obtained by the VEM using the stabilization parameter choices  $\beta_K^G$  and  $\beta_K^N$  are displayed across the frequency spectrum in Figs. 19a and Fig. 19b, respectively. It can be seen from these figures that the differences have small upper bounds of  $1.6 \times 10^{-3}$  and  $1.5 \times 10^{-4}$ . These are generally prevalent at high frequencies. While they do not affect the quality of the computed SAC in this example, it is still possible that appreciable deviations may be observed in cases where mesh distortion is more severe. Hence, when encountering meshes with potentially non-standard aspect ratios,  $\beta_K^N$  is recommended over  $\beta_K^G$ .

ID	Name	$\sigma$	$\phi$	$\alpha_\infty$	$\Lambda$	$\Lambda'$	$E$	$\nu$	$\eta_s$	$\rho$
I	Melamine foam	$N \cdot s \cdot m^{-4}$ $10^4$	0.99	1.01	$9.8 \times 10^{-5}$	$1.96 \times 10^{-4}$	$1.6 \times 10^5$	0.44	0.1	8
II	Plaster-board	-	-	-	-	-	$3 \times 10^9$	0.3	0.08	700
III	Air	-	-	-	-	-	-	-	-	1.197

**Table 7** Macroscopic material parameters corresponding to the relevant material ID**Fig. 16**  $u_x$  (in [m]) contours at low and high frequencies, respectively. High frequency FEM contours are also provided for comparison.**Fig. 17**  $p$  (in [Pa]) contours at low and high frequencies, respectively. High frequency FEM contours are also provided for comparison.**Fig. 18** SAC computed by VEM, FEM and TMM for the multilayer absorption problem.

### 6.2.2 Diffuse field transmission loss

A sound transmission problem is studied here for the same multilayer configuration. The right face has an

anechoic termination, i.e., a Robin type impedance boundary condition. This corresponds to the term  $b^{0\Gamma}(p_h, \delta p_h)$  defined in Eq. (23e) and Table 2. A diffuse field acoustic excitation is incident on the left face of the domain. The excitation consists of several oblique incidence plane waves with angles of incidence  $\theta \in [0, 75^\circ]$ . A total of  $N = 20$  samples were computationally determined to be sufficiently representative of the entire diffuse field. The response of the system to an excitation frequency spectra of  $f = [100, 4000]$  Hz is evaluated. The associated  $u_x$ ,  $u_y$  and  $p$  VEM contours for  $\theta = 0^\circ$  and  $\theta = 75^\circ$  are shown in Figs. 20, 21 and 22 for 100 Hz and 4000 Hz respectively.

The elastic wave contours  $u_x$  and  $u_y$  are only computed over the melamine foam and plasterboard domains. Similarly, the acoustic wave contours are eval-

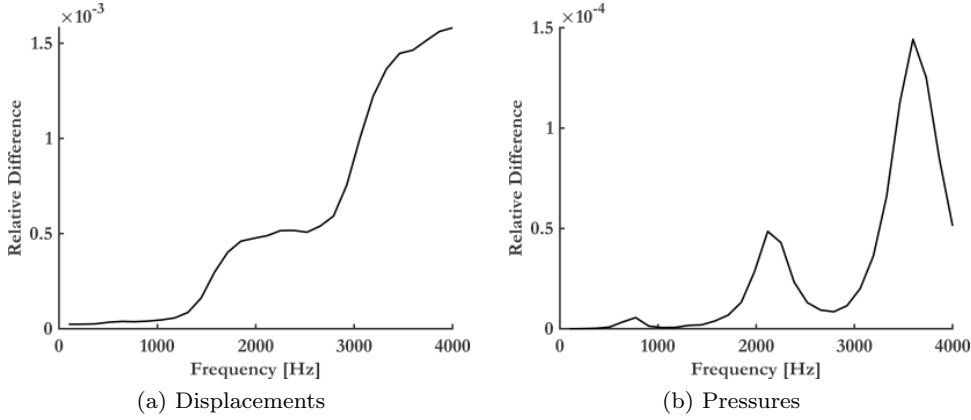


**Fig. 19** Relative differences in spectral solutions generated by the VEM at the interfaces using stabilization parameter choices Eqs. (117) and (118)

ated only over the melamine foam and terminating air layers.

There is a good correspondence between the 4000 Hz  $u_x$ ,  $u_y$  and  $p$  contours as computed by the FEM and VEM for both the cases of normal and oblique incidence. A fully horizontal contour is observed for the elastic wave in x-direction in Figs. 20a, 20b, 20c. Oblique contours are retrieved in Figs. 20c, 20d and 20e. Contrary to the normal incidence case, waves are propagating along the y direction in the 75° case and are shown in Fig. 21a, 21b and 21c. The high frequency excitations have been almost entirely dissipated by the time they enter the plasterboard layer.

The pressures from the acoustic wave are nearly uniformly distributed over each of the two layers at normal incidence, as seen in Figs. 22a, 22b and 22c. Excepting minor oscillations, the high frequency acoustic wave at oblique incidence has almost died down by the time it has reached the rear air layer in Figs. 22e and 22f. The oblique excitation contours encountered in Figs. 20e, 20f, 21b, 21c, 22e and 22f are reminiscent of evanescent waves rather than propagating waves.

The sound transmission loss factor (STL) is computed for the diffuse field excitation according to Eq. (127)

$$\mathcal{T}_{\text{df}}(\omega) = -10 \log_{10} \left( \frac{\int_{0^\circ}^{75^\circ} \mathcal{T}(\omega, \theta) \sin(\theta) \cos(\theta) d\theta}{\int_{0^\circ}^{75^\circ} \sin(\theta) \cos(\theta) d\theta} \right), \quad (127)$$

where  $\mathcal{T}(\omega, \theta)$  denotes the STL computed for a single plane wave at incidence  $\theta$  (see Appendix D). The STL evaluated by the FEM, the VEM, and the TMM is shown in Fig. 23c. The associated STL curves at normal

incidence and oblique incidence  $\theta = 75^\circ$  are provided for clarity in Figs. 23a and 23b, respectively.

The STL curve at normal incidence (Fig. 23a) shows good correlations between all methods. Both the FEM and VEM correctly estimate the coincidence frequency at 75° oblique incidence correctly in Fig. 23b. Similarly, both methods accurately predict the critical frequency for the diffuse field excitation as well in Fig. 23c. However, slight deviations at the peaks of both curves are observed. This is attributed to the following reasoning: the TMM assumes an infinite lateral dimension and as a result does not account for reflections occurring off of the lateral boundaries. This effect is captured by the FEM and VEM and is especially prevalent at large angles of oblique incidence.

### 6.3 Porous composite with tortuous inclusion

This example is adapted from [8] to demonstrate the ability of the VEM to accurately model the acoustic behaviour of a rigid porous composite material. This medium has a tortuous mesoscale inclusion (material II) embedded within the host material (material I). The client material is more permeable than the host. The macroscopic parameters are summarized in Table 8. The configuration is provided with a fully clamped backing (often called rigid backing in acoustical literature) and is subjected to a normal incidence plane wave excitation as shown in Fig. 24.

Contrary to the previous examples, here the preceding air column contained in the impedance tube also needs to be modeled to account for reflection, scattering, dispersion and edge effects introduced by the heterogeneous interface. The relevant inlet and incident quantities are accordingly computed at the extreme left end. Consequently, along with the 45 mm air column,

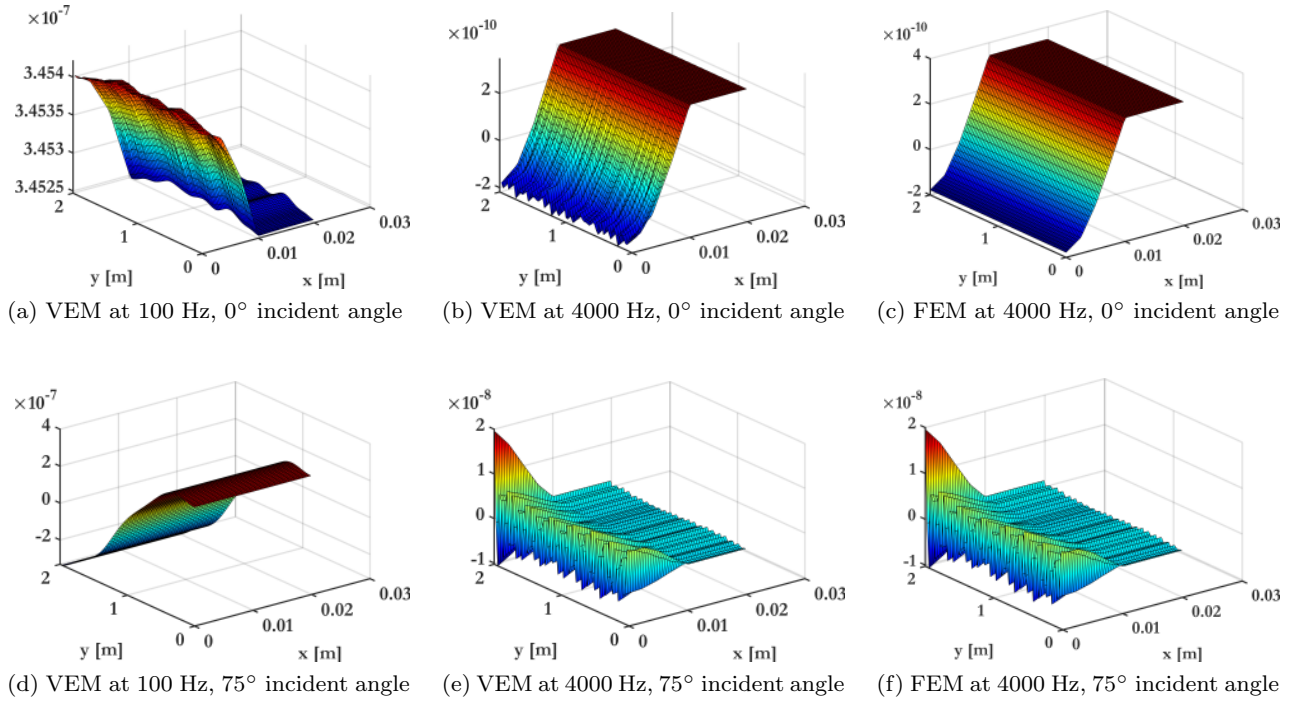


**Fig. 20**  $u_x$  (in [m]) contours at low and high frequencies and angles of incidence, respectively. High frequency FEM contours are also provided for comparison.

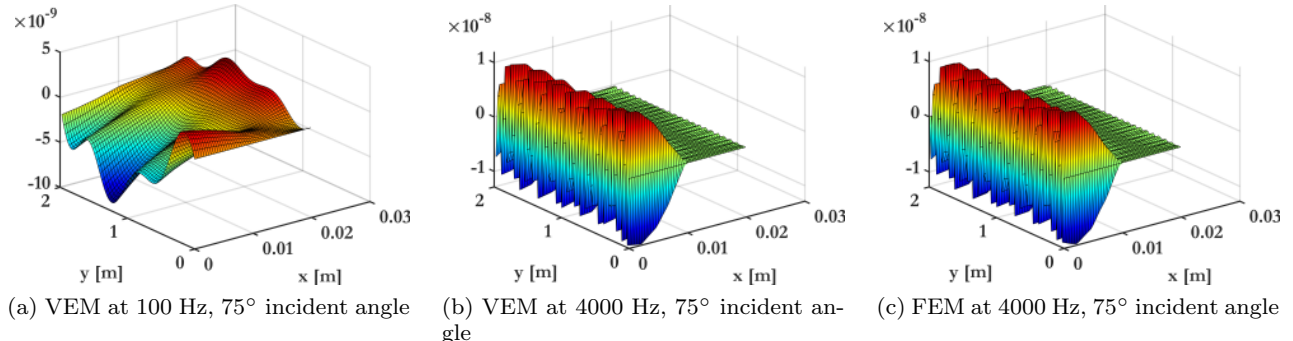


**Fig. 21**  $u_y$  (in [m]) contours at low and high frequencies and high angle of incidence, respectively. High frequency FEM contours are also provided for comparison.

Name	$\sigma$	$\phi$	$\alpha_\infty$	$\Lambda$	$\Lambda'$
I (Host)	$N \cdot s \cdot m^{-4}$ $10^6$	-	-	m $12 \times 10^{-6}$	m $12 \times 10^{-6}$
II (Client)	$1.15 \times 10^4$	1.00 0.96	1 1.01	$108 \times 10^{-6}$	$138 \times 10^{-6}$

**Table 8** Macroscopic material parameters corresponding to the relevant material ID

the entire domain is discretized with 2592 CVT elements - following the 20 elements per minimum wavelength rule. This discretization is illustrated in Fig. 25.

**Remark 11** This is an axi-symmetric domain and hence the plane-strain assumption is not expected to hold, es-

specially in high-frequencies. However, we opted for this test case as it provides insight on the capability of the VEM in efficiently treating tortuous geometries. For this purpose, the accuracy of the method is compared against the TMM and also an axi-symmetric FEM.

It is evident from Fig. 25 that the interfaces between (a) air and the sample, (b) host and client material are not perfectly enforced. This is deliberately done to investigate the influence of imperfect interfaces on the final result. The problem is solved over equally distributed frequency steps ranging from 20 Hz to 5000 Hz. The pressure contours at low (100 Hz) and high

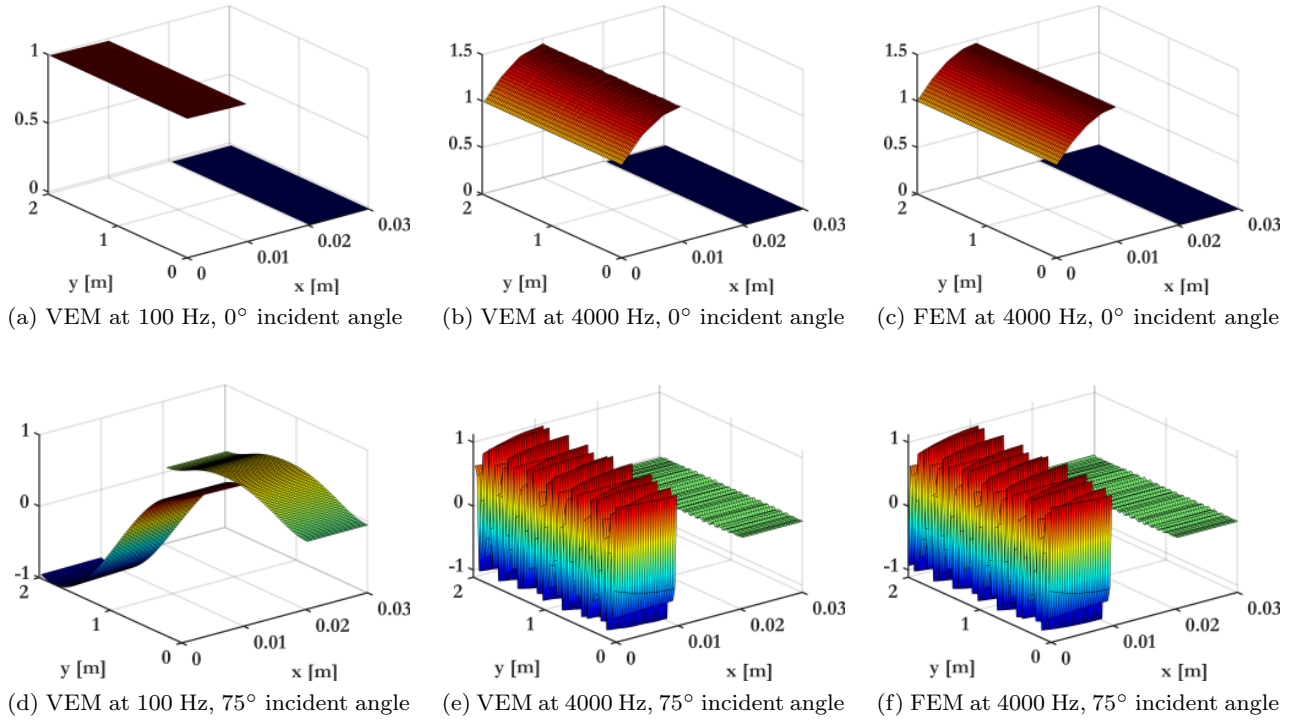


**Fig. 22**  $p$  (in [Pa]) contours at low and high frequencies and angles of incidence, respectively. High frequency FEM contours are also provided for comparison.

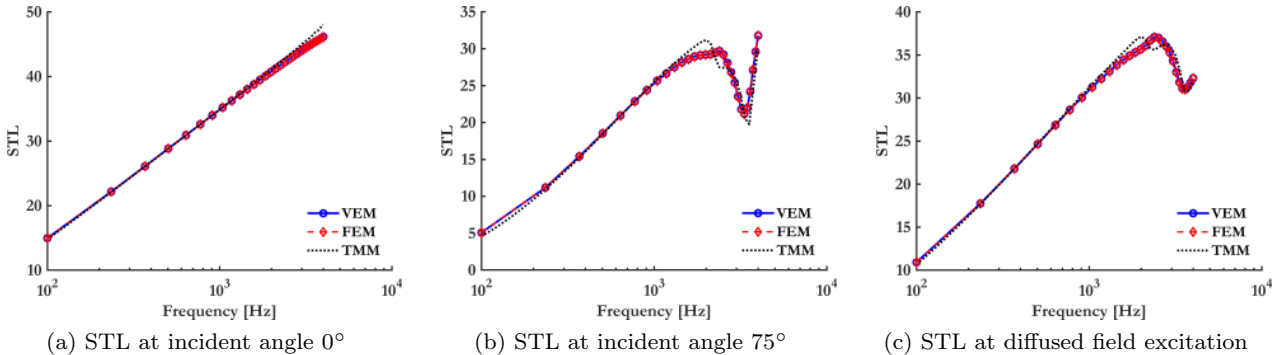


**Fig. 23** Sound Transmission Loss curves computed for the multilayer diffuse field transmission loss problem through the VEM, FEM and TMM

(5000 Hz) as computed by the VEM are displayed in Figs. 26a and 26c, respectively.

The corresponding contours as evaluated by the FEM are shown in Figs. 26b and 26d, respectively. The results are practically identical. The imperfect interfaces does not affect the solutions significantly.

The SACs as computed by the VEM and the axisymmetric FEM are compared with the TMM porous composite model with pressure diffusion effect [8] in Fig. 27. Good agreement between the three methods is observed until  $\approx 3000$  Hz. Beyond this limit, a slight deviation is noticed. This is attributed to two reasons.

First, due to the plane strain assumption that cannot account for the domain axisymmetry. Second, the equivalent model theory [8], on which the porous composite model is based, is no longer perfectly valid as scale separation breaks down here. The acoustic wavelength is now smaller than the characteristic mesoscopic size of the inclusion.

#### 6.4 Mesoscale inclusions

It has already been mentioned in Section 6.2 that porous materials do not offer desirable absorption properties

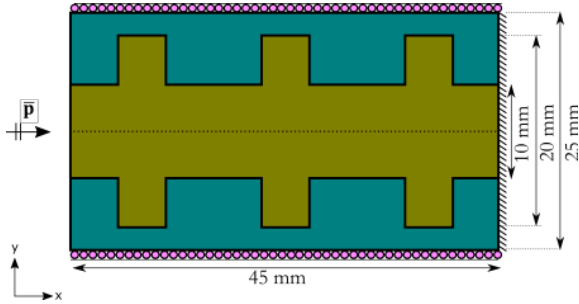


**Fig. 24** Schematic diagram of a 45 mm thick rigid skeleton porous material with a second rigid porous material as a tortuous inclusion. Roller and clamped supports are provided at lateral boundaries and the rear, respectively. The macroscopic parameters of the matrix and inclusion are provided in Table 8.

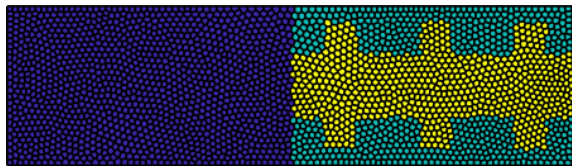


**Fig. 25** The domain along with an equally thick air layer is discretized using 2592 CVT elements, following the 20 elements per minimum wavelength discretization schema.

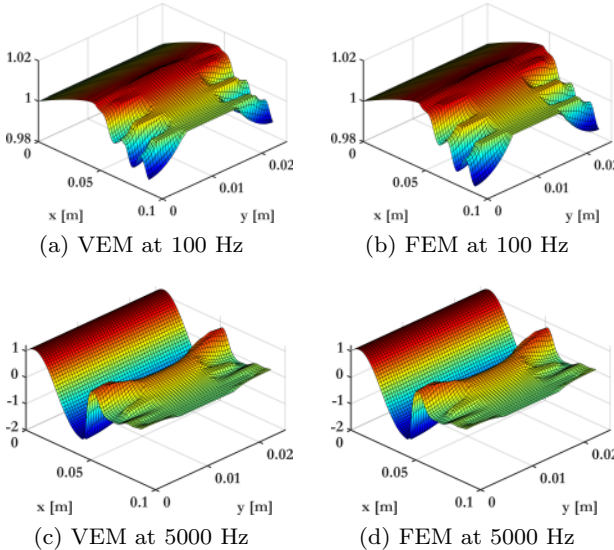


**Fig. 26**  $p$  (in [Pa]) FEM and VEM contours at low and high frequencies at normal incidence plane wave excitation.

at low frequencies. This is traditionally remedied by deploying multilayered systems, as shown in Section 6.4. Alternative solutions are explored in the form of double porosity materials [100], porous composites [8] and embedded inclusions [101]. An example of a tortuous porous composite is provided in Section 6.3. In this example, the ability of embedded rigid inclusions to improve absorption at lower frequencies is shown. The cases provided in Examples 6.4.1 and 6.4.2 are directly

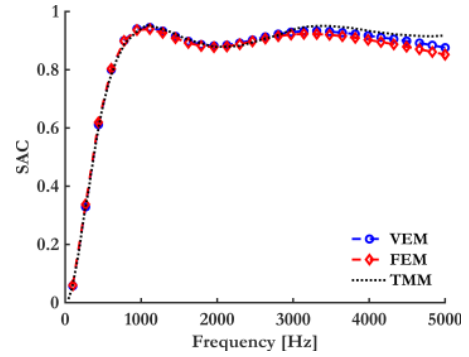


**Fig. 27** SAC computed by the VEM, axi-symmetric FEM and TMM for the rigid porous composite material.

adapted from [101]. All cases are subjected to plane wave normal incidence excitation and a rigid backing. The porous material involved is a foam with rigid motionless skeleton modelled as an equivalent fluid. The exact material parameters are provided in Table 9.

$\sigma$	$\phi$	$\alpha_\infty$	$\Lambda$	$\Lambda'$
$N \cdot s \cdot m^{-4}$	-	-	m	m
8900	0.95	1.42	$180 \times 10^{-6}$	$360 \times 10^{-6}$

**Table 9** Macroscopic material parameters corresponding to the relevant material ID

The inclusions are treated as infinitely rigid cylindrical tubes. This means that the inclusion domain interiors need not be meshed. Additionally, the Neumann boundaries at the inclusion interfaces are zero (zero normal-velocity).

#### 6.4.1 One Inclusion in periodic unit cell

A periodically repeating square unit cell of size 2 cm is taken up. A single cylindrical inclusion centered at (1 cm, 1 cm) of radius 0.75 cm is embedded. The unit cell is repeated ten times in the vertical direction to simulate an infinite lateral dimension. The total vertical dimension is 20 cm. This configuration is illustrated in Fig. 28. The domain has been discretized with uniform CVT elements resulting in a polygonal mesh with 7000 elements and 13,961 nodes. The SAC computed over the frequency range 100 Hz-10kHz with the VEM for this configuration is shown in Fig. 29. The curve is validated against the analytic mode-matching technique developed in [101]. Additionally, the SAC for the same porous domain without the inclusions is also provided for comparison. It is evident that the configuration with inclusions exhibits an improved absorption behaviour in the 1800 Hz - 3800 Hz frequency range. A near-unity peak is observed at  $\approx 3000$  Hz. The pressure contours

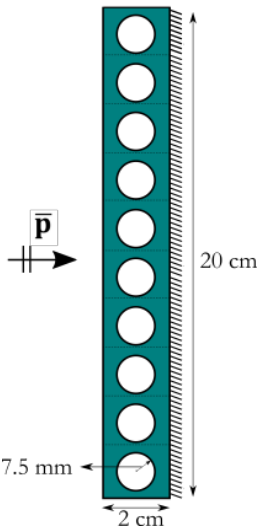


**Fig. 28** A 2 cm thick domain with a single infinitely rigid circular inclusion of radius 7.5 mm, per unit cell. Unit cell repeats periodically in the vertical direction with period 2 cm.

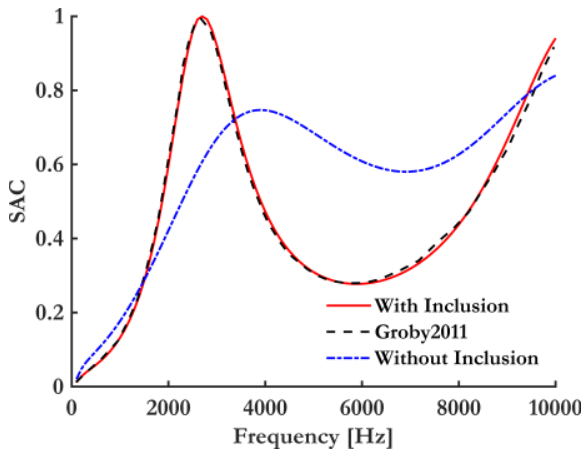


**Fig. 29** SAC computed by the VEM for the domain with and without inclusion. A reference curve using the analytic mode-matching technique from [101] is provided for comparison.

computed by the method at 100 Hz and 10 kHz are shown in Fig. 30.

#### 6.4.2 Two Inclusions in periodic unit cell

A second configuration, comprising two cylindrical inclusions of different sizes within the unit cell is shown in Fig. 31. The unit cell is rectangular ( $3.5\text{cm} \times 2\text{cm}$ ) with a period of 2 cm. The first inclusion is centered at (2.5 cm, 1cm) with radius 0.75 cm. The second inclusion is of radius 0.5 cm and is centered at (1.5 cm,  $2.5 - \sqrt{3}$ ). The domain is discretized with 7000 uniform CVT elements resulting in 13,990 nodes. The SAC computed over the frequency range 100 Hz-10kHz by

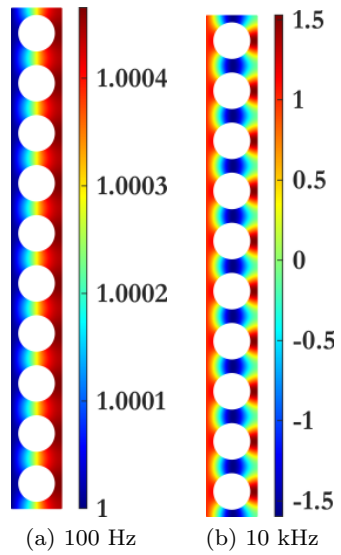


**Fig. 30**  $p$  (in [Pa]) contours computed by VEM at low and high frequencies at normal incidence plane wave excitation.

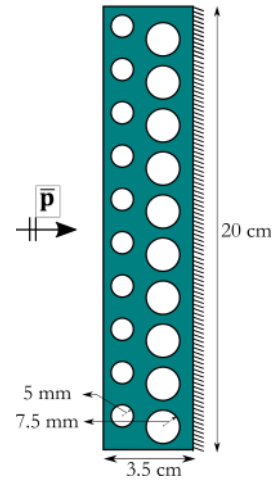


**Fig. 31** A 3.5 cm thick domain with two infinitely rigid circular inclusions of radius 7.5 mm and 5 mm respectively, per unit cell. Unit cell repeats periodically in the vertical direction with period 2 cm.

the VEM for the configurations with and without inclusions are shown in Fig. 32. Improvements in absorption behaviour are exhibited by the configuration with inclusions across two frequency bands: 1600 Hz - 2200 Hz, 3700 Hz - 5000 Hz. These low frequency absorption peaks in both cases are primarily due to the tortuosity added by the solid inclusions.

#### 6.4.3 Complex inclusion geometries

The ability of the VEM to easily model more complex non-periodic inclusions is demonstrated here. The

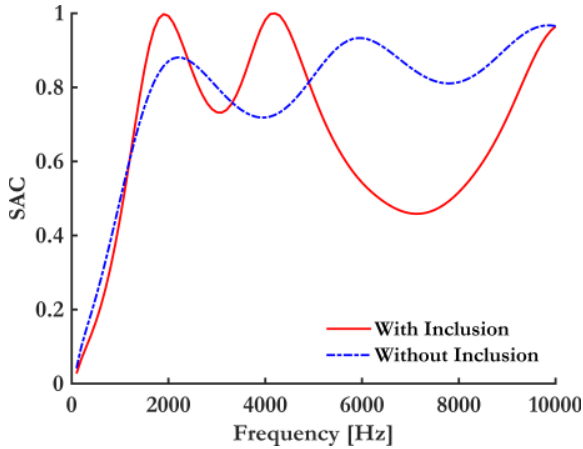


**Fig. 32** SAC computed by the VEM for the domain with and without inclusions.

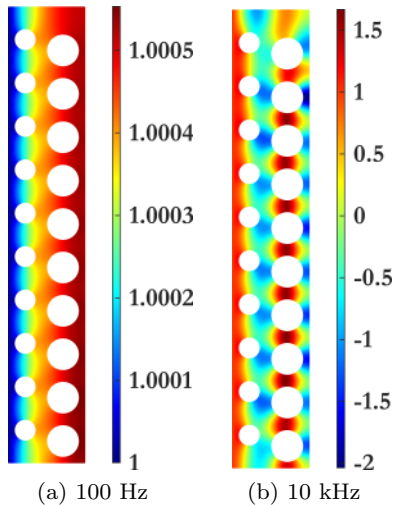


**Fig. 33**  $p$  (in [Pa]) contours computed by VEM at low and high frequencies at normal incidence plane wave excitation.

first example is a  $5\text{ cm} \times 15\text{ cm}$  rectangular domain with irregular infinitely rigid inclusions in the shape of alphabets V-E-M. This domain is discretized with a CVT mesh containing 2500 elements and 5030 nodes. The pressure contours at 100 Hz and 10 kHz are shown in Fig. 34. The second example increases the inclusion complexity even further by embedding inclusions in the shape of a bat, spider and pacman in a  $6\text{ cm} \times 18\text{ cm}$  rectangular domain. The discretization involved contains 5000 CVT elements with 10,054 nodes. The low and high frequency pressure contours are provided in Fig. 35. Both examples use the same equivalent fluid porous foam described in Sections 6.4.1 and 6.4.2 and employ the same boundary conditions.

The discretizations used for these different inclusion-types are summarized in Table 10.

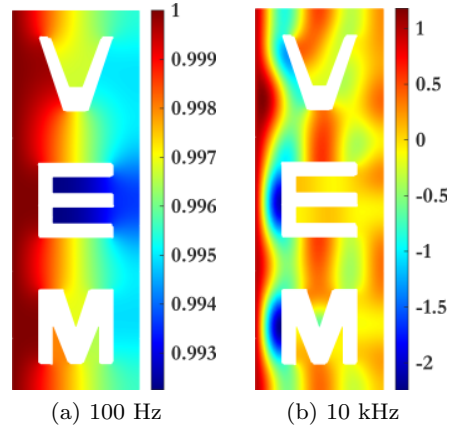


**Fig. 34**  $p$  contours computed by the VEM at low and high frequencies at normal incidence plane wave excitation.

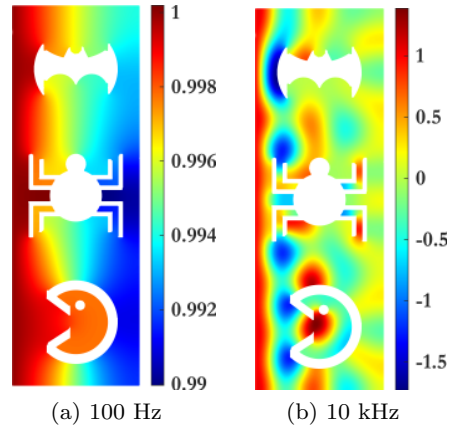


**Fig. 35**  $p$  contours computed by the VEM at low and high frequencies at normal incidence plane wave excitation.

Mesh	Nodes	Elements
One inclusion	13,961	7000
Two inclusions	13,990	7000
V-E-M	5030	2500
Superhero	10,054	5000

**Table 10** Discretizations for the four inclusion-types used in Section 6.4

## 7 Concluding Remarks

A novel VEM discretization has been proposed for studying the vibro-acoustic behaviour of fluid, elastic and poroelastic materials in the frequency domain. The novelty of the method lies in employing the flexible meshing capabilities of the VEM to reduce computational cost and accurately capture complex interfaces. Implicitly defined basis functions are used to evaluate elementary state matrices through employing appropriately defined

operator-specific projectors. The final matrix form of equations are non-linear in  $\omega$ , and are repeatedly solved over the desired frequency spectrum. The solution is post-processed to obtain acoustic indicators like SAC and STL.

The method was shown to exhibit near-optimal convergence rates for different element types in Example 6.1. This illustrates that the VEM can accurately handle versatile mesh configurations at different frequencies. Furthermore, the computational gains achieved are discussed and evidenced by comparisons with the FEM. The ability of the method to handle different types of materials (fluid, elastic, poroelastic) and the resulting interface coupling conditions are provided in Example 6.2. This section also shows that the VEM can be used to easily resolve non-conforming interfaces using appropriate node-insertion algorithms. In this context, the accuracy of two different stabilization parameter choices was explored; although the differences were negligible, the non-isotropic stabilisation procedure seems to provide more well-behaved solutions at the higher frequency spectrum. Different excitations (plane waves at normal and oblique incidence, diffuse-fields) and constraints (rigid backing, anechoic termination) were considered and the accuracy of the method was verified in each case against the TMM.

Example 6.3 concerns tortuous rigid porous composites and shows that the VEM can be used to study the influence of imperfectly defined interfaces. Example 6.4 illustrates the power of the VEM in handling complex periodic and non-periodic mesoscale inclusions across a reasonably large frequency bandwidth. Examples 6.3 and 6.4 show the potential of using the VEM as a simulation tool in investigating the absorption behaviour of porous composites, in contrast to more classical multi-layer systems, as shown in Example 6.2.

The method is currently limited by its confinement to exclusively 2-D domains. Extending the method to 3-D polyhedral or 2-D axi-symmetric discretizations is currently a work in progress.

**Acknowledgements** This work has been carried out under the auspices of the grant: "European industrial doctorate for advanced, lightweight and silent, multifunctional composite structures — N2N". The N2N project is funded under the European Union's Horizon 2020 research and innovation programme under the Marie Skłodowska-Curie Actions Grant: 765472.

## Conflict of interest

The authors declare that they have no conflict of interest.

## References

- J. Tychsen, J. Rösler, Production and characterization of porous materials with customized acoustic and mechanical properties, in: Fundamentals of High Lift for Future Civil Aircraft, Springer, 2020, pp. 497–512.
- K. Hirosawa, Numerical study on the influence of fiber cross-sectional shapes on the sound absorption efficiency of fibrous porous materials, *Applied Acoustics* 164 (2020) 107222.
- Z. Liu, M. Fard, J. L. Davy, Prediction of the acoustic effect of an interior trim porous material inside a rigid-walled car air cavity model, *Applied Acoustics* 165 (2020) 107325.
- S. A. Cummer, J. Christensen, A. Alù, Controlling sound with acoustic metamaterials, *Nature Reviews Materials* 1 (3) (2016) 1–13.
- G. Ma, P. Sheng, Acoustic metamaterials: From local resonances to broad horizons, *Science advances* 2 (2) (2016) e1501595.
- R. Fitzgerald, Helmholtz equation as an initial value problem with application to acoustic propagation, *The Journal of the Acoustical Society of America* 57 (4) (1975) 839–842.
- C. Zwicker, C. W. Kosten, Sound absorbing materials, Elsevier publishing company, 1949.
- F. Chevillotte, L. Jaouen, F.-X. Bécot, On the modeling of visco-thermal dissipations in heterogeneous porous media, *The Journal of the Acoustical Society of America* 138 (6) (2015) 3922–3929.
- M. A. Biot, Theory of propagation of elastic waves in a fluid-saturated porous solid. i. low-frequency range, *J. Acoust. Soc. Am.* 28 (2) (1956) 168–178.
- M. A. Biot, Theory of propagation of elastic waves in a fluid-saturated porous solid. ii. higher frequency range, *J. Acoust. Soc. Am.* 28 (2) (1956) 179–191.
- N. Atalla, R. Panneton, P. Debergue, A mixed displacement-pressure formulation for poroelastic materials, *The Journal of the Acoustical Society of America* 104 (3) (1998) 1444–1452.
- F.-X. Bécot, L. Jaouen, An alternative Biot's formulation for dissipative porous media with skeleton deformation, *The Journal of the Acoustical Society of America* 134 (6) (2013) 4801–4807.
- L. Jaouen, Acoustical porous material recipes, Website. URL: <http://apmr.matelys.com>.
- F. Chevillotte, C. Perrot, E. Guillon, A direct link between microstructure and acoustical macro-behavior of real double porosity foams, *The Journal of the Acoustical Society of America* 134 (6) (2013) 4681–4690.
- C. Perrot, F. Chevillotte, R. Panneton, Micro-/macro relations linking local geometry parameters to sound absorption of porous media.
- D. L. Johnson, J. Koplik, R. Dashen, Theory of dynamic permeability and tortuosity in fluid-saturated porous media, *J. Fluid Mech.* 176 (1987) 379–402.
- Y. Champoux, J.-F. Allard, Dynamic tortuosity and bulk modulus in air-saturated porous media, *J. Appl. Phys.* 70 (1991) 1975–1979.
- D. Lafarge, P. Lemarinier, J.-F. Allard, V. Tarnow, Dynamic compressibility of air in porous structures at audible frequencies, *J. Acoust. Soc. Am.* 102 (4) (1997) 1995–2006.
- Y. Miki, Acoustical properties of porous materials—modifications of Delany-Bazley models, *Journal of the Acoustical Society of Japan (E)* 11 (1) (1990) 19–24.

20. S. Mousavi, N. Sukumar, Numerical integration of polynomials and discontinuous functions on irregular convex polygons and polyhedrons, *Computational Mechanics* 47 (5) (2011) 535–554.
21. J. E. Bishop, A displacement-based finite element formulation for general polyhedra using harmonic shape functions, *International Journal for Numerical Methods in Engineering* 97 (1) (2014) 1–31.
22. G. Manzini, A. Russo, N. Sukumar, New perspectives on polygonal and polyhedral finite element methods, *Mathematical Models and Methods in Applied Sciences* 24 (08) (2014) 1665–1699.
23. C. Talischi, G. H. Paulino, A. Pereira, I. F. Menezes, Polytop: a matlab implementation of a general topology optimization framework using unstructured polygonal finite element meshes, *Structural and Multidisciplinary Optimization* 45 (3) (2012) 329–357.
24. G. H. Paulino, A. L. Gain, Bridging art and engineering using escher-based virtual elements, *Structural and Multidisciplinary Optimization* 51 (4) (2015) 867–883.
25. D. W. Spring, S. E. Leon, G. H. Paulino, Unstructured polygonal meshes with adaptive refinement for the numerical simulation of dynamic cohesive fracture, *International Journal of Fracture* 189 (1) (2014) 33–57.
26. N. Sukumar, J. Bolander, Voronoi-based interpolants for fracture modelling, *Tessellations in the Sciences*.
27. S. Leon, D. Spring, G. Paulino, Reduction in mesh bias for dynamic fracture using adaptive splitting of polygonal finite elements, *International Journal for Numerical Methods in Engineering* 100 (8) (2014) 555–576.
28. S. Biabanaki, A. Khoei, P. Wriggers, Polygonal finite element methods for contact-impact problems on non-conformal meshes, *Computer Methods in Applied Mechanics and Engineering* 269 (2014) 198–221.
29. C. Talischi, A. Pereira, G. H. Paulino, I. F. Menezes, M. S. Carvalho, Polygonal finite elements for incompressible fluid flow, *International Journal for Numerical Methods in Fluids* 74 (2) (2014) 134–151.
30. E. L. Wachspress, W. EL, A rational finite element basis.
31. J. Warren, Barycentric coordinates for convex polytopes, *Advances in Computational Mathematics* 6 (1) (1996) 97–108.
32. R. Sibson, A vector identity for the dirichlet tessellation, in: *Mathematical Proceedings of the Cambridge Philosophical Society*, Vol. 87, Cambridge University Press, 1980, pp. 151–155.
33. V. Belikov, V. Ivanov, V. Kontorovich, S. Korytnik, A. Y. Semenov, The non-sibsonian interpolation: a new method of interpolation of the values of a function on an arbitrary set of points, *Computational mathematics and mathematical physics* 37 (1) (1997) 9–15.
34. M. S. Floater, Mean value coordinates, *Computer aided geometric design* 20 (1) (2003) 19–27.
35. M. S. Floater, G. Kós, M. Reimers, Mean value coordinates in 3d, *Computer Aided Geometric Design* 22 (7) (2005) 623–631.
36. N. Sukumar, Construction of polygonal interpolants: a maximum entropy approach, *International journal for numerical methods in engineering* 61 (12) (2004) 2159–2181.
37. M. Arroyo, M. Ortiz, Local maximum-entropy approximation schemes: a seamless bridge between finite elements and meshfree methods, *International journal for numerical methods in engineering* 65 (13) (2006) 2167–2202.
38. N. Sukumar, E. Malsch, Recent advances in the construction of polygonal finite element interpolants, *Archives of Computational Methods in Engineering* 13 (1) (2006) 129.
39. S. Natarajan, S. Bordas, D. Roy Mahapatra, Numerical integration over arbitrary polygonal domains based on Schwarz–Christoffel conformal mapping, *International Journal for Numerical Methods in Engineering* 80 (1) (2009) 103–134.
40. L. Beirão Da Veiga, F. Brezzi, A. Cangiani, G. Manzini, L. Marini, A. Russo, Basic principles of virtual element methods, *Mathematical Models and Methods in Applied Sciences* 23(1) (2013) 199–214.
41. B. Ahmad, A. Alsaedi, F. Brezzi, L. D. Marini, A. Russo, Equivalent projectors for virtual element methods, *Computers & Mathematics with Applications* 66 (3) (2013) 376–391.
42. F. Brezzi, R. S. Falk, L. D. Marini, Basic principles of mixed virtual element methods, *ESAIM: Mathematical Modelling and Numerical Analysis* 48 (4) (2014) 1227–1240.
43. J. Bonelle, A. Ern, Analysis of compatible discrete operator schemes for elliptic problems on polyhedral meshes, *ESAIM: Mathematical Modelling and Numerical Analysis* 48 (2) (2014) 553–581.
44. G. Vacca, L. Beirão da Veiga, Virtual element methods for parabolic problems on polygonal meshes, *Numerical Methods for Partial Differential Equations* 31 (6) (2015) 2110–2134.
45. B. A. de Dios, K. Lipnikov, G. Manzini, The nonconforming virtual element method, *ESAIM: Mathematical Modelling and Numerical Analysis* 50 (3) (2016) 879–904.
46. K. Lipnikov, G. Manzini, M. Shashkov, Mimetic finite difference method, *Journal of Computational Physics* 257 (2014) 1163–1227.
47. L. Beirão Da Veiga, F. Brezzi, L. Marini, A. Russo, The hitchhiker’s guide to the virtual element method, *Mathematical Models and Methods in Applied Sciences* 24(8) (2014) 1541–1573.
48. L. B. Da Veiga, A. Russo, G. Vacca, The virtual element method with curved edges, *ESAIM: Mathematical Modelling and Numerical Analysis* 53 (2) (2019) 375–404.
49. E. Artioli, L. B. da Veiga, M. Verani, An adaptive curved virtual element method for the statistical homogenization of random fibre-reinforced composites, *Finite Elements in Analysis and Design* 177 (2020) 103418.
50. P. Wriggers, B. Hudobivnik, F. Aldakheel, A virtual element formulation for general element shapes, *Computational Mechanics* (2020) 1–15.
51. V. M. Nguyen-Thanh, X. Zhuang, H. Nguyen-Xuan, T. Rabczuk, P. Wriggers, A virtual element method for 2d linear elastic fracture analysis, *Computer Methods in Applied Mechanics and Engineering* 340 (2018) 366–395.
52. F. Aldakheel, B. Hudobivnik, P. Wriggers, Virtual element formulation for phase-field modeling of ductile fracture, *International Journal for Multiscale Computational Engineering* 17 (2).
53. A. Hussein, B. Hudobivnik, P. Wriggers, A combined adaptive phase field and discrete cutting method for the prediction of crack paths.
54. L. Beirão da Veiga, D. Mora, G. Rivera, A virtual element method for Reissner-Mindlin plates, Tech. rep., CI2MA preprint 2016-14, available from <http://www.ci2ma.udc.cl>.

55. C. Chinosi, Vem for the Reissner-Mindlin plate based on the mitc approach: The element of degree 2, in: European Conference on Numerical Mathematics and Advanced Applications, Springer, 2017, pp. 519–527.
56. V. Gyrya, H. M. Mourad, C1-continuous virtual element method for Poisson-Kirchhoff plate problem, Tech. rep., Los Alamos National Lab.(LANL), Los Alamos, NM (United States) (2016).
57. A. Gain, C. Talischi, G. H. Paulino, On the virtual element method for three-dimensional elasticity problems on arbitrary polyhedral meshes, Computer Methods in Applied Mechanics and Engineering 282 (2013) 132–160. doi:10.1016/j.cma.2014.05.005.
58. E. Artioli, S. De Miranda, C. Lovadina, L. Patruno, A stress/displacement virtual element method for plane elasticity problems, Computer Methods in Applied Mechanics and Engineering 325 (2017) 155–174.
59. E. Artioli, L. B. Da Veiga, C. Lovadina, E. Sacco, Arbitrary order 2d virtual elements for polygonal meshes: part i, elastic problem, Computational Mechanics 60 (3) (2017) 355–377.
60. L. Beirão Da Veiga, F. Brezzi, L. D. Marini, Virtual elements for linear elasticity problems, SIAM Journal on Numerical Analysis 51 (2) (2013) 794–812.
61. A. Sreekumar, S. P. Triantafyllou, F.-X. Bécot, F. Chevillotte, A multiscale virtual element method for the analysis of heterogeneous media, International Journal for Numerical Methods in Engineering 121 (8) (2020) 1791–1821.
62. P. Wriggers, W. Rust, B. Reddy, A virtual element method for contact, Computational Mechanics 58 (6) (2016) 1039–1050.
63. E. Artioli, S. Marfia, E. Sacco, High-order virtual element method for the homogenization of long fiber nonlinear composites, Computer Methods in Applied Mechanics and Engineering 341 (2018) 571–585.
64. M. Pingaro, M. L. De Bellis, P. Trovalusci, R. Masiani, Statistical homogenization of polycrystal composite materials with thin interfaces using virtual element method, Composite Structures 264 (2021) 113741.
65. L. B. da Veiga, D. Mora, G. Rivera, R. Rodríguez, A virtual element method for the acoustic vibration problem, Numerische Mathematik 136 (3) (2017) 725–763.
66. I. Perugia, P. Pietra, A. Russo, A plane wave virtual element method for the Helmholtz problem, ESAIM: Mathematical Modelling and Numerical Analysis 50 (3) (2016) 783–808.
67. C. Böhm, B. Hudobivnik, M. Marino, P. Wriggers, Electro-magneto-mechanical response of polycrystalline materials: Computational homogenization via the virtual element method, Computer Methods in Applied Mechanics and Engineering 380 (2021) 113775.
68. O. Andersen, H. M. Nilsen, X. Raynaud, Virtual element method for geomechanical simulations of reservoir models, Computational Geosciences 21 (5-6) (2017) 877–893.
69. H. M. Nilsen, I. Larsen, X. Raynaud, Combining the modified discrete element method with the virtual element method for fracturing of porous media, Computational Geosciences 21 (5) (2017) 1059–1073.
70. G. Vacca, An H1-conforming virtual element for Darcy and Brinkman equations, Mathematical Models and Methods in Applied Sciences 28 (01) (2018) 159–194.
71. E. Cáceres, G. N. Gatica, F. A. Sequeira, A mixed virtual element method for the brinkman problem, Mathematical Models and Methods in Applied Sciences 27 (04) (2017) 707–743.
72. L. Beirão Da Veiga, F. Brezzi, L. D. Marini, A. Russo, Mixed virtual element methods for general second order elliptic problems on polygonal meshes, ESAIM: Mathematical Modelling and Numerical Analysis 50 (3) (2016) 727–747.
73. F. Dassi, G. Vacca, Bricks for the mixed high-order virtual element method: projectors and differential operators.
74. J. Coulet, I. Faille, V. Girault, N. Guy, F. Nataf, A fully coupled scheme using virtual element method and finite volume for poroelasticity, Computational Geosciences (2019) 1–23.
75. R. Bürger, S. Kumar, D. Mora, R. Ruiz-Baier, N. Verma, Virtual element methods for the three-field formulation of time-dependent linear poroelasticity, arXiv preprint arXiv:1912.06029.
76. A. Sreekumar, S. P. Triantafyllou, F.-X. Bécot, F. Chevillotte, Multiscale vem for the Biot consolidation analysis of complex and highly heterogeneous domains, Computer Methods in Applied Mechanics and Engineering 375 113543.
77. L. B. da Veiga, A. Pichler, G. Vacca, A virtual element method for the miscible displacement of incompressible fluids in porous media, Computer Methods in Applied Mechanics and Engineering 375 (2021) 113649.
78. A. Borio, F. P. Hamon, N. Castelletto, J. A. White, R. R. Settgast, Hybrid mimetic finite-difference and virtual element formulation for coupled poromechanics, Computer Methods in Applied Mechanics and Engineering 383 (2021) 113917.
79. J.-F. Sigmund, Fluid-structure interaction: an introduction to finite element coupling, John Wiley & Sons, 2015.
80. M. A. Biot, Mechanics of deformation and acoustic propagation in porous media, Journal of applied physics 33 (4) (1962) 1482–1498.
81. O. Dazel, B. Brouard, C. Depollier, S. Griffiths, An alternative Biot's displacement formulation for porous materials, The Journal of the Acoustical Society of America 121 (6) (2007) 3509–3516.
82. P. Debergue, R. Panneton, N. Atalla, Boundary conditions for the weak formulation of the mixed (u, p) poroelasticity problem, The Journal of the acoustical Society of America 106 (5) (1999) 2383–2390.
83. M. Mengolini, M. F. Benedetto, A. M. Aragon, An engineering perspective to the virtual element method and its interplay with the standard finite element method, Computer Methods in Applied Mechanics and Engineering, 350 (6) (2019) 995–1023, doi =https://doi.org/10.1016/j.cma.2019.02.043.,
84. L. Beirão Da Veiga, F. Brezzi, L. Marini, A. Russo, Serendipity nodal vem spaces, Computers & Fluids 141 (2016) 2–12.
85. A. Cangiani, G. Manzini, A. Russo, N. Sukumar, Hourglass stabilization and the virtual element method, International Journal for Numerical Methods in Engineering 102 (3-4) (2015) 404–436.
86. L. Beirão da Veiga, C. Lovadina, A. Russo, Stability analysis for the virtual element method, Mathematical Models and Methods in Applied Sciences 27 (13) (2017) 2557–2594.
87. F. Dassi, L. Mascotto, Exploring high-order three dimensional virtual elements: bases and stabilizations, Computers & Mathematics with Applications 75 (9) (2018) 3379–3401.

88. T. Sorgente, S. Biasotti, G. Manzini, M. Spagnuolo, The role of mesh quality and mesh quality indicators in the virtual element method, arXiv preprint arXiv:2102.04138.
89. J. Allard, N. Atalla, Propagation of sound in porous media: modelling sound absorbing materials 2e, John Wiley & Sons, 2009.
90. T. Strouboulis, K. Copps, I. Babuška, The generalized finite element method: an example of its implementation and illustration of its performance, International Journal for Numerical Methods in Engineering 47 (8) (2000) 1401–1417.
91. C. Farhat, I. Harari, L. P. Franca, The discontinuous enrichment method, Computer methods in applied mechanics and engineering 190 (48) (2001) 6455–6479.
92. A. T. Patera, A spectral element method for fluid dynamics: laminar flow in a channel expansion, Journal of computational Physics 54 (3) (1984) 468–488.
93. E. Nobrega, F. Gautier, A. Pelat, J. Dos Santos, Vibration band gaps for elastic metamaterial rods using wave finite element method, Mechanical Systems and Signal Processing 79 (2016) 192–202.
94. O. Zienkiewicz, C. Emson, P. Bettess, A novel boundary infinite element, International Journal for Numerical Methods in Engineering 19 (3) (1983) 393–404.
95. W. C. Chew, Q. Liu, Perfectly matched layers for elastodynamics: a new absorbing boundary condition, Journal of Computational Acoustics 4 (04) (1996) 341–359.
96. M. Soliman, F. L. DiMaggio, Doubly asymptotic approximations as non-reflecting boundaries in fluid-structure interaction problems, Computers & Structures 17 (2) (1983) 193–204.
97. N. Atalla, F. Sgard, Finite element and boundary methods in structural acoustics and vibration, CRC Press, 2015.
98. B. I. Wohlmuth, A mortar finite element method using dual spaces for the Lagrange multiplier, SIAM journal on numerical analysis 38 (3) (2000) 989–1012.
99. E. Wadbro, S. Zahedi, G. Kreiss, M. Berggren, A uniformly well-conditioned, unfitted Nitsche method for interface problems, BIT Numerical Mathematics 53 (3) (2013) 791–820.
100. O. Dazel, F.-X. Bécot, L. Jaouen, Biot effects for sound absorbing double porosity materials, Acta Acustica united with Acustica 98 (4) (2012) 567–576.
101. J.-P. Groby, O. Dazel, A. Duclos, L. Boeckx, L. Kelders, Enhancing the absorption coefficient of a backed rigid frame porous layer by embedding circular periodic inclusions, The Journal of the Acoustical Society of America 130 (6) (2011) 3771–3780.

## Appendix A Monomial spaces

The contents of the monomial spaces  $[\mathbb{M}_k(\mathcal{K})]^2$  and  $[\mathbb{M}_k(\mathcal{K})]$  are iteratively defined in Table 11.

In Table 11,  $\xi = \frac{x-x_{\mathcal{K}}}{h_{\mathcal{K}}}$  and  $\eta = \frac{y-y_{\mathcal{K}}}{h_{\mathcal{K}}}$  denote scaled monomials in each parametric direction. The number of terms in  $[\mathbb{M}_k(\mathcal{K})]^2$  and  $[\mathbb{M}_k(\mathcal{K})]$  are  $n_k^u = (k+1)(k+2)$  and  $n_k^p = \frac{(k+1)(k+2)}{2}$ , respectively. The operator-specific kernels are provided in Table 12. The contents of these kernels can be derived using kinematical decomposition relations mentioned in [73].

The zero-energy modes contained in  $\mathbb{K}^\varepsilon(\mathcal{K})$  can be understood as rigid body motions, i.e., two translations and one rotation in 2-D physical space.

## Appendix B Computing B matrices

Using quadratures, Eq. (66) results in

$$\mathbf{B}_j^{\nabla u} = \mathbf{B}_{bj}^{\nabla u} + \mathbf{B}_{dj}^{\nabla u}, \quad (128)$$

where

$$\mathbf{B}_{bj}^{\nabla u} = \sum_{e \in \partial\mathcal{K}} \int_e \mathbf{u}_h \cdot (\delta^* \nabla \mathbf{m}_{j+2} \mathbf{n}_e^\nabla) \, de, \quad (129)$$

and

$$\mathbf{B}_{dj}^{\nabla u} = - \int_{\mathcal{K} \setminus \partial\mathcal{K}} \mathbf{u}_h \cdot (\delta^* \Delta \mathbf{m}_{j+2}) \, d\mathcal{K} \quad (130)$$

respectively.

Similarly, Eq. (69) becomes

$$\mathbf{B}_j^{\nabla p} = \mathbf{B}_{bj}^{\nabla p} + \mathbf{B}_{dj}^{\nabla p}, \quad (131)$$

where

$$\mathbf{B}_{bj}^{\nabla p} = \sum_{e \in \partial\mathcal{K}} \int_e \mathbf{p}_h \cdot \left( \frac{1}{\tilde{\rho}_{eq}} \nabla \mathbf{m}_{j+1} \cdot \mathbf{n}^\nabla(e) \right) \, de, \quad (132)$$

and

$$\mathbf{B}_{dj}^{\nabla p} = - \int_{\mathcal{K} \setminus \partial\mathcal{K}} \mathbf{p}_h \cdot \left( \frac{1}{\tilde{\rho}_{eq}} \Delta \mathbf{m}_{j+1} \right) \, d\mathcal{K} \quad (133)$$

respectively, where the array  $\mathbf{n}^\nabla(e)$  is defined here as

$$\mathbf{n}^\nabla(e) = [n_x(e) \ n_y(e)]^T. \quad (134)$$

The boundary integrals in Eqs. (128) and (131) are evaluated using Gauss-Lobatto quadratures in a similar manner to Eq. (74).

Polynomial order	$\mathbb{M}_k(\mathcal{K})$	$[\mathbb{M}_k(\mathcal{K})]^2$
$k = 0$	$\mathbb{M}_0(\mathcal{K}) = \{1\}$	$[\mathbb{M}_0(\mathcal{K})]^2 = \left\{ \begin{Bmatrix} 1 \\ 0 \end{Bmatrix}, \begin{Bmatrix} 0 \\ 1 \end{Bmatrix} \right\}$
arbitrary order $k$	$\mathbb{M}_k(\mathcal{K}) = \left\{ \mathbb{M}_{k-1}(\mathcal{K}), \begin{array}{c} \xi^k, \\ \xi^{k-1}\eta, \dots \eta^k \end{array} \right\}$	$[\mathbb{M}_k(\mathcal{K})]^2 = \left\{ \begin{array}{ll} [\mathbb{M}_{k-1}(\mathcal{K})]^2, & \begin{Bmatrix} \xi^k \\ 0 \end{Bmatrix}, \\ \begin{Bmatrix} 0 \\ \xi^k \end{Bmatrix}, & \begin{Bmatrix} \xi^{k-1}\eta \\ 0 \end{Bmatrix}, \begin{Bmatrix} 0 \\ \xi^{k-1}\eta \end{Bmatrix}, \\ \dots & \begin{Bmatrix} \eta^k \\ 0 \end{Bmatrix}, \begin{Bmatrix} 0 \\ \eta^k \end{Bmatrix} \end{array} \right\}$

**Table 11** Generalized scalar and vector valued monomials for  $\mathbb{M}_k(\mathcal{K})$  and  $[\mathbb{M}_k(\mathcal{K})]^2$ , respectively

Operator	Label	Contents	Number of Elements
$a_{\mathcal{K}}^{\varepsilon}(\cdot, \cdot)$	$\mathbb{K}^{\varepsilon}(\mathcal{K})$	$\left\{ \begin{Bmatrix} 1 \\ 0 \end{Bmatrix}, \begin{Bmatrix} 0 \\ 1 \end{Bmatrix}, \begin{Bmatrix} \eta \\ -\xi \end{Bmatrix} \right\}$	3
$a_{\mathcal{K}}^{\nabla}(\cdot, \cdot)$	$\mathbb{K}^{\nabla u}(\mathcal{K})$	$\left\{ \begin{Bmatrix} 1 \\ 0 \end{Bmatrix}, \begin{Bmatrix} 0 \\ 1 \end{Bmatrix} \right\}$	2
$a_{\mathcal{K}}^0(\cdot, \cdot)$	$\mathbb{K}^{0u}(\mathcal{K})$	$\{\emptyset\}$	0
$b_{\mathcal{K}}^0(\cdot, \cdot)$	$\mathbb{K}^{\nabla p}(\mathcal{K})$	$\{1\}$	1
$b_{\mathcal{K}}^0(\cdot, \cdot)$	$\mathbb{K}^{0u}(\mathcal{K})$	$\{\emptyset\}$	0

**Table 12** Definition of operator kernels

To evaluate the corresponding domain integrals, the terms  $\Delta \mathbf{m}_{j+2}$  in Eq. (130) is expanded over the  $[\mathbb{M}_{k-2}(\mathcal{K})]^2$  basis

$$\delta^* \Delta \mathbf{m}_{j+2} = \sum_{\beta=1}^{n_{k-2}^u} d_{j\beta}^{\nabla u} \mathbf{m}_{\beta}, \quad \forall \mathbf{m}_{\beta} \in [\mathbb{M}_{k-2}(\mathcal{K})]^2. \quad (135)$$

Inserting Eq. (135) in Eq. (130) the following expression is derived

$$\mathbf{B}_{dj}^{\nabla u} = -|\mathcal{K}| \sum_{\beta=1}^{n_{k-2}^u} d_{j\beta}^{\nabla u} \text{dof}_{kN_v+\beta}(\mathbf{u}_h) = -|\mathcal{K}| \mathbf{d}^{\nabla u}, \quad (136)$$

where

$$\mathbf{d}^{\nabla u} = \underbrace{\begin{bmatrix} 0 & \cdots & 0 \end{bmatrix}}_{N_B^u} \underbrace{\begin{bmatrix} d_{j1}^{\nabla u} & \cdots & d_{j(n_{k-2}^u)}^{\nabla u} \end{bmatrix}}_{N_A^u}. \quad (137)$$

Similarly, expanding  $\Delta \mathbf{m}_{j+1}$  over the basis  $\mathbb{M}_{k-2}(\mathcal{K})$

$$\frac{1}{\tilde{\rho}_{\text{eq}}} \Delta \mathbf{m}_{j+1} = \sum_{\beta=1}^{n_{k-2}^p} d_{j\beta}^{\nabla p} \mathbf{m}_{\beta}, \quad \forall \mathbf{m}_{\beta} \in \mathbb{M}_{k-2}(\mathcal{K}), \quad (138)$$

where the coefficients  $d_{j\beta}^{\nabla p}$  are also obtained through inspection and substituting in Eq. (133)

$$\mathbf{B}_{dj}^{\nabla p} = -|\mathcal{K}| \sum_{\beta=1}^{n_{k-2}^p} d_{j\beta}^{\nabla p} \text{dof}_{kN_v+\beta}(\mathbf{p}_h) = -|\mathcal{K}| \mathbf{d}^{\nabla p}, \quad (139)$$

where

$$\mathbf{d}^{\nabla p} = \underbrace{\begin{bmatrix} 0 & \cdots & 0 \end{bmatrix}}_{N_B^p} \underbrace{\begin{bmatrix} d_{j1}^{\nabla p} & \cdots & d_{j(n_{k-2}^p)}^{\nabla p} \end{bmatrix}}_{N_A^p}. \quad (140)$$

### Appendix C Computing D matrices

The matrices  $\mathbf{D}^{\varepsilon}$ ,  $\mathbf{D}^{0u}$ ,  $\mathbf{D}^{\nabla p}$ , and  $\mathbf{D}^{0p}$  in Eqs. (105)-(108) assume the following form

$$\mathbf{D}^{\varepsilon} = \begin{bmatrix} \text{dof}_1(\mathbf{m}_1) & \dots & \text{dof}_1(\mathbf{m}_{n_k^u-3}) \\ \vdots & \ddots & \vdots \\ \text{dof}_{n_{\text{dof}}^u}(\mathbf{m}_1) & \dots & \text{dof}_{n_{\text{dof}}^u}(\mathbf{m}_{n_k^u-3}) \end{bmatrix}, \quad (141a)$$

$$\mathbf{D}^{0u} = \begin{bmatrix} \text{dof}_1(\mathbf{m}_1) & \dots & \text{dof}_1(\mathbf{m}_{n_k^u}) \\ \vdots & \ddots & \vdots \\ \text{dof}_{n_{\text{dof}}^u}(\mathbf{m}_1) & \dots & \text{dof}_{n_{\text{dof}}^u}(\mathbf{m}_{n_k^u}) \end{bmatrix}, \quad (141b)$$

$$\mathbf{D}^{\nabla p} = \begin{bmatrix} \text{dof}_1(\mathbf{m}_1) & \dots & \text{dof}_1(\mathbf{m}_{n_k^p-1}) \\ \vdots & \ddots & \vdots \\ \text{dof}_{n_{\text{dof}}^p}(\mathbf{m}_1) & \dots & \text{dof}_{n_{\text{dof}}^p}(\mathbf{m}_{n_k^p-1}) \end{bmatrix}, \quad (141c)$$

$$\mathbf{D}^{0p} = \begin{bmatrix} \text{dof}_1(\mathbf{m}_1) & \dots & \text{dof}_1(\mathbf{m}_{n_k^p}) \\ \vdots & \ddots & \vdots \\ \text{dof}_{n_{\text{dof}}^p}(\mathbf{m}_1) & \dots & \text{dof}_{n_{\text{dof}}^p}(\mathbf{m}_{n_k^p}) \end{bmatrix}, \quad (141d)$$

The quantities  $\text{dof}_i(\mathbf{m}_j)$  and  $\text{dof}_i(\mathbf{m}_j)$  are evaluated according to the following expressions (see Table 4), for the solid

$$\begin{cases} \text{dof}_i(\mathbf{m}_j) = \mathbf{m}_j(\mathbf{x}_i), & \forall i \leq 2kN_v \\ \text{dof}_i(\mathbf{m}_j) = \frac{1}{|\mathcal{K}|} \int_{\mathcal{K}} \mathbf{m}_j \cdot \mathbf{m}_{\beta} d\mathcal{K}, \\ \forall \mathbf{m}_{\beta} \in [\mathbb{M}_{k-2}(\mathcal{K})]^2, & i > 2kN_v, \end{cases} \quad (142)$$

and the fluid phase

$$\begin{cases} \text{dof}_i(\mathbf{m}_j) = \mathbf{m}_j(\mathbf{x}_i), & \forall i \leq kN_v \\ \text{dof}_i(\mathbf{m}_j) = \frac{1}{|\mathcal{K}|} \int_{\mathcal{K}} \mathbf{m}_j \cdot \mathbf{m}_\beta d\mathcal{K}, & \\ \forall \mathbf{m}_\beta \in \mathbb{M}_{k-2}(\mathcal{K}), & i > kN_v \end{cases}, \quad (143)$$

respectively.

## Appendix D Computing Sound Absorption and Transmission Loss coefficients

The complex valued surface impedance at the incident face normalized with respect to the impedance of air  $z(\theta)$  is computed

$$Z_{sn\mathcal{K}}(\omega, \theta) = \left( \frac{p_{\mathcal{K}}^{in}}{v_{n\mathcal{K}}^{in}} \right)_{\Gamma_{hI}^{\mathcal{K}}} / z(\theta) \quad (144)$$

where  $p_{\mathcal{K}}^{in}$  and  $v_{n\mathcal{K}}^{in}$  denote inlet pressures and normal component of fluid velocities over the elementary incident face  $\Gamma_{hI}^{\mathcal{K}}$ . This quantity is now used to obtain the elementary coefficient of reflection:

$$R_{\mathcal{K}}(\omega, \theta) = \frac{Z_{sn\mathcal{K}}(\omega, \theta) - 1}{Z_{sn\mathcal{K}}(\omega, \theta) + 1} \quad (145)$$

As the VEM computes only resultant quantities (the net incident and reflected waves), one requires  $R_{\mathcal{K}}(\omega, \theta)$  to obtain purely incident pressures and normal fluid velocities over  $\Gamma_{hI}^{\mathcal{K}}$ .

$$p_{\mathcal{K}}^{inc} = \left| \frac{p_{\mathcal{K}}^{in}}{1 + R_{\mathcal{K}}(\omega, \theta)} \right|_{\Gamma_{hI}^{\mathcal{K}}}, \quad v_{n\mathcal{K}}^{inc} = \frac{p_{\mathcal{K}}^{inc}}{z(\theta)} \quad (146)$$

The time averaged powers are evaluated according to Eqs. (147) below

$$\begin{aligned} \mathbb{W}^{in}(\omega, \theta) &= \frac{1}{2} \Re \left( \int_{\Gamma_{hI}} p^{in} \cdot v_n^{in*} d\Gamma \right) = \\ &\quad \frac{1}{2} \Re \left( \sum_i \int_{\Gamma_{hI}^{\mathcal{K}(i)}} p_{\mathcal{K}(i)}^{in} \cdot v_{n\mathcal{K}(i)}^{in*} d\Gamma \right), \end{aligned} \quad (147a)$$

$$\begin{aligned} \mathbb{W}^{inc}(\omega, \theta) &= \frac{1}{2} \int_{\Gamma_{hI}} p^{inc} \cdot v_n^{inc} d\Gamma = \\ &\quad \frac{1}{2} \sum_i \int_{\Gamma_{hI}^{\mathcal{K}(i)}} p_{\mathcal{K}(i)}^{inc} \cdot v_{n\mathcal{K}(i)}^{inc} d\Gamma, \end{aligned} \quad (147b)$$

$$\mathbb{W}^{ref}(\omega, \theta) = \mathbb{W}^{inc}(\omega, \theta) - \mathbb{W}^{in}(\omega, \theta), \quad (147c)$$

$$\begin{aligned} \mathbb{W}^{trans}(\omega, \theta) &= \frac{1}{2} \Re \left( \int_{\Gamma_{hO}} p^{out} \cdot v_n^{out*} d\Gamma \right) = \\ &\quad \frac{1}{2} \Re \left( \sum_i \int_{\Gamma_{hO}^{\mathcal{K}(i)}} p_{\mathcal{K}(i)}^{out} \cdot v_{n\mathcal{K}(i)}^{out*} d\Gamma \right), \end{aligned} \quad (147d)$$

where  $\mathbb{W}^{in}$ ,  $\mathbb{W}^{inc}$ ,  $\mathbb{W}^{ref}$  and  $\mathbb{W}^{trans}$  represent inlet, incident, reflected and transmitted powers, respectively. The operator  $\Re(\cdot)$  extracts real valued data, Complex conjugation is denoted by (\*). Outlet fluid pressures and normal components of fluid velocity  $p_{\mathcal{K}(i)}^{out}$  and  $v_{n\mathcal{K}(i)}^{out}$  are evaluated over an elementary outlet face  $\Gamma_{hO}^{\mathcal{K}(i)}$ . The SAC and STL are finally derived for a plane wave incident at an angle  $\theta$  with a driving angular frequency of  $\omega$ :

$$\alpha(\omega, \theta) = 1 - \frac{\mathbb{W}^{ref}(\omega, \theta)}{\mathbb{W}^{inc}(\omega, \theta)}, \quad \mathcal{T}(\omega, \theta) = 10 \log \frac{\mathbb{W}^{inc}(\omega, \theta)}{\mathbb{W}^{trans}(\omega, \theta)}. \quad (148)$$

For a detailed report investigating the post-processing procedures involved in structural and porous vibro-acoustics, see, e.g., [97], [89].